EUSKAL HERRIKO UNIBERTSITATEA - UNIVERSIDAD DEL PAIS VASCO

MATERIALEN FISIKA SAILA - DEPARTAMENTO DE FÍSICA DE MATERIALES

Functionalization of Particles by Atomic Layer Deposition for Energy Storage Applications

Sarai Garcia

PhD Thesis

Thesis supervisors:

Prof. Dr. Mato Knez

Dr. J. Alberto Blázquez

2020

This PhD thesis has been carried out at:

CIC nanoGUNE

Nanomaterials group

Donostia, Spain

CIDETEC

Energy Storage Unit

Donostia, Spain

Resumen

Los materiales en forma de pequeñas partículas son uno de los principales ingredientes en diversos procesos y aplicaciones industriales. Generalmente, estos materiales están clasificados en función de su tamaño y sus funcionalidades: mientras que las partículas en tamaño milimétrico son usadas principalmente en la industria alimentaria, farmacéutica y en sectores de limpieza y construcción, aquellas de tamaño micrométrico y nanométrico son generalmente empleadas en aplicaciones de almacenamiento de energía, catálisis o electrónica.

Las investigaciones pioneras han centrado su atención en partículas de tamaño micrométrico y nanométrico, debido a sus propiedades relevantes con relación a su pequeño tamaño y su gran área superficial. La funcionalización de dichas partículas podría mejorar considerablemente su comportamiento y otorgarles valor añadido. Entre los muchos métodos de funcionalización, cabe destacar la generación de partículas "core-shell", ya sea encapsulando las partículas con un recubrimiento, o bien depositando pequeñas "islas" de un determinado material en su superficie, protegiéndolas, activándolas químicamente, o modificando su comportamiento inicial. En la actualidad, existen diversas técnicas de recubrimiento, las cuales puedes clasificarse principalmente en dos grupos: técnicas de recubrimiento en seco y técnicas de recubrimiento en húmedo. Los métodos de recubrimiento en húmedo se caracterizan principalmente por emplear disolventes durante el proceso de revestimiento. Aunque su aplicación es sencilla, no muchos procesos industriales hacen uso de esta tecnología debido a varios inconvenientes. Entre ellos, destaca el proceso de secado de los disolventes residuales, que requiere largos tiempos de procesado, genera una gran cantidad de residuos y consume mucha energía. Es por ello que en los últimos años, los métodos de recubrimiento

en seco han atraído mucho interés a la hora de depositar películas delgadas. Su ventaja principal reside en el control preciso del espesor del recubrimiento generado, incluso a escala nanométrica. Una de las tecnologías más conocidas en este campo es la deposición química de fase vapor (*Chemical Vapor Deposition*, o CVD), aunque posteriormente se desarrolló una técnica derivada del CVD conocida como deposición de capa atómica (*Atomic Layer Deposition*, o ALD), que permite una mayor precisión en el control del espesor y en la composición de la película depositada.

La aplicación de ALD en diferentes campos, incluyendo microelectrónica, sistemas de almacenamiento de energía y aplicaciones biológicas, ha adaptado esta tecnología a substratos con una gran variedad de formas geométricas; desde substratos planos hasta materiales en forma de partículas. A la hora de recubrir partículas mediante ALD se pueden encontrar dos tipos de reactores en función de cómo se manipulen las partículas: los reactores de partículas estáticas y los reactores de lecho fluidizado. Los reactores de partículas estáticas se utilizan para recubrir pequeñas cantidades. No son adecuados para grandes cantidades, ya que las partículas quedarían menos recubiertas a medida que aumenta la profundidad del lecho. Por otro lado, los reactores de lecho fluidizado mantienen las partículas en constante movimiento durante el proceso de recubrimiento, y por tanto son aptos para procesar mayores cantidades de partículas. En este tipo de reactor se introduce un gas inerte por su parte inferior provocando un movimiento del lecho de partículas similar al de un fluido, manteniéndolas en suspensión y recubriéndolas homogéneamente. Este tipo de reactor permite recubrir grandes cantidades de partículas mediante ALD, y puede ser escalado para su uso en aplicaciones industriales.

La aplicación de la tecnología ALD para la fabricación y/o recubrimiento de componentes de sistemas de almacenamiento de energía se ha investigado intensamente en los últimos años, ofreciendo grandes avances tecnológicos. Las formas más convencionales de producción de energía, principalmente mediante el uso de combustibles fósiles, están siendo sustituidas por tecnologías de producción de energías renovables, que requieren sistemas de almacenamiento de energía eficientes y fiables. Las baterías son uno de los sistemas de almacenamiento de

energía más importantes, gracias a su excelente densidad de energía y tasa de liberación de la misma. Las baterías de iones de litio (*Lithium-Ion Batteries*, LIB) son actualmente el tipo de batería más común en una amplia variedad de aplicaciones. Estas baterías dominan el mercado de la electrónica portátil y la electrificación del transporte, proporcionando una excelente ciclabilidad, una larga vida útil y una alta estabilidad de la densidad de energía, llegando a una densidad de energía de 300 $Wh \cdot kg^{-1}$. Sin embargo, su capacidad específica limitada y los materiales catódicos empleados han llevado a los investigadores a buscar otros tipos de sistemas de baterías alternativas.

Las baterías de litio-azufre (*Lithium-Sulfur*, Li-S) se han convertido en una alternativa prometedora debido al fácil manejo y extraordinarias propiedades del azufre como material catódico activo. Concretamente, las baterías de litio-azufre muestran una densidad de energía teórica de 2600 $Wh \cdot kg^{-1}$ (mucho más alta que la de las baterías de ion litio convencionales). Además, el azufre es ecológico y uno de los elementos más abundantes en el mundo. Sin embargo, las baterías Li-S presentan varios inconvenientes, entre los que destacan la naturaleza aislante del azufre, el efecto de cambio de volumen del cátodo entre la carga y la descarga, el 'shuttle effect' de los polisulfuros y el peligro de seguridad asociado al ánodo de litio. Todos estos inconvenientes han impedido la implantación de esta tecnología, y conducen a los investigadores a encontrar soluciones emergentes para el desarrollo de baterías de Li-S con alta densidad de energía, ciclabilidad y estabilidad a largo plazo. La aplicación de ALD en sistemas de almacenamiento de energía ha demostrado aportar muchas mejoras hasta el momento. De hecho, la deposición de ciertos materiales a escala nanométrica sobre los distintos componentes de una batería se ha erigido como una línea de investigación relevante en la mejora de la densidad de potencia y reversibilidad de las baterías de Li-S.

El objetivo de esta tesis se basa en el estudio y la comprensión de la generación de recubrimientos mediante ALD en materiales en forma de partículas, prestando especial atención a materiales aptos para dispositivos de almacenamiento de energía. Para ello, se han recubierto partículas de tamaño micrométrico y

nanométrico con óxidos metálicos, mostrando resultados prometedores y nuevas funcionalidades que no se habían observado con anterioridad.

En la primera parte de la tesis se realiza un estudio inicial de recubrimiento de partículas mediante ALD en un reactor de partículas estáticas. Para ello se recubren partículas de óxido de hierro (γ-Fe_2O_3) con dióxido de titanio (TiO_2), generando partículas "core-shell" de FeO_x-TiO_2. Este estudio demuestra que mediante la aplicación de ALD no solo se consigue recubrir las partículas, sino que, dependiendo de los reactivos (precursores) utilizados, también se pueden reducir químicamente para formar nanopartículas 'core-shell' de tipo Fe_3O_4-TiO_2. Este estudio demuestra que la elección del ligando apropiado del precursor de metal puede conducir a un enfoque novedoso de recubrimiento y reducción química de las partículas. En este caso, el ligando del precursor organometálico aplicado, $(CH_3)_2N^-$, desencadena la reducción del Fe^{3+} presente en el substrato (γ-Fe_2O_3), mientras se oxida y se recombina formando tetrametilhidrazina como subproducto de la reacción tal y como se muestra en la Figura I. Además, el catión del precursor también desempeña un papel importante, ya que cuanto mayor es su electronegatividad, más energía se requiere para liberar los ligandos, lo cual es condicionante para la recombinación de estos últimos. Por lo tanto, el diseño apropiado de precursores y la selección de substratos adecuados allanarán el camino para la formación de nuevos compuestos, mientras que el proceso ALD empleado permitirá un fácil escalado a nivel industrial de grandes cantidades de partículas, recubiertas y reducidas químicamente al mismo tiempo.

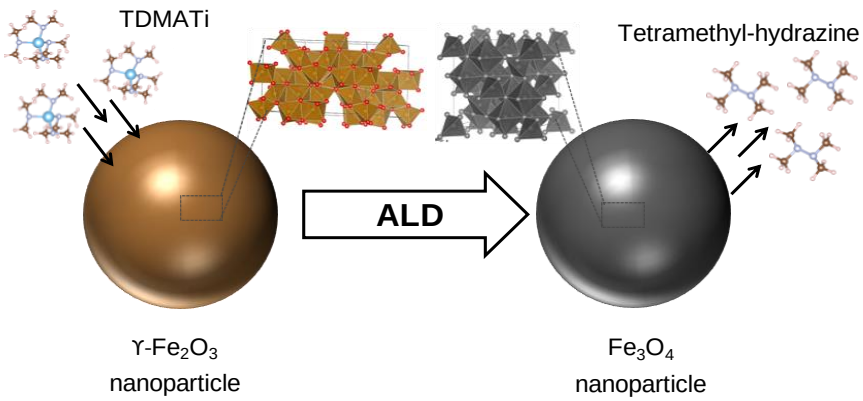

Figura I. Esquema del proceso de ALD desencadenado sobre las partículas de óxido de hierro.

En la segunda parte de la tesis se lleva a cabo el estudio de recubrimientos ALD en dispositivos de almacenamiento de energía, específicamente, en baterías de litio-azufre. Para ello, se realiza la modificación mediante ALD del material catódico de las baterías de Li-S haciendo uso de un reactor de ALD convencional (de partículas estáticas). Como parte del trabajo, se evalúan los parámetros óptimos de aplicación de la película delgada depositada por ALD sobre los electrodos de azufre. Los procesos de ALD se realizan a baja temperatura y se analiza el efecto del material depositado sobre el material catódico tras varios ciclos de deposición. Durante el proceso ALD se deposita óxido de aluminio o alúmina (Al_2O_3) sobre cátodos prefabricados (Figura II), mejorando la capacidad de los sistemas, principalmente a elevadas intensidades de corriente, es decir, a cortos tiempo de carga y descarga. Como resultado, se determina que aplicando únicamente dos ciclos de ALD a 85 ^{o}C, la capacidad de las baterías Li-S aumenta en un 13 % a bajas densidades de corriente (C/5), y en un 50 % a altas densidades de corriente (>1C).

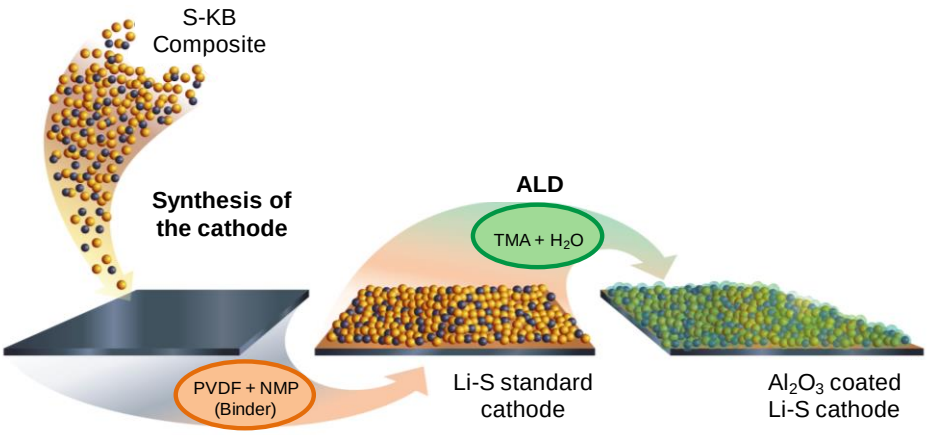

Figura II. Ilustración esquemática de la fabricación del cátodo de azufre y la posterior deposición de alúmina mediante el proceso ALD.

Finalmente, en la última parte de esta tesis, se emplea la técnica ALD como tecnología prometedora para el recubrimiento de composites de azufre-carbono presentes en baterías Li-S, mejorando su rendimiento. En este caso, las partículas compuestas de azufre y carbono son encapsuladas o cubiertas con "islas" de alúmina en su superficie por medio de la técnica ALD en un reactor de lecho fluidizado, que ofrece enormes ventajas para recubrir grandes cantidades de partículas. De esta forma se consiguen unir las partículas antes de la fabricación del cátodo, mejorando su cohesión. Los mejores resultados se obtienen después de aplicar 5 ciclos de ALD, aumentando la capacidad del sistema un 30 % a bajas densidades de corriente, y un 50 % a altas densidades de corriente, con respecto a una batería Li-S estándar. Además, gracias a la mejora morfológica proporcionada por la alúmina depositada (cohesión de partículas) la cantidad de azufre en los cátodos se puede duplicar, fabricando electrodos uniformes y sin grietas con mayor cantidad de azufre, imposibles de fabricar con el composite convencional. Estos nuevos electrodos exceden significativamente el rendimiento de los electrodos estándar, y aumentan la capacidad de las baterías litio-azufre en un 60 %.

Abstract

Powders are essential ingredients for many processes and applications. They are usually classified with relation to their particle sizes and functionalities. While particles in the millimeter size range are intensely used in alimentary, pharmaceutical, cleaning and construction sectors, micrometer and nanometer sized particles are commonly used in energy storage applications, catalysis and electronics.

Recent research has focused its attention on micrometer and nanometer sized particles due to the special properties arising from their high surface area to particle size ratio. Functionalization of those particles can greatly improve their performance. In this way, providing added value, like protecting and activating them, or changing their performance. Among the most promising ways of functionalization is the generation of core-shell particles through coating, or the deposition of islands or clusters on the surface of the particles. Nowadays, a wide variety of coating technologies are applied for this purpose. Among those coating technologies, chemical vapor deposition (CVD) became attractive in the recent years thanks to its great thickness control over the deposited coating. However, more recently, atomic layer deposition (ALD) was developed, allowing for ultimate thickness and compositional control of the deposited film in a large variety of geometries. The application of ALD in different fields, including microelectronics, energy storage systems or bioapplications, pushed the application of this technology to materials with diverse geometries, among those being particles. The need for coating powders resulted in the modification of reactors for carrying out ALD processes on such materials. The various reactors are distinct in the way of handling particles; namely, static particle reactors and fluidized bed

reactors. While static particle reactors are used to coat small amounts of particles, fluidized bed reactors (FBR) can be used to coat large amounts of particles, allowing the scale-up of the technology for its use in industrial applications.

The application of ALD to fabricate or coat materials and components for energy storage systems is intensely investigated and it is beginning to deliver breakthroughs. Batteries belong to the most important energy storage systems thanks to their excellent energy density and energy release rate. Lithium-ion batteries (LIB) are currently the most common battery types for a large variety of applications. In fact, they offer a theoretical energy density of around 300 $Wh \cdot kg^{-1}$. However, their limited specific capacity and the precious cathode materials made researchers looking into other kinds of battery systems as alternatives. Lithium-sulfur (Li-S) batteries became a promising alternative due to their better handling and extraordinary properties of sulfur as cathodic material. Namely, it shows a theoretical energy density of 2600 $Wh \cdot kg^{-1}$, higher than that of Li-ion batteries. Moreover, sulfur is environmentally friendly and one of the most abundant elements in the world. However, Li-S batteries suffer from several drawbacks that affect their application and have driven researchers to develop solutions to enable the practical use of lithium-sulfur batteries and in this was increase the energy density and long-term stability. The application of ALD in energy storage systems has shown many improvements by now. In fact, the deposition of certain materials at the nanometric scale has many unique benefits for improving the behavior of Li-S batteries.

The objective of this thesis is the study and understanding of ALD coatings on powders, paying special attention to materials that can be used for energy storage devices. Micrometer and nanometer sized particles have been coated with metal oxides, which showed promising alterations and functionalities of powders that have not been observed before.

In the first part of the thesis, an initial study of coating particles by ALD is done. For this aim, iron oxide nanoparticles (γ-Fe_2O_3) are coated with titanium dioxide (TiO_2), generating FeO_x-TiO_2 core-shell nanoparticles. This study shows that the

application of ALD not only coats the particles, but also, depending on the reactants (precursors) used, can also reduce them to form core-shell nanoparticles of Fe_3O_4-TiO_2. This study demonstrates that choosing an appropriate ligand of the metal source can unveil a novel approach to concertedly coat and reduce γ-Fe_2O_3 nanoparticles. Moreover, it is found that the more electronegative the cation of the precursor is, the more energy is necessary to release the ligands, which is conditional for their recombination. Thus, the appropriate design of precursors and selection of substrates will pave the way for numerous new compositions with more and improved functionalities.

In the second part of the thesis, the study of ALD on energy storage devices, specifically on lithium-sulfur batteries, is carried out. The modification of the cathode material of lithium-sulfur batteries is done by ALD in a conventional static ALD reactor. The optimal parameters for the ALD application to sulfur-based electrodes are evaluated. Aluminum oxide (Al_2O_3) is deposited on prefabricated cathodes, improving the capacity of the systems. In fact, applying only 2 ALD cycles at 85 °C increases the capacity of a lithium-sulfur battery by 13 % for low current densities and by 50 % for high current densities.

Finally, a promising powder coating technology is applied in order to coat sulfur-carbon composite powders of cathodes of lithium-sulfur batteries by ALD and in this way considerably improving the performance of those batteries. For this aim, a fluidized bed reactor was constructed. The best results are obtained after applying 5 ALD cycles of Al_2O_3, sufficient to increase the capacity of the system by 30 % at low current densities and by 50 % at high current densities, with respect to a standard battery system. Besides, the sulfur loading in the cathodes can be doubled thanks to the morphological improvement provided by the aluminum oxide. After coating, uniform and crack-free electrodes can be fabricated, which significantly exceed the performance of standard electrodes increasing the capacity of lithium-sulfur batteries by 60 %.

Contents

Chapter 1

Introduction

This chapter gives an introduction to the main topics studied in this thesis, namely, particle technology and energy storage devices. The most relevant works developed so far are highlighted and its contribution to this thesis is explained.

1.1. Particle Technology

1.1.1. Background

Since the industrial revolution, powders have been essential parts of processes. Over 75 % of raw materials and around 50 % of products from the chemical industry fall into the category of particles.[1] Powders are very useful in a wide range of applications and processes. They are usually classified according to their particle size and functionality. Particles in the millimeter range are typically found in alimentary and pharmaceutical sectors, cleaning and construction. In contrast, micrometer- and nanometer-sized particles are more commonly used in energy storage systems, catalysis or electronics.[2], [3] Given the continuous need for improved materials for emerging applications, the research and development of powders for industrial use is growing considerably.

Recent research focuses on micrometer and nanometer scale particle-based technologies due to the special properties associated to the particle size and their large specific surface areas. Powders are intensely investigated for the production of drugs, food, electronics, catalysts and energy storage devices.[4]–[7] In many of those applications, functionalization of particles can greatly improve their performance. One of the most promising ways for improving the performance of particles is the application of a coating around them, forming core-shell nanoparticles as shown in Figure 1,[8] or even the deposition of islands or clusters of further materials on their surface, which brings additional functionalities to the powder, protecting them, activating or changing their performance.

For instance, a facile way to enhance the performance of catalysts was developed by Goulas *et al.*, who deposited platinum (Pt) clusters on TiO_2 particles to increase the active surface area of the Pt catalyst.[9] In another case, for energy storage applications, Beetstra and coworkers deposited a thin film of alumina on the cathode material of Li-ion batteries ($LiMnO_2$ nanoparticles). The film prevented the dissolution of the cathode material into the electrolyte, thus reducing the aging of the battery.[10]–[12] For various applications, SiO_2 nanopowders have been coated with TiO_2 to obtain core-shell nanoparticles.

Thanks to the synthesis of the core-shell structure with its increased surface area, the performance of the TiO_2 is enhanced, and therefore, its photocatalytic and optical properties.[13], [14] All those examples demonstrate that modifying properties of a material at nanometric or micrometric scales can result in macroscopic effects, improving the performance of the material for its final application.

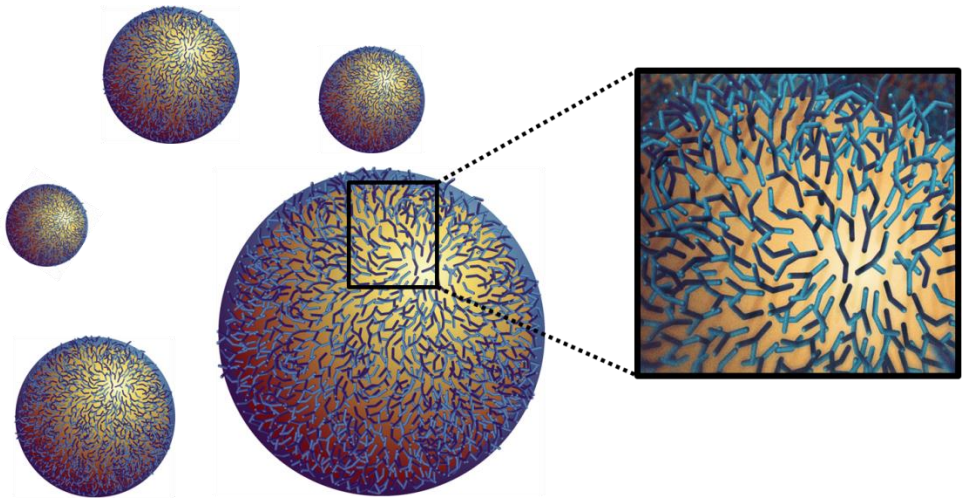

Figure 1. Core-shell particle structure with functional groups on a particle surface.

1.1.2. Coating Technologies

Coating of powders is a straightforward pathway to obtain functional particles. Indeed, in pharmaceutical, biological, food, energy or chemical industries, new materials are achieved by altering the surface properties and/or functionalities of fine particles.[15] Such surface modifications not only enhance the performance of particles, but also lead to the design of advanced and novel materials.

Coatings of particles are typically performed in either of the two ways, wet or dry. The wet particle coating technology, also known as liquid coating, involves solvents in the coating process. The coating agent is dissolved or suspended in a solvent and the resulting liquid is then progressively applied to the particles to be

coated. Once the solvent is evaporated, it leaves behind a solidified coat on the particles. Not many industrial coating processes rely on the liquid coating technology, since the drying stage of solvent evaporation involves long processing times, generates large amounts of waste and considerably consumes energy.[16], [17] Besides, it is difficult to control the thickness of the deposited layers accurately and to assure that they are pinhole-free. Nowadays, the most prominent liquid coating techniques include spray drying,[18] sol-gel coating,[19] or fluid bed coating.[20]

As an alternative, gas-phase processes, also known as dry particle coating, have been developed for coating particles. In this case, the coating agent is dispersed in a gas and added to the system in form of solid particles. The adhesion of the particles to the substrate is achieved by van-der-Waals or electrostatic forces. The particle size of the coating agent is small enough to allow adhesive forces to generate thinner coatings with high accuracy.

A promising technology among the gas phase techniques is the chemical vapor deposition (CVD).[21], [22] This deposition technique is based on the simultaneous injection of two or more vaporized molecular reactants (precursors) into a reaction chamber, which will react with the surface of a substrate. Thus, a coating with a precise control over its thickness, even down to hundreds of nanometers, is deposited. During the 1960s, some initial experiments were done by Russian and Finnish researchers modifying CVD towards ultimate growth control, which marked the beginning of the era of atomic layer deposition (ALD), originally called atomic layer epitaxy (ALE).[23]

1.1.3. Atomic Layer Deposition

Atomic layer deposition (ALD) was intensely investigated and developed during the 1970s by Suntola *et al.* in order to produce high quality ZnS films for thin film electroluminescent (TFEL) flat panel displays.[24] In the early development stage it was called Atomic Layer Epitaxy (ALE), but it was soon realized that the films rarely show epitaxial growth, but were rather amorphous or polycrystalline. Therefore, this new deposition method was renamed to Atomic Layer Deposition

(ALD). The interest in this technology increased in 1990s, especially for microelectronic devices, but it was not until 2000s, when its use grew exponentially, triggered by the need of mass production of thin conformal coatings on high aspect ratio structures.[25]

Atomic layer deposition is a vapor phase thin film deposition technique to create conformal, pinhole free and homogeneous coatings. Similar to CVD, the process is based on the reaction between two or more gaseous precursors, whose surface chemical reaction results in the desired coating material.[26], [27]

In ALD processes one of the precursors, typically an organometallic, metal organic or metal halide molecule, acts as the metal source for the final coat. The other reactant is a counter precursor, like water, ozone, ammonia, hydrogen, or similar, which defines the nature of the deposited material; a pure element, an oxide or a nitride, etc. In ALD processes, the substrate is exposed to each precursor separately, which stands in contrast to CVD, where all precursors are supplied simultaneously to the reaction chamber. Consequently, ALD precursors do not react with each other in the gas phase, but the reaction takes place exclusively at the solid-gas interface. The high precision and controllability of the film growth of ALD is based on the self-terminating nature of the chemical reactions in each cycle. Once the surface is saturated with one precursor, no more reactions take place, even if excess precursor is available in the reaction chamber. The supply of the counter precursor will consequently react with only one layer of the bound primary precursor, thus assuring that a maximum of one monolayer of precursor is formed on the surface in each cycle.[26], [28]–[30]

Aluminum oxide or alumina (Al_2O_3), deposited using trimethylalumininum (TMA), $Al(CH_3)_3$, and water, H_2O, is one of the most studied ALD systems mainly for the following three reasons: (1) alumina can be deposited in a wide range of temperatures and pressures given by the high reactivity of TMA, (2) the deposition of alumina shows the typical linear layer-by-layer growth mechanism of ALD, and (3) it is a facile and economic process if compared to other ALD processes. Figure 2 illustrates the aluminum oxide (Al_2O_3) ALD deposition step by step, described as follows: (1) TMA pulse into the chamber. TMA molecules are

supplied to the reaction chamber by an inert carrier gas, in this case, nitrogen. The molecules react with available functional groups on the surface of the substrate, usually hydroxyl groups (-OH), until surface saturation is reached. (2) Purging of the excess precursor and byproducts (methane, CH_4) out of the reaction chamber by an inert gas. Nitrogen gas is used to remove the excess of TMA and methane molecules. (3) Water vapor supply to the reaction chamber. Using nitrogen as carrier gas, water vapor molecules react with the chemisorbed TMA molecules on the substrate surface, generating the first layer of alumina. (4) Purging of the excess second precursor and the reaction byproduct, methane. This purging step completes an ALD cycle, eliminating the excess of water and methane from the reaction chamber. In each cycle, one alumina layer is deposited; enabling the control of the final thickness of the coating with the number of the applied ALD cycles.

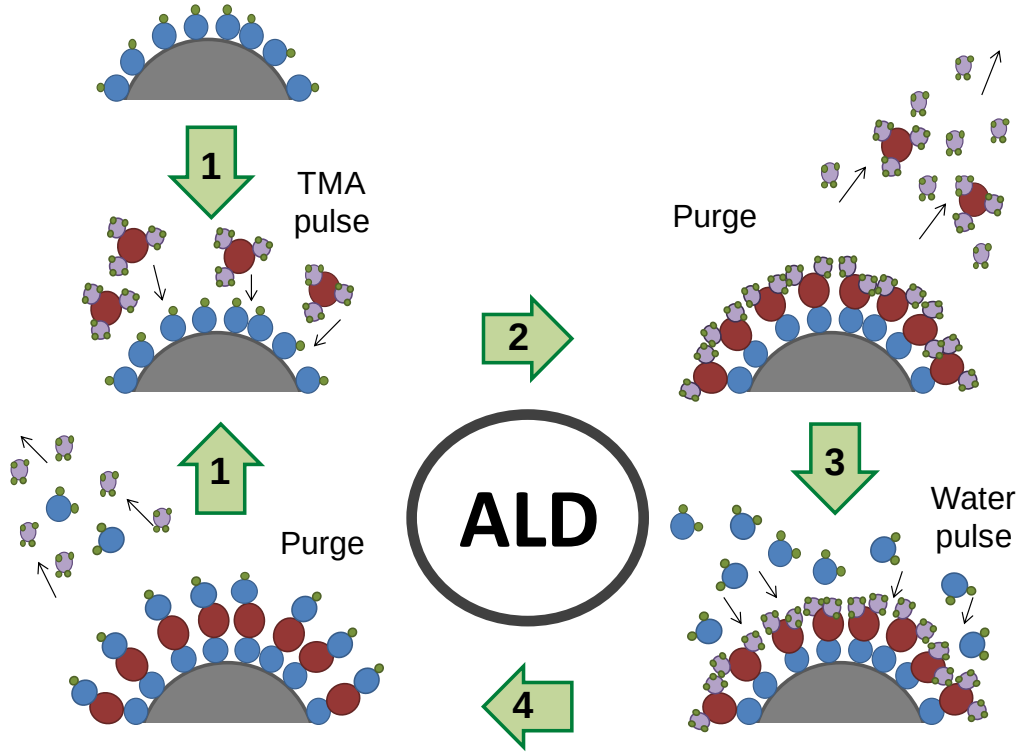

Figure 2. Schematic of the ALD deposition of Al_2O_3 using trimethylaluminium (TMA) and water as precursors.

ALD has been dominantly used to functionalize microelectronic devices, mainly in order to deposit homogeneous and pinhole free high-k dielectric coatings to prevent current leaks through the gate oxide.[31]–[33] More recently, its use was extended to many other applications, such as improved photovoltaic devices [34] or energy storage systems with increased electrochemical performance.[35], [36] The spread of ALD into different fields also brings about the evolution and adaptation of this technology towards substrates with a large variety of geometries, ranging from flat substrates to fine particles.[37]–[39]

The application of ALD to particles, being it continuous or semi-continuous, is increasingly attracting attention thanks to the high surface area of particles and thus their enhanced functionality in comparison to flat substrates. Meanwhile, a variety of reactors have been developed which are suitable for a deposition of nanometer-scaled layers on particles.[40]

1.1.4. ALD reactors for coating particles

The reactors for coating individual particles by means of ALD can be classified as a function of powder particle motion; namely, as static particle reactors and as agitated or fluidized particle reactors.

ALD on static particles

The first experiments for coating powders by ALD were conducted as early as 1992 by Suntola and coworkers in a flow-type ALD reactor, with the goal to obtain active catalyst materials. They used a top-flow reactor with static particles as substrates. The precursor gases were fed from the top of the reactor and then diffused through the bed of particles, before their excess and byproducts were purged through the pumping system connected to the bottom of the reactor.[41] Another experiment was carried out by Ferguson *et al.* in a pump-type ALD reactor at the University of Colorado in the early 2000s. Successful deposition of Al_2O_3 and SiO_2 on boron nitride (BN) particles for thermal applications was obtained using a sample holder as support for the particles.[42]

ALD reactors, where the deposition is carried out on static particles, have shown very good results for a wide range of coatings. However, experiments performed with such configuration are only applicable to small amounts of powders. Figure 3a schematizes such a process, where for small amounts of powders individual particles are coated by ALD, since the precursors reach each particle easily. However, if the amount of particles is large, only the upper fraction of the powder will be completely coated (Figure 3b), since those are rapidly exposed to the precursor gases, similar to a planar substrate. With increasing depth of the powder bed, the coating thickness will decrease, eventually leaving particles in the bulk of the bed uncoated. This effect can be attributed to two factors, namely i) the limited diffusion of the precursor into the bulk of the bed due to more tortuous diffusion paths and therefore longer exposure times required, and ii) the higher consumption of the precursor due to the much larger surface area of the particles if compared to flat substrates. Additionally, if the number of deposited ALD cycles is high, the lack of mobility of the particles will generate continuous and thick coatings, specially on the surface of the bulk, that act as a glue connecting and agglomerating particles to each other. Therefore, conformal coatings are successfully deposited on individual particles by ALD using this technique, but the nature of the set-up is not suitable for up-scaling.[43]

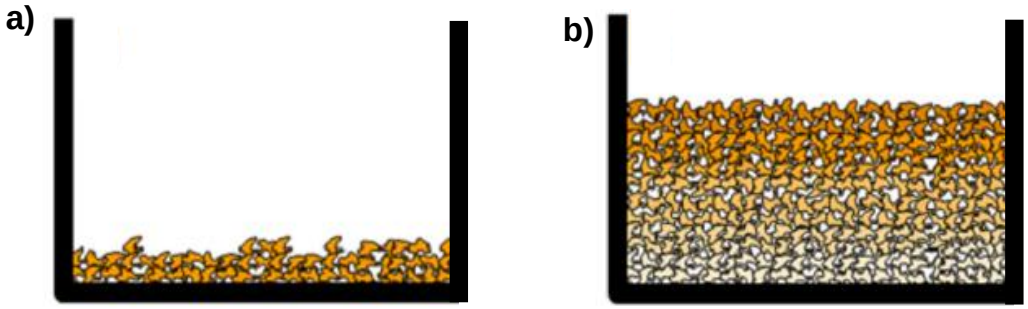

Figure 3. Schematic of static particles coated in a pump-type ALD reactor. The intensity of the coloration indicates the efficiency of the coatings. Image adapted from D. Longrie *et al.*, *Journal of Vacuum Science & Technology A: Vacuum, Surfaces and Films,* **32**, 1 (2014).

In order to uniformly coat large amounts of particles, homogeneous agitation or fluidization of the particles is needed to improve gas and precursors diffusion and reduce the necessary exposure times. One of the most efficient and well-known techniques for this aim is the fluidized bed reactor (FBR), where particles behave like a fluid. More recently, McCormick *et al.* developed also rotatory reactors for ALD.[44] In this case, thanks to the agitation of the particles due to the rotatory movement of the reactor chamber, particles are also coated in a homogeneous manner. While fluidized bed reactors are commonly used for coating microsized or larger particles, rotatory reactors are mostly used for coating nanoparticles with very high surface area, which require very large quantities of precursors. Moreover, depending on the porosity and the tortuous paths for the diffusion of the precursors along the nanoparticles to be coated, much longer residence times are needed to saturate the sample surface.[40] For this reason, a cost effective way for coating nanomaterials with high surface areas and without wasting too much precursor is the use of ALD rotatory reactors.

Given the nature of the materials to be coated in this thesis, the study is performed in a fluidized bed reactor.

ALD on fluidized particles

The fluidization of particles is obtained with a gas introduced upwards with an appropriate flow into the reactor. This process is characterized by a good gas-solid mixing that shows an efficient mass and heat transfer.[40] Fluidized bed reactors (FBR) were studied first by Wank *et al.* for processing large amounts of powders, specifically for coating fine nickel particles with alumina by ALD.[45]

FBRs are well established in industrial applications whenever there is a need for modifying particles, even though those conventionally do not use ALD, but other chemical coating processes like chemical vapor deposition (CVD). The amount of powder which can be processed in an FBR is significantly higher than in static-type ALD reactors. Appropriate design for an ALD process ensures a scale-up of ALD-type of powder coatings for industrial applications.

However, the fluidization behavior of the particles is dependent on their size and density. The Geldart diagram, shown in Figure 4, describes four main groups of particles. (1) Type A particles are characterized by uniform fluidization. A typical example would be cracking catalysts. (2) Type B particles have larger sizes than type A particles. As soon as the fluidization starts, bubbling occurs. Sand is the most prominent example of this class of particles. (3) Type C particles are very fine, at the nanometer scale, which tend to fluidize in a homogeneous manner. Usually, agglomerates are generated due to the small particle size and the resulting stronger cohesion forces. (4) Type D particles are the largest particles among this classification, with high densities, like grains or beans. Strong gas flows are required to fluidize this type of particles and usually, spouting occurs during the fluidization process.[46]

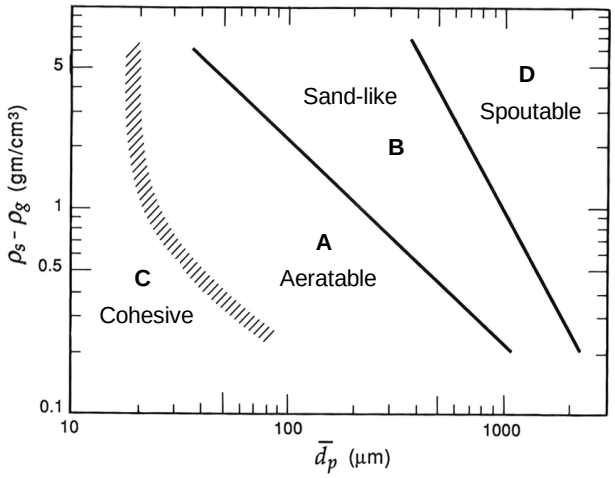

Figure 4. Geldart diagram of the particle fluidization behavior as a function of particle size and density. Figure adapted from H.A. Khawaja, *International Journal of Multiphysics* **9**, 4 (2015).

During the fluidization process agglomerates may be formed, which occurs due to van-der-Waals interactions, liquid or humidity bridging, or electrostatic forces. Thus, the coating process may result in a poor fluidization behavior, in which the particle bed is not homogeneously mixed, and therefore, channels and dead zones,

that decrease the fluidization of particles, can appear.[47] As solution to overcome this issue, additional assistive methods are attached to the reactor, which should help to break agglomerates during the process, thus improving the fluidization efficiency. The most efficient techniques are mechanical stirring,[48] mechanical vibration[49] and ultrasound.[50] In such cases, particle fluidization happens dynamically, ensuring that agglomerates break and recombine continuously as a result of agglomerate-agglomerate and agglomerate-wall collisions.[46] In this way, a proper coating (continuous or semi-continuous) of each particle is ensured.

The good processing properties of fluidized bed reactors, and its versatility and precise control over the film thickness, make ALD-FBR an interesting approach for powder coatings, not only for research purposes, but also for scale-up and industrial production. The application of this technology to fabricate materials for energy storage systems is intensely investigated and it is beginning to deliver breakthroughs in a large variety of battery systems.

1.2. Energy storage

1.2.1. Background

Combustion of fossil fuels has been for many years, the main source of energy, a process that releases greenhouse gasses (CO_2, CO or CH_4) as byproduct to our atmosphere. This effect leads to abnormal overheating of the planet and the currently discussed climate change.[51], [52] Renewable energy generation technologies can be a solution to satisfy the growing energy requirements of our society. Solar, wind, hydropower and geothermal technologies, among others, can effectively substitute the conventional methods for energy generation without emission of further greenhouse gases.[53] However, these renewable energy technologies often require specific locations of the plants or do not generate electricity continuously, requiring efficient and reliable energy storage and transport methods.

Energy storage (ES) systems constitute an essential element in the development of sustainable energy technologies, providing great potential to overcome our energy needs in a sustainable way.[54] By now, there is a broad range of developed ES systems that can be classified in mechanical, thermal, chemical, electrochemical and electrical energy storage devices.[55]

The electrochemical energy storage is the most versatile ES system, with applications ranging from stationary plants to small electronic devices. Nowadays, four general types of electrochemical energy storage systems are in use, as shown in Figure 5. Those include capacitors, supercapacitors, batteries and fuel cells.[56], [57] Each system has its own characteristics regarding the storage capacity or energy density, and energy release rate (power density).

Batteries offer an excellent energy storage technology for a better integration of renewable energies into our society. As schematically shown in Figure 6, a battery cell consists of two electrodes, separated by a separator and an electrolyte between the electrodes. Both electrodes are connected through an external circuit. During the discharge, the negative electrode (anode) is oxidized, thereby releasing cations into the electrolyte. Simultaneously, the positive electrode (cathode) is

reduced by binding those ions from the electrolyte. During this process the electrons travel from the anode to the cathode through the external circuit, generating the electrical current.[58] In other words, a battery or voltaic cell is a concept of two half cells bridged with each other to permit the ion transfer. It is based on two half reactions; oxidation in one half cell (electrode) and reduction in the other, resulting in a final redox reaction where energy is converted from chemical to electrical.

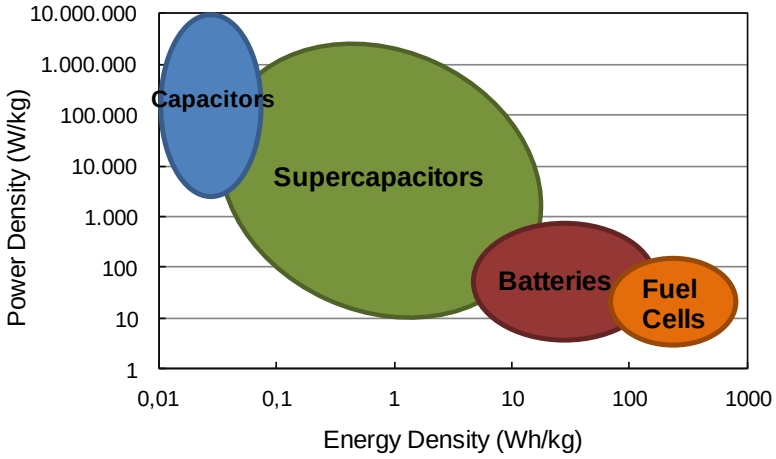

Figure 5. Classification of electrochemical storage systems by energy density vs power density (Ragone plot). Figure adapted from B. K. Kim *et al., Electrochemical Supercapacitors for Energy Storage and Conversion. Handbook of Clean Energy Systems,* (2015).

Considering the reversibility of the redox processes, batteries can be divided into two categories. On the one hand, there are primary batteries, such as zinc-carbon, silver-zinc or lithium primary batteries, where the electrochemical reaction is not reversible. These batteries are not rechargeable and are for a single use only. They provide high energy densities at a low production cost.[59] On the other hand, there are secondary or rechargeable batteries, where the discharge process can be reversed by passing an equivalent current in the opposite direction. The most common rechargeable batteries are lead-acid and nickel-cadmium batteries. More recently, the development of nickel-metal hydride and li-ion batteries has allowed

the revolution of portable electronics (smart phones, laptops, electric cars, etc.). Those battery systems are more compact and have a high energy density along with long cycle life.[60]

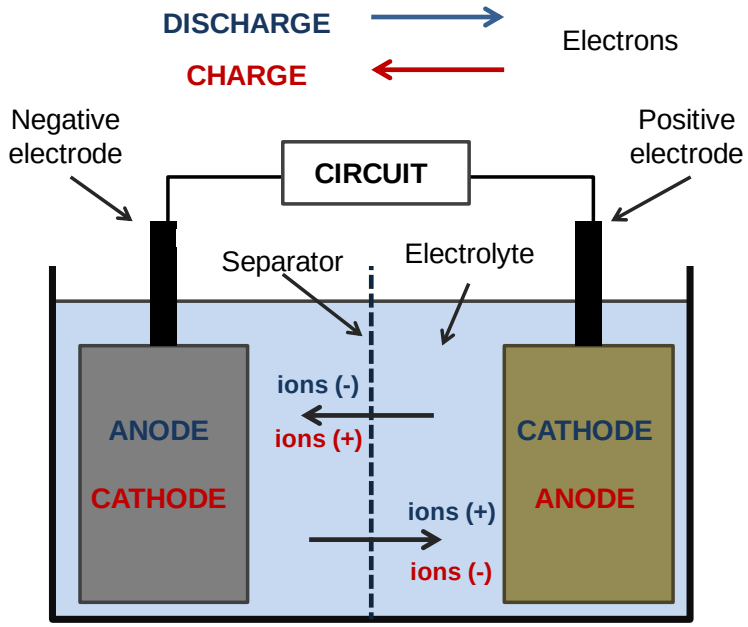

Figure 6. Schematic of the basic constituents of a rechargeable battery in its charge-discharge processes, marked red and blue, respectively.

Lithium-ion batteries (LIB) are currently the most used batteries for portable applications. Their naming indicates their mechanism. Namely, lithium ions are exchanged between the typically graphitic anode and the cathode, usually a ternary lithium-transition metal oxide, like $LiCoO_2$.[61]–[63] With a theoretical energy density of around 300 $Wh \cdot kg^{-1}$, this kind of batteries provides excellent cycling stability, long cycle life and a high C-rate stability.[64] Nowadays, LIBs dominate the market of portable electronics and transport electrification. However, they also suffer from several drawbacks. Firstly, the electrode materials have a limited specific capacity, limiting the energy density of the battery. Secondly, the cathode materials are composed of rare metals, which have impact on the large-scale usability and, consequently, the price in future applications.

These limitations are a driving force to develop further battery technologies, suitable to replace the currently implanted LIB technology.

Lithium has excellent properties, including low density ($0{,}59\ g \cdot cm^{-3}$), high theoretical specific capacity ($3860\ mAh \cdot g^{-1}$), and a sufficiently negative redox potential (-3,04 V), which made the researchers focusing on alternative lithium metal based batteries.[65] In recent years, lithium-air (Li-O_2) and lithium-sulfur (Li-S) batteries have become promising solutions for the next generation of energy storage systems.[66], [67] Although Li-O_2 exhibits higher theoretical energy density than Li-S, the latter one is closer to the real market. This is attributed to the better handling and the exciting properties of sulfur as cathode material in energy storage systems.

1.2.2. Lithium-Sulfur batteries

Sulfur shows an outstanding theoretical specific capacity of $1672\ mAh \cdot g^{-1}$, and a theoretical energy density of $2600\ Wh \cdot kg^{-1}$. Moreover, sulfur is environmentally friendly and one of the most abundant elements on earth, which considerably lowers its price compared to the cathode materials in lithium-ion battery systems.[68]

A conventional lithium-sulfur battery comprises a sulfur-based cathode, a lithium metal anode and a separator soaked in electrolyte as it is shown in Figure 7. The cathode is the most complex part of the battery. It is composed of the active material (here, sulfur), conductive additives (conductive carbon), and a binder. In contrast, as anode a metallic lithium foil is commonly used. A porous polymer is usually used as separator. The electrolyte is a mixture of ether based solvents, namely, 1,3-dioxolane (DOL) and dimethoxyethane (DME) with lithium bis(trifluorosulfonyl imide) (LiTFSI) salt dissolved in it.[69], [70]

During the discharge of the cell, the oxidation happens at the anode, where lithium is oxidized and lithium ions (Li^+) are released to the electrolyte, and the electrons are released into the external circuit (Reaction 1).[71]

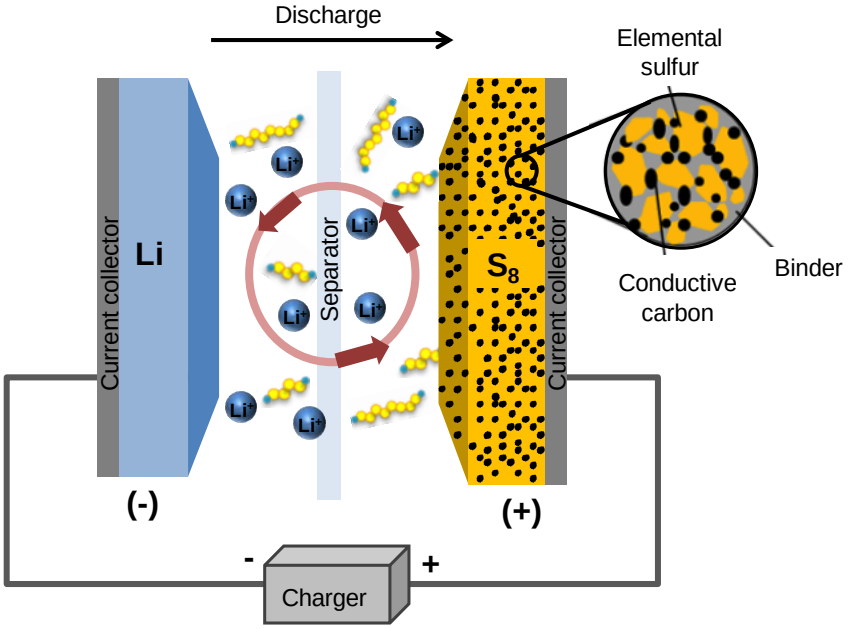

Figure 7. Schematic representation of a lithium-sulfur cell. Figure adapted from *Oxis Energy. Next Generation Battery Technology (https://oxisenergy.com/products/* taken on 02/01/2020*)*

Both, lithium ions and electrons travel to the cathode where the reduction of elemental sulfur occurs (Reaction 2). Following the half reactions (oxidation (1) and reduction (2)) the redox reaction of the whole process is shown in Reaction 3:

$$Li \rightarrow Li^+ + e^- \qquad \text{E=0 V (vs Li/Li}^+\text{)} \qquad (1)$$

$$S + 2e^- \rightarrow S^{2-} \qquad \text{E=2,2 V (vs Li/Li}^+\text{)} \qquad (2)$$

$$S + 2Li^+ + 2e^- \rightarrow Li_2S \qquad \text{E=2,2 V (vs Li/Li}^+\text{)} \qquad (3)$$

The most stable form of elemental sulfur in nature is the octasulfur ring, S_8. Considering this, the redox Reaction 3, can be adjusted as follows (Reaction 4):

$$S_8 + 16Li^+ + 16e^- \rightarrow 8Li_2S \qquad \text{E=2,2 V (vs Li/Li}^+\text{)} \qquad (4)$$

From this reaction, the theoretical specific capacity of sulfur vs lithium is calculated to be 1672 mAh · g^{-1}. Considering that the average potential is around 2,2 V, the theoretical energy density of sulfur vs lithium is around 2600 Wh · kg^{-1}.[69] However, the reduction mechanism of sulfur is more complex than shown in Reaction 4.

As shown in Figure 8, during the discharge process the reduction of sulfur undergoes disproportion reactions of the octasulfur ring, forming higher order lithium polysulfides, Li_2S_8 (Reaction 5).

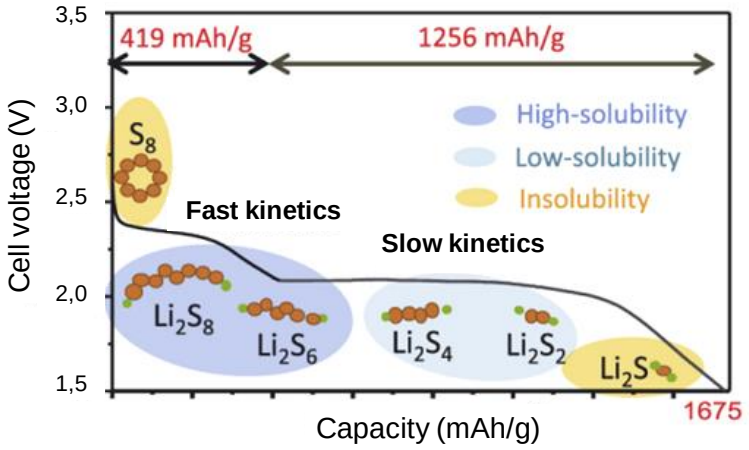

Figure 8. Discharge voltage profiles of sulfur and intermediately formed lithium polysulfides. Image adapted from B. Yan *et al.*, *Journal of Power Sources*, 338 (2017).

The discharge continues via the reduction of Li_2S_8, to further higher order lithium polysulfides, Li_2S_x, where 8>x>6, and subsequently into lower order lithium polysulfides, Li_2S_n, where 6>n>2, both described by the Reaction 6 and Reaction 7, respectively. Finally, the discharge finishes with the products of the reaction of reduced sulfur with lithium, forming lithium disulfide (Li_2S_2) or lithium sulfide (Li_2S) (Reaction 8).

$$S_8 + 2Li^+ + 2e^- \rightarrow Li_2S_8 \qquad \text{E=2,5 V} \quad (\text{vs Li/Li}^+) \qquad (5)$$

$$Li_2S_8 + nLi^+ + ne^- \rightarrow Li_2S_x \quad 8 > x > 6 \quad E=2{,}4\ V \quad (vs\ Li/Li^+) \quad (6)$$

$$Li_2S_x + nLi^+ + ne^- \rightarrow Li_2S_n \quad 6 > n > 2 \quad E=2{,}0\ V \quad (vs\ Li/Li^+) \quad (7)$$

$$Li_2S_x + nLi^+ + ne^- \rightarrow Li_2S \quad E=1{,}7\ V \quad (vs\ Li/Li^+) \quad (8)$$

Even if there is an agreement of the researchers regarding the general redox Reactions (5) to (8), the exact species formed during the battery charge-discharge cycles is controversial. The disproportion reactions that take place are strongly dependent on many details of the battery, such as, the amount of electrolyte, salts, battery configuration, and operating voltage, among others.

1.2.3. Drawbacks in Lithium-Sulfur batteries

Lithium-sulfur batteries stand out due to their exciting theoretical electrochemical properties. However, there are several factors that negatively affect this battery system:

Insulating nature of sulfur

The most important drawback to overcome in lithium sulfur batteries is the insulating nature of sulfur, the active material. Its electrical conductivity is around $10^{-30}\ S \cdot cm^{-1}$, which is a true obstacle for the electrochemical utilization of a high percentage of this active material in the cathode.[72] The common strategy to solve this issue is to confine sulfur in a conductive matrix like carbon, polymers or other organic materials, and afterwards disperse and fix it in the conductive matrix by thermal treatments. This approach adds complexity to the cathode and implies a need to investigate secondary problems, including processing of the cathode, its scalability, and the sulfur loading.

Polysulfides dissolution "Shuttle effect"

When the battery discharge is taking place, the reduction of sulfur passes through several lithium polysulfides intermediates (see Figure 8).[73], [74] Those

intermediate polysulfides are soluble in the electrolyte and tend to migrate towards the anode, where they become reduced by reacting with lithium to lower order lithium polysulfides. Some of those polysulfides can be further reduced to Li_2S, becoming insoluble and forming an ionically insulating and irreversible interface, the so-called Solid Electrolyte Interface (SEI), thus passivating the anode's surface. This effect leads to a self-discharge of the battery and a low Coulombic efficiency, as well as cathode degradation, due to the active material loss and passivation of the anode.[75]

Structural changes

The structural changes during charge-discharge processes of the battery (sulfur solid to liquid and vice versa) and density differences between elemental sulfur (2,07 $g \cdot cm^{-3}$) and lithium sulfide (1,66 $g \cdot cm^{-3}$) lead to a mechanical stress in the cathode, resulting in cracking, delamination and loss of the integrity of the cathode structure, eventually ending in a cell failure.[76], [77]

Lithium anode

The lithium metal, used as anode of Li-S batteries, easily reacts with the solvents in the electrolyte, resulting in a decrease of the Coulombic efficiency of the system.[78] Moreover, the non-homogeneous deposition and dissolution of lithium during the charge-discharge processes leads to the growth of lithium dendrites. Those dendrites can grow perpendicular to the anode into the electrolyte, through the separator and further to the cathode. Upon physical contact with the cathode, a short circuit of the battery will occur. Furthermore, the inhomogeneous dispersion of lithium in the formed dendrites, can cause breaks and result in inactive lithium in the electrolyte, reducing the efficiency and stability of the lithium anode and reacting with the electrolyte by consuming it, thus causing a lower cycle life.[79]

1.2.4. ALD on Lithium-Sulfur batteries

With the significant obstacles that have been found in lithium-sulfur batteries, it is imperative to focus the attention on developing Li-S batteries with high energy

density and long-term stability by suppressing, overcoming or minimizing the described drawbacks. The design of effective strategies to address the insulating nature of sulfur, the volume effect of the cathode, the shuttle effect of soluble polysulfides and safety hazard of the Li metal anode is becoming very challenging.[80]

ALD has exceptional capabilities in developing conformal films with precise control. It has demonstrated to be a promising strategy for solving emerging issues in advanced energy storage devices via surface modification and fabrication of various functional materials. Badot *et al.* successfully deposited V_2O_5 films by ALD that served as LIB cathodes.[81] Thereafter, more extensive ALD coatings were done for components in Li-ion batteries. More recently, ALD experiments were performed to improve Li-S batteries. Kim *et al.* conducted the first study of applying ALD-Al_2O_3 on a sulfur cathode.[82] In that work, sulfur-carbon composite cathodes were fabricated and further coated with alumina using a plasma-enhanced chamber-type ALD reactor. The ALD-modified cathodes exhibited an evident increase in the system capacity, doubling it after a certain number of cycles, if compared to untreated cathodes. In a similar work by Yu *et al.* graphene-based sulfur composites were coated with Al_2O_3 by ALD. The circularly shaped composite pellets were coated in a chamber-type ALD reactor, where the assembly of pellets was static. The alumina coating reduced the dissolution of lithium polysulfides and increased the stability of the graphene-sulfur composite.[83]

In order to improve the conductivity of the sulfur-containing cathode and in this way maximize the utilization of sulfur, Meng *et al.* prepared nanoscaled sulfur particles by ball-milling of micrometer sized sulfur particles, thereby achieving higher efficiency and capacity of the battery system. In their work they deposited Al_2O_3 on the sulfur nanoparticles in a chamber-type ALD reactor with a static particle assembly. The deposition of Al_2O_3 by ALD showed different kinds of coverages of the sulfur cathodes as a function of the number of ALD cycles; dispersed nanoparticles (5-20 ALD cycles), porous nanofilms (50 ALD cycles) and uniform dense nanofilms (100 ALD cycles). Very interestingly, the morphology of the deposited coating revealed two different mechanisms for improving the

performance of the resulting sulfur cathodes, which are resulting from the alumina coating. For low ALD cycle numbers (<20 cycles), alumina was deposited on sulfur discontinuously, as islands, acting as exceptional absorbent of polysulfides. For larger numbers of ALD cycles (≥50 cycles) Al_2O_3 formed a porous film over the cathode and acted as a physical barrier, inhibiting polysulfides from contacting and dissolving into the liquid electrolyte. In the case of thick alumina coatings (100 cycles) the electrochemical reactions of the sulfur electrode were restricted due to the uniform and dense coating of insulating alumina. As a result, they identified that 5 ALD cycles of Al_2O_3 deposition were sufficient to increase the capacity of Li-S batteries by 50% in comparison to the bare sulfur cathode.[84]

In all mentioned cases, ALD was used to improve the lithium-sulfur battery system by altering the cathode materials. The deposition of a specific material at the nanometer scale has many and unique benefits for improving the behavior of Li-S batteries, increasing its capacity and power density, in addition to its excellent properties over the control of the materials growth given by ALD.

1.3. Overview of this thesis

The aim of this thesis is to study and understand the functionalization of powders by ALD, especially for energy storage applications in lithium-sulfur batteries. Micro- and nano-sized particles of inorganic materials have been coated with metal oxides, showing promising results and new functionalities that have not been observed before. The thesis is composed of 6 chapters:

Chapter 1 shows an overview of the topical area. Both, particle coating technologies and energy storage devices are introduced. The state-of-the-art of each technology and the combination thereof is reviewed as introduction to the work performed in the course of the present thesis.

Chapter 2 describes the experimental techniques and methods utilized in this thesis for the physicochemical characterization of the studied samples.

Chapter 3 describes an initial study of particle coatings by ALD. For this aim, iron oxide particles (γ-Fe_2O_3) are coated with titanium dioxide (TiO_2), generating

FeO_x-TiO_2 core-shell nanoparticles. The study shows that ALD technology not only grows TiO_2 coatings around particles, but also a reduction of γ-Fe_2O_3 particles to Fe_3O_4 occurs as a side effect, which is analyzed in more detail theoretically and experimentally.

Chapter 4 presents the modification of cathode materials of lithium-sulfur batteries by ALD in a conventional static reactor. Alumina is deposited on prefabricated cathodes applying various processing temperatures. The results show an improved performance of the resulting ALD modified batteries in form of an increase of the efficiency and capacity of the battery.

Chapter 5 describes the coating of sulfur-carbon composite powders, which are subsequently used to assemble cathodes for lithium-sulfur batteries. Al_2O_3 is deposited by ALD in a home-made fluidized bed reactor. This novel experiment has not been done before and it shows promising results for the scale-up of the process to coat large amounts of composite powders. The coated powders show improvements in the efficiency and capacity of the assembled battery.

Chapter 6 summarizes the main results and conclusions obtained from this thesis and proposes further steps, which are necessary to further develop the line of study of this thesis.

References

[1] Kalman, H., Tardos, G. I. Elements of particle technology in the chemical industry. *Part. Sci. Technol.* **23**, 1–19 (2005).

[2] Stark, W. J., Stoessel, P. R., Wohlleben, W., Hafner, A. Industrial applications of nanoparticles. *Chem. Soc. Rev.* **44**, 5793–5805 (2015).

[3] Santos, C., Gabriel, B., Blanchy, M., Neto, V., Santos, C. S. C., Menes, O., García, D., Blanco, M., Arconada, N. Industrial applications of nanoparticles-a prospective overview. *Mater. Today Proc.* **2**, 456-465 (2015).

[4] Rizvi, S. A. A., Saleh, A. M. Applications of nanoparticle systems in drug delivery technology. *Saudi Pharm. J.* **26**, 64–70 (2018).

[5] Zhang, S., Liu, M., Liu, W., Liu, Y., Li, Z., Wang, X., Yang, F. Absorption enhancement in thin film solar cells with bilayer silver nanoparticle arrays. *J. Phys. Commun.* **2**, 1–8 (2018).

[6] Moshfegh, A. Z. Nanoparticle catalysts. *J. Phys. D. Appl. Phys.* **42**, 1–30 (2009).

[7] Liu, N., Li, W., Pasta, M., Cui, Y. Nanomaterials for electrochemical energy storage. *Front. Phys.* **9**, 323–350 (2014).

[8] Chaudhuri, R. G., Paria, S. Core/Shell Nanoparticles : Classes, Properties, Synthesis Mechanisms, Characterization, and Applications. *Chem. Rev.* **112**, 2373–2433 (2012).

[9] Goulas, A., van Ommen, J. R. Scalable production of nanostructured particles using atomic layer deposition. *KONA Powder Part. J.* **31**, 234–246 (2014).

[10] Beetstra, R., Nijenhius, J., Kelder, E. M., Ruud van Ommen, J. Improved Li-Ion Battery Performance by Coating Cathode Nano-Particles using Atomic Layer Deposition. *12th Int. Conf. Fluid. - New Horizons Fluid.*

Eng. 369–376 (2007).

[11] Beetstra, R., Lafont, U., Nijenhuis, J., Kelder, E. M., Van Ommen, J. R. Atmospheric pressure process for coating particles using atomic layer deposition. *Chem. Vap. Depos.* **15**, 227–233 (2009).

[12] Jung, Y. S., Cavanagh, A. S., Dillon, A. C., Groner, M. D., George, S. M., Lee, S. H. Enhanced stability of $LiCoO_2$ cathodes in lithium-ion batteries using surface modification by atomic layer deposition. *J. Korean Ceram. Soc.* **47**, 61–65 (2010).

[13] Didden, A. P., Middelkoop, J., Besling, W. F. A., Nanu, D. E., Van De Krol, R. Fluidized-bed atomic layer deposition reactor for the synthesis of core-shell nanoparticles. *Rev. Sci. Instrum.* **85**, 013905 (2014).

[14] Ullah, S., Ferreira-Neto, E. P., Pasa, A. A., Alcântara, C. C. J., Acuña, J. J. S., Bilmes, S. A., Martínez Ricci, M. L., Landers, R., Fermino, T. Z., Rodrigues-Filho, U. P. Enhanced photocatalytic properties of core-shell SiO_2-TiO_2 nanoparticles. *Appl. Catal. B Environ.* **179**, 333–343 (2015).

[15] Chavda, V. P., Soniwala, M. M., Chavda, J. R. Particle coating: From conventional to advanced. *Int. J. Pharm. Med. Res.* **1**, 1–17 (2013).

[16] Saleh, K., Guigon, P. Coating and encapsulation processes in powder technology. *Handbook of Powder Technology.* **11**, 323-375 (2007).

[17] Lip, S. P., Kowarskiy, C. R., Feldl, K. M., Grim, W. M. Recent Advances in Microencapsulation Technology and Equipment. *Drug Dev. Ind. Pharm.* **14**, 353–376 (1988).

[18] Santos, D., Maurício, A. C., Sencadas, V., Santos, J. D., Fernandes, M. H., Gomes, P. S. Spray Drying: An Overview. *Biomater. - Phys. Chem. - New Ed.* (2018).

[19] Sajjadi, S. P. Sol-gel process and its application in Nanotechnology. *J. Polym. Eng. Technol.* **13**, 38–41 (2005).

[20] Dewettinck, K., Huyghebaert, A. Top-Spray Fluidized Bed Coating: Effect

of Process Variables on Coating Efficiency. *LWT - Food Sci. Technol.* **31**, 568–575 (1998).

[21] Choy, K. L. Chemical vapour deposition of coatings. *Prog. Mater. Sci.* **48**, 57–170 (2003).

[22] Creighton, J. R., Ho, P. Introduction to chemical vapor deposition (CVD). *ASM Int.* 1–10 (2001).

[23] George, S. M. Atomic layer deposition: an overview. *Chem. Rev.* **110**, 111–131 (2009).

[24] Suntola, T., Antson, J. Method for Producing Compound Thin Films. *United States Patent* (1977).

[25] Leskelä, M., Ritala, M. Atomic Layer Deposition Chemistry: Recent Developments and Future Challenges. *Angew. Chemie - Int. Ed.* **42**, 5548–5554 (2003).

[26] Parsons, G. N., George, S. M., Knez, M. Progress and future directions for atomic layer deposition and ALD-based chemistry. *MRS Bull.* **36**, 865–871 (2011).

[27] Puurunen, R. L. A short history of atomic layer deposition: Tuomo Suntola's atomic layer epitaxy. *Chem. Vap. Depos.* **20**, 332–344 (2014).

[28] Johnson, R. W., Hultqvist, A., Bent, S. F. A brief review of atomic layer deposition: From fundamentals to applications. *Mater. Today* **17**, 236–246 (2014).

[29] Pinna, N., Knez, M. Atomic Layer Deposition of Nanostructured Materials. *Whiley-VCH* (2012).

[30] Leskelä, M., Ritala, M. Atomic layer deposition (ALD): From precursors to thin film structures. *Thin Solid Films* **409**, 138–146 (2002).

[31] Gordon, R. G. Review of Recent Progress in Atomic Layer Deposition (ALD) of Materials for Micro- and Nano-electronics. *Polym. Mater. Sci.*

Technol. Repr. **90,** 726–728 (2004).

[32] Puurunen, R. L. Surface chemistry of atomic layer deposition: A case study for the trimethylaluminum/water process. *J. Appl. Phys.* **97** (2005).

[33] Mistry, K., Allen, C., Auth, C., Beattie, B., Bergstrom, D., Bost, M., Brazier, M., Buehler, M., Cappellani, A., Chau, R., Choi, C., Ding, G., Fischer, K., Ghani, T., Grover, R., Han, W., Hanken, D. *et al.* Electron Devices Meeting 2007, IEDM 2007,. *IEEE Int.* 247–250 (2007).

[34] Bakke, J. R., Pickrahn, K. L., Brennan, T. P., Bent, S. F. Nanoengineering and interfacial engineering of photovoltaics by atomic layer deposition. *Nanoscale* **3**, 3482–3508 (2011).

[35] Bachmann, J. Atomic Layer Deposition in Energy Conversion Applications. *Whiley-VCH* (2017).

[36] Oviroh, P. O., Akbarzadeh, R., Pan, D., Coetzee, R. A. M., Jen, T.-C. New development of atomic layer deposition: processes, methods and applications. *Sci. Technol. Adv. Mater.* **20**, 465–496 (2019).

[37] Naumann, V., Otto, M., Wehrspohn, R. B., Werner, M., Hagendorf, C. Interface and material characterization of thin ALD-Al_2O_3 layers on crystalline silicon. *Energy Procedia* **27**, 312–318 (2012).

[38] Wank, J. R., George, S. M., Weimer, A. W. Nanocoating individual cohesive boron nitride particles in a fluidized bed by ALD. *Powder Technol.* **142**, 59–69 (2004).

[39] Weimer, A. W. Particle atomic layer deposition. *Journal of Nanoparticle Research.* **21,** 1-42 (2019).

[40] Longrie, D., Deduytsche, D., Detavernier, C. Reactor concepts for atomic layer deposition on agitated particles: A review. *J. Vac. Sci. Technol. A Vacuum, Surfaces, Film.* **32**, 010802 (2014).

[41] Lakomaa, E. L., Haukka, S., Suntola, T. Atomic layer growth of TiO_2 on silica. *Appl. Surf. Sci.* **60–61**, 742–748 (1992).

[42] Ferguson, J. D., Weimer, A. W., George, S. M. ALD of Al_2O_3 and SiO_2 on BN particles using sequential surface reaction. *Appl. Surf. Sci.* **162**, 280–292 (2000).

[43] Longrie, D. Atomic Layer Deposition for Surface Engineering of Powders. (2013).

[44] Mccormick, J. A. Atomic Layer Deposition on Nanoparticles in a Rotatory Reactor. (2007).

[45] Wank, J. R., George, S. M., Weimer, A. W. Coating fine nickel particles with Al_2O_3 utilizing an atomic layer deposition-fluidized bed reactor (ALD-FBR). *J. Am. Ceram. Soc.* **87**, 762–765 (2004).

[46] van Ommen, J. R., Valverde, J. M., Pfeffer, R. Fluidization of nanopowders: A review. *J. Nanoparticle Res.* **14**, 1–29 (2012).

[47] Sundaresan, S. Instabilities in Fluidized Beds. *Annu. Rev. Fluid Mech.* **35**, 63–88 (2003).

[48] Nam, C. H., Pfeffer, R., Dave, R. N., Sundaresan, S. Aerated Vibrofluidization of Silica Nanoparticles. *AIChE J.* **50**, 1776–1785 (2004).

[49] King, D. M., Liang, X., Zhou, Y., Carney, C. S., Hakim, L. F., Li, P., Weimer, A. W. Atomic layer deposition of TiO_2 films on particles in a fluidized bed reactor. *Powder Technol.* **183**, 356–363 (2008).

[50] Zhu, C., Liu, G., Yu, Q., Pfeffer, R., Dave, R. N., Nam, C. H. Sound assisted fluidization of nanoparticle agglomerates. *Powder Technol.* **141**, 119–123 (2004).

[51] Panwar, N. L., Kaushik, S. C., Kothari, S. Role of renewable energy sources in environmental protection: A review. *Renew. Sustain. Energy Rev.* **15**, 1513–1524 (2011).

[52] Owusu, P. A., Asumadu-Sarkodie, S. A review of renewable energy sources, sustainability issues and climate change mitigation. *Cogent Eng.* **3**, 1167990 (2016).

[53] Mohtasham, J. Review Article-Renewable Energies. *Energy Procedia* **74**, 1289–1297 (2015).

[54] Larcher, D., Tarascon, J. M. Towards greener and more sustainable batteries for electrical energy storage. *Nat. Chem.* **7**, 19–29 (2015).

[55] Ibrahim, H., Ilinca, A., Perron, J. Energy storage systems-Characteristics and comparisons. *Renew. Sustain. Energy Rev.* **12**, 1221–1250 (2008).

[56] Dunn, B., Kamath, H., Tarascon, J. M. Electrical energy storage for the grid: A battery of choices. *Science (80).* **334**, 928–935 (2011).

[57] Chen, H., Cong, T. N., Yang, W., Tan, C., Li, Y., Ding, Y. Progress in electrical energy storage system: A critical review. *Prog. Nat. Sci.* **19**, 291–312 (2009).

[58] Schmidt-Rohr, K. How Batteries Store and Release Energy: Explaining Basic Electrochemistry. *J. Chem. Educ.* **95**, 1801–1810 (2018).

[59] Viswanathan, B. Batteries. Energy Sources (2017).

[60] Poullikkas, A. A comparative overview of large-scale battery systems for electricity storage. *Renew. Sustain. Energy Rev.* **27**, 778–788 (2013).

[61] Korthauer, R. Lithium-ion batteries: Basics and applications. *Lithium-Ion Batter. Basics Appl.* 1–413 (2018).

[62] Goodenough, J. B., Park, K.-S. The Li-Ion Rechargeable Battery: A Perspective. *J. Am. Chem. Soc.* **135**, 1167–1176 (2013).

[63] Armand, M., Tarascon, J. M. Building better batteries. *Nature* **451**, 652–657 (2008).

[64] Nazar, L. F., Cuisinier, M., Pang, Q. Lithium-sulfur batteries. *Mater. Res. Soc.* **39**, 436–442 (2014).

[65] Choi, J. W., Aurbach, D. Promise and reality of post-lithium-ion batteries with high energy densities. *Nat. Rev. Mater.* **1**, 1–16 (2016).

[66] Carbone, L., Greenbaum, S. G., Hassoun, J. Lithium sulfur and lithium oxygen batteries: New frontiers of sustainable energy storage. *Sustain. Energy Fuels* **1**, 228–247 (2017).

[67] Bruce, P. G., Freunberger, S. A., Hardwick, L. J., Tarascon, J. M. Li-O_2 and Li-S batteries with high energy storage. *Nat. Mater.* **11**, 19–29 (2012).

[68] Boyd, D. A. Sulfur and Its Role In Modern Materials Science. *Angew. Chemie - Int. Ed.* **55**, 15486–15502 (2016).

[69] Seh, Z. W., Sun, Y., Zhang, Q., Cui, Y. Designing high-energy lithium-sulfur batteries. *Chem. Soc. Rev.* **45**, 5605–5634 (2016).

[70] Li, G., Li, Z., Zhang, B., Lin, Z. Developments of electrolyte systems for lithium-sulfur batteries: A review. *Front. Energy Res.* **3**, 1–12 (2015).

[71] Wild, M., O'Neill, L., Zhang, T., Purkayastha, R., Minton, G., Marinescu, M., Offer, G. J. Lithium sulfur batteries, a mechanistic review. *Energy Environ. Sci.* **8**, 3477–3494 (2015).

[72] Chung, S. H., Chang, C. H., Manthiram, A. Progress on the Critical Parameters for Lithium–Sulfur Batteries to be Practically Viable. *Adv. Funct. Mater.* **28**, 1801188 (2018).

[73] Kolosnitsyn, V. S., Karaseva, E. V. Lithium-sulfur batteries: Problems and solutions. *Russ. J. Electrochem.* **44**, 506–509 (2008).

[74] Ren, W., Ma, W., Zhang, S., Tang, B. Recent advances in shuttle effect inhibition for lithium sulfur batteries. *Energy Storage Mater.* **23**, 707-732 (2019).

[75] Li, G., Wang, S., Zhang, Y., Li, M., Chen, Z., Lu, J. Revisiting the Role of Polysulfides in Lithium–Sulfur Batteries. *Adv. Mater.* **30**, 1705590 (2018).

[76] Lv, D., Zheng, J., Li, Q., Xie, X., Ferrara, S., Nie, Z., Mehdi, L. B., Browning, N. D., Zhang, J. G., Graff, G. L., Liu, J., Xiao, J. High Energy Density Lithium-Sulfur Batteries: Challenges of Thick Sulfur Cathodes.

Adv. Energy Mater. **5**, 1402290 (2015).

[77] Ye, Y., Wu, F., Liu, Y., Zhao, T., Qian, J., Xing, Y., Li, W., Huang, J., Li, L., Huang, Q., Bai, X., Chen, R. Toward Practical High-Energy Batteries: A Modular-Assembled Oval-Like Carbon Microstructure for Thick Sulfur Electrodes. *Adv. Mater.* **29**, 1700598 (2017).

[78] Cheng, X. B., Huang, J. Q., Zhang, Q. Review - Li metal anode in working lithium-sulfur batteries. *J. Electrochem. Soc.* **165**, A6058–A6072 (2018).

[79] Yan, C., Zhang, X. Q., Huang, J. Q., Liu, Q., Zhang, Q. Lithium-Anode Protection in Lithium–Sulfur Batteries. *Trends Chem.* **1**, 693-704 (2019).

[80] Yan, B., Li, X., Bai, Z., Song, X., Xiong, D., Zhao, M., Li, D., Lu, S. A review of atomic layer deposition providing high performance lithium sulfur batteries. *J. Power Sources* **338**, 34–48 (2017).

[81] Badot, J. C., Ribes, S., Yousfi, E. B., Vivier, V., Pereira-Ramos, J. P., Baffler, N., Lincot, D. Atomic layer epitaxy of vanadium oxide thin films and electrochemical behavior in presence of lithium ions. *Electrochem. Solid-State Lett.* **3**, 485–488 (2000).

[82] Kim, H., Lee, J. T., Lee, D., Magasinski, A., Cho, W. Plasma-Enhanced Atomic Layer Deposition of Ultrathin Oxide Coatings for Stabilized Lithium – Sulfur Batteries. *Adv. Energy Mater.* **3**, 1308–1315 (2013).

[83] Yu, M., Yuan, W., Li, C., Hong, J., Shi, G. Performance enhancement of a graphene – sulfur composite as a lithium – sulfur battery electrode by coating with an ultrathin Al_2O_3 film via atomic layer deposition. *J. Mater. Chem. A* **2**, 7360–7366 (2014).

[84] Meng, X., Liu, Y., Cao, Y., Ren, Y., Lu, W., Elam, J. W. High-Performance High-Loading Lithium – Sulfur Batteries by Low Temperature Atomic Layer Deposition of Aluminum Oxide on Nanophase S Cathodes. *Adv. Mater. Interfaces* **4**, 1700096 (2017).

Chapter 2

Experimental techniques and methods

In this chapter the experimental techniques and methods used in this thesis are overviewed. All applied characterization tools related to physical, chemical, structural and electrochemical characterization, are briefly described. The specific experimental conditions of each method are detailed in the corresponding sections of the Chapters 3, 4 and 5.

2.1. X-ray Diffractometry (XRD)

X-ray diffractometry (XRD) characterization allows the analysis of the crystallinity of a material. Commonly, it is used for the identification of a crystalline material, for the determination of different phases in a polymorphic material and for the quantification of a crystalline phase. In XRD constructive interferences of monochromatic X-rays that interact with a crystalline sample, are analyzed. During the measurement, a monochromatic X-ray beam irradiates the sample at a grazing incident angle θ and the detector collects the reflected beam at an angle 2θ with respect to the incident beam, as schematically shown in Figure 9.

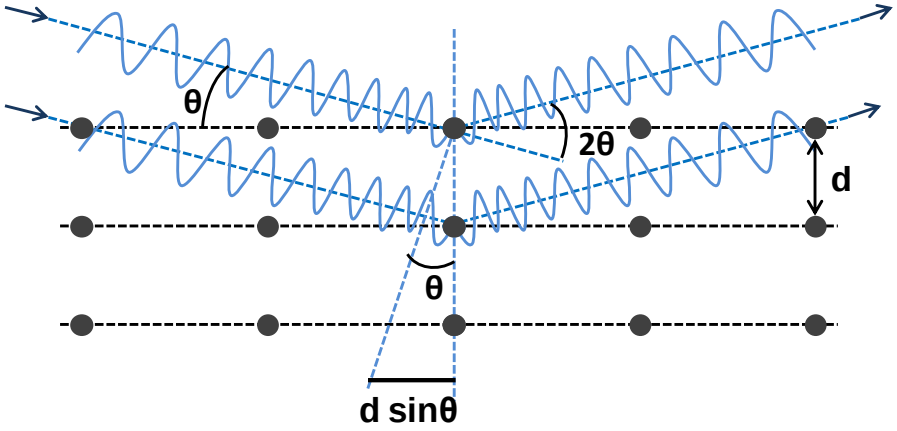

Figure 9. Schematic of the XRD principle. An X-ray beam irradiates a crystal at a grazing incident angle θ and it is scattered by the atoms in the crystal. When the Bragg's condition is fulfilled, characteristic peaks, resulting from constructive interferences, create a reflected peak characteristic of the crystalline material.

The interaction between the incident X-ray beam with the sample produces constructive interferences. When the conditions are in agreement with Bragg's law (Equation 1) a peak will appear in the reflected beam.[1]

$$2d\sin\theta = n\lambda \tag{1}$$

where d is the spacing between the diffracting planes, θ is the incident angle of the beam and λ is the wavelength of the beam. Thus, analyzing the information provided by the reflected peaks, the different crystalline planes present in the analyzed samples are obtained.

In this thesis, the XRD measurements were carried out by using the X-ray diffractometer X'Pert PANalytical, with a Cu Kα (λ=0,154 nm) radiation source. During the measurements, the working voltage and current were 45 kV and 40 mA, respectively. Since all measured samples were powders, the equipment was used in the X-ray powder diffraction mode, where the sample is rotated during the measurements to increase the probability of obtaining diffraction patterns.

2.2. Magnetometric measurements

Magnetometry refers to a broad class of experimental techniques that are used for the macroscopic characterization of magnetic properties. Magnetometers can be classified as (i) AC types, which measure magnetic properties using fields that vary relatively rapidly in time, and (ii) DC types, which measure in quasi-static fields. In this thesis, DC type measurements have been performed in order to characterize the magnetic properties of the studied samples. Among the different possible studies that can be performed with DC measurements, the analysis of magnetization as a function of the temperature, M(T), is most common. In this case, two approaches are used for the analysis: Zero-field cooling (ZFC) and Field cooling (FC). In ZFC, the sample is cooled down without any applied field. Then, at low temperatures, a small magnetic field is applied, and finally, the temperature is incrementally increased while the magnetization is measured in each increment. On the other hand, in FC, the sample is cooled down in presence of a magnetic field, typically the same as the one used for the ZFC measurement, and the magnetization is stepwise measured during warming while the magnetic field is maintained. From the measurements one can extract the various magnetic transition temperatures, such as, Curie, Néel and blocking temperature.[2] From the shape of the curves, indirect qualitative information of interparticle dipolar interactions or the particle size distribution can be obtained.

In order to carry out the experiments, the superconducting quantum interference device (SQUID) magnetometry system has been used. This technique requires the sample to be placed inside the magnetometer. By measuring its total magnetic moment as a function of temperature and magnetic field, it provides information about the type of magnetic ordering, as well as the presence of any phase transition that occurs at a critical temperature or magnetic field.

2.2.1. Superconducting Quantum Interference Device (SQUID)

The Superconducting Quantum Interference Device (SQUID) magnetometer is very sensitive to extremely weak magnetic signals. This instrument allows measuring the magnetization and/or the DC-susceptibility of the sample. It is based on superconducting loops containing Josephson junctions.[3] Those junctions allow to measure small variations of the magnetic flux inside the coil. A DC current is applied to the SQUID coil, and the sample placed in the center of the detectors is moved perpendicularly to generate a magnetic flux that can create voltage changes in the junctions, which allows to measure the magnetization of the sample.

The detection coils, the connecting wires and the input coils form a closed superconductive circuit, as shown in Figure 10. The SQUID and detection coils are a concentric superconducting DC magnet, which allows to apply the external magnetic field to the studied sample. Thus, any change of the flux detected by the coils produces a change in the persistent current flowing within the detection circuit. This change produces a variation of the SQUID output voltage that is proportional to the magnetic moment of the sample.

In this thesis, magnetic measurements have been carried out with a commercial MPSM3 SQUID-VSM EverCool system from Quantum Design. The experiments have been carried out by measuring the magnetic moment of the sample and scaling it to the mass of the sample to obtain the magnetization. We studied the ZFC/FC curves of the as-prepared nanoparticles to identify the characteristic Verwey transition[4] of the magnetite structure associated with changes in its

magnetic, electrical, and thermal properties. Further details of the characterized samples are provided in the corresponding chapter.

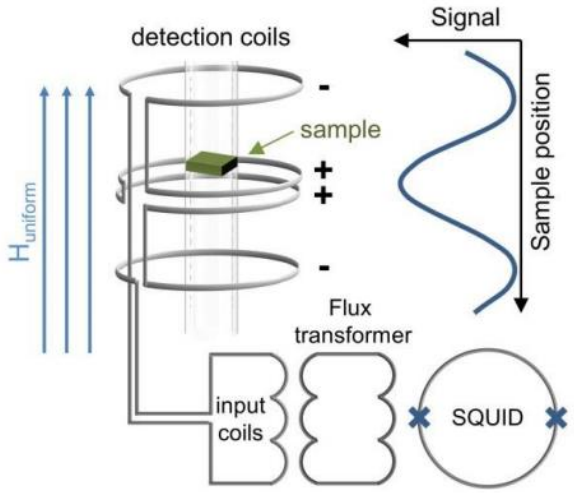

Figure 10. Schematic of the SQUID magnetometer detection system.

2.3. Electron Microscopy

The resolution of spectroscopic and microscopic techniques is limited by diffraction. However, changing the illumination source to smaller wavelengths is a commonly used strategy to overcome this limitation. Electron microscopy techniques are based on a beam of accelerated electrons that substitute light as illumination source. The wavelength of an electron beam is dependent on its acceleration, meaning that the higher the acceleration of electrons is, the shorter is the wavelength and therefore, the higher the resolution of the resulting image. Electron microscopy can span magnifications ranging from thousands to millions with resolutions ranging from nanometers to Ångstroms and even to the atomic scale. Thus, this technique is very useful for imaging nanomaterials with different sizes and geometries.

Figure 11 schematically shows the main interactions between the accelerated electron beam and the studied sample. Depending on how electrons are collected

by the detector, electron microscopy can be referred to as scanning electron microscopy (SEM) or transmission electron microscopy (TEM).

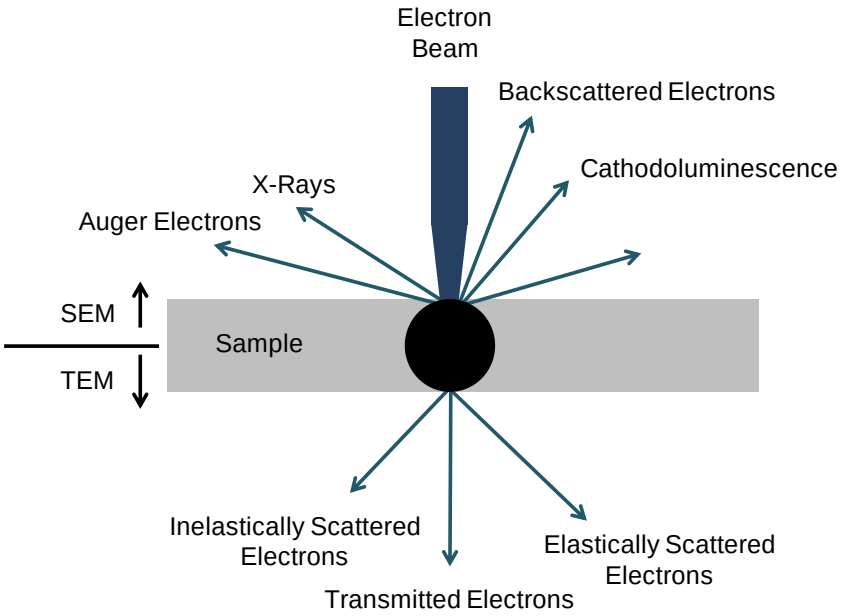

Figure 11. Illustration of the main types of interactions between an accelerated electron beam and a sample in an electron microscope.

2.3.1. Scanning Electron Microscopy (SEM)

Scanning electron microscopy (SEM) is very useful, especially in nanoscience, for analyzing micro and nanostructures of materials, including their shape, topography and morphology. In SEM, an electron beam scans across the sample surface and interacts with the sample. Secondary electrons or backscattered electrons, emitted from the sample surface, are collected by the detector. Those electrons result from the excitation of the sample by the electron beam. The amount of emitted secondary electrons depends on the topography of the surface of the sample, while the intensity of the backscattered electrons depends on the atomic number Z. Therefore, the detection of those electrons enables topological or compositional imaging of the sample. Moreover, as it is shown in Figure 11,

further modes are available in SEM imaging, which involve detection of characteristic X-rays, auger electrons, cathodoluminescence or charge of the sample.

For the SEM experiments performed in this thesis, an ULTRA plus ZEISS field emission scanning electron microscope (FESEM), equipped with an Ammeter EDAX (Apollo model) accessory for the elemental analysis of the samples by energy dispersive spectroscopy (EDS), was used. The specific process conditions are explained in each corresponding chapter.

2.3.2. Transmission Electron Microscopy (TEM)

In transmission electron microscopy (TEM), the electron beam passes through the sample and the transmitted electrons are detected in order to generate an image of the studied sample. Only thin samples or powders can be analyzed with this technique, since the electrons have to pass through the sample. The transmission of the electron beam depends on the interaction of the beam with the sample and thus on the atomic number Z. The achievable resolution in TEM images is usually an order of magnitude higher than in SEM images. In a well-adjusted TEM, even crystalline lattices of materials and single atoms can be observed.

2.3.3. Energy-Dispersive X-ray Spectroscopy (EDS)

Energy-dispersive X-ray spectroscopy (EDS) is an analytical technique used for the elemental analysis of a specific sample. In this case, a high-energy beam of charged particles, electrons or protons, excites an electron from an inner shell of an irradiated atom, expelling it from the shell and leaving an electron hole behind. This hole will be filled with an electron from an outer shell, and the difference in energy between the outer and the inner shell will be released as X-ray radiation. The energy emitted by the X-rays is specific of the emitting atom and is measured by an energy-dispersive spectrometer. In this way, EDS gives a precise analysis of the elemental composition of the sample. Usually, EDS measurements are carried out in parallel to TEM or SEM imaging, thus,

resulting in a complete analysis of elemental composition and structural information of the sample.

For all the TEM-EDS experiments performed in this thesis, a FEI Titan microscope, operating at 300 kV in scanning mode with a coupled energy-dispersive X-ray spectrometer (STEM-EDS) and equipped with a Quantum GIF 965 electron energy loss spectrometer (EELS), was used. All the measured powder samples were prepared by ultrasound dispersion in ethanol and drop casting on holey carbon TEM grids. Further details of the analyzed samples are provided in the corresponding chapter.

2.4. Inductively Coupled Plasma Mass Spectrometry (ICP-MS)

Inductively coupled plasma mass spectrometry (ICP-MS) is a very sensitive technique for the analysis of the inorganic composition of materials. For an analysis, inductively coupled plasma is used to atomize the sample and create atomic and small polyatomic ions, which are then detected in the mass spectrometer. This technique is applied for detecting very low concentrations of metals and non-metals in liquids with extreme precision. Moreover, it can detect different isotopes of the same element. The rapidity, accuracy and sensitivity of this technique make it highly valuable in micro and nanoscience.

In a typical ICP-MS analysis, samples are provided in liquid form. If samples are solid, they have to be pretreated in a process known as sample digestion, where they are dissolved and then diluted with dionized water and an acid, for example, nitric acid. For the measurement, the introduced liquid sample is transformed to a gas or aerosol by evaporation or nebulization. Liquid droplets are formed and become nebulized in the presence of a perpendicular argon gas flow. Later, in the torch where the plasma is generated, the argon gas with the nebulized sample is atomized. The formed atoms absorb energy from the plasma until they release electrons and become ionized. The newly formed ions pass to the mass analyzer. In order to analyze and determine the composition of the sample a mass spectrometer is coupled to the plasma system. The ions from the

plasma are extracted into the mass spectrometer with a series of cones. Here, the ions are separated based on the mass of their mass-to-charge ratio. A detector receives a signal proportional to the concentration, and afterwards, the concentration of the sample is determined through calibration with a certified reference material, such as a single or multi-element reference standard.

There are many applications of ICP-MS, such as, metal speciation (determination of oxidation state) or quantification of proteins and biomolecules, but usually this technique is used for elemental analysis. ICP-MS has the capability to scan all the elements of a sample simultaneously, allowing a rapid sample processing. It allows the determination of elements with atomic mass ranges from 7 to 250 (from lithium to uranium), and with sophisticated instrumentation and methods, sometimes even higher.

In this thesis, the elemental analysis of the studied powder samples was done with an iCAP-Q, Thermo Fisher Scientific GmbH equipment, Germany. Further details of the sample preparation and processing are given in the corresponding chapter.

2.5. Thermogravimetric analysis (TGA)

Thermogravimetric analysis (TGA) is an analytical technique, where a thermobalance is used to determine materials' thermal stability and its fraction of volatile components by monitoring the weight change that occurs when the sample is heated at a constant rate until temperatures of 1000 °C. This measurement provides information about physical phenomena (phase transitions, absorption, adsorption and desorption) and chemical phenomena (chemisorptions, thermal decompositions and solid-gas reactions) of a specific sample.[5]

In a TGA process, the sample is placed in a container with a precision balance inside a furnace with programmable temperature control. During the process a thermogravimetric analyzer continuously measures the sample mass, while the temperature of the sample is changed over time and the thermal reaction is

taking place. In order to carry out the reaction, a gas passes through the chamber (furnace). The nature of this gas depends on the kind of reaction that is expected to occur and can be air, inert gas, oxidizing or reducing gases, among others.

The collected thermogravimetric data from the thermal reaction are compiled and a quantitative analysis is done by measuring the loss or gain in mass. The TGA curve typically shows horizontal and curved sections, indicating a change in mass upon heating or cooling of the sample. The obtained data is used for determining purity and composition of materials, sublimation, drying or ignition temperatures of materials and for evaluating the stability of the compounds as a function of the temperature.

In this thesis, TGA measurements were done with a Netsch STA, Germany, for identifying the fraction of sulfur in the cathodic materials of lithium-sulfur batteries. The specific variables for each case are detailed in the corresponding chapter.

2.6. Dynamic Light Scattering (DLS)

Dynamic light scattering (DLS) is an analytical technique for measuring the average size and size distribution of particles dispersed in a suspension and/or emulsion. Usually, micro- or nanoparticles and macromolecules are measured. The technique is based on the Brownian motion of the dispersed particles.[6] Since particles are constantly colliding with solvent molecules, those collisions cause energy transfer, which affects the particle mobility. Since the energy transfer is rather constant, it is possible to determine the speed of the particles. By means of Stokes-Einstein equation,[7] the speed of the particles and the particle size are correlated, therefore the average size of the particles can be determined based on the correlation function, which is determined from the acquisition of so-called speckle patterns.

Figure 12 explains the DLS technique. A single frequency laser is directed to a sample contained in a cuvette. The incident laser light is attenuated using some

lens positioned between the sample and laser (generator and detector). When the incident laser light reaches the sample where particles are, it is scattered in all directions.

The scattered light is detected at a certain angle over time and this signal is used to determine the diffusion coefficient (speed of particles) and the particle size with the Stokes-Einstein equation.

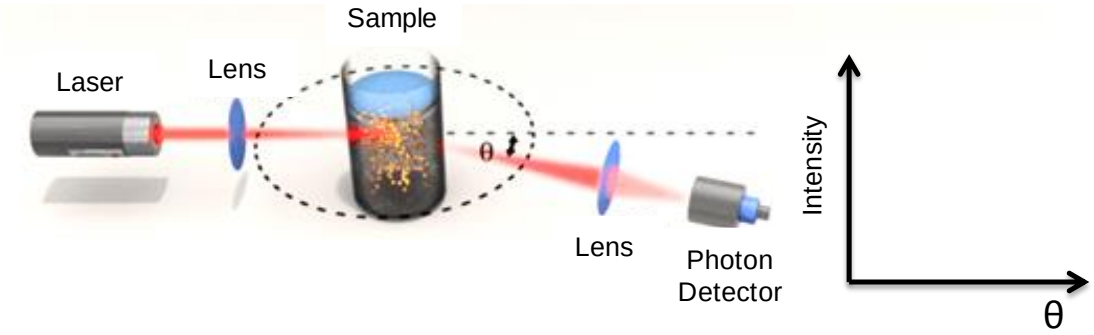

Figure 12. Schematic illustration of the procedure in the dynamic light scattering technique. Figure adapted from *https://lsinstruments.ch/en/technology/static-light-scattering-sls* taken on 13/12/2019.

Movements of the particles cause fluctuations in the generated pattern. The dynamic information of the particles is derived from an autocorrelation of the intensity trace recorded during experiments. From the intensity trace, a second order correlation function is obtained given by Equation 2.

$$g^2(\tau) = \frac{\langle I(t) I(t+\tau) \rangle}{\langle I(t) \rangle^2} \tag{2}$$

where *I(t)* is the intensity of the scattered light at a time *t*, and the brackets indicate averaging over all *t*. The correlation function depends on the delay τ, the amount that a duplicate intensity trace is shifted from the original before the averaging is performed. Once the autocorrelation data is obtained, using

some mathematical approaches and taking advantage of Stoke Einstein equation, the average particle size and the size distribution can be obtained.

In this thesis, the average particle size of the ALD-coated powders has been measured using a Nanosizer DLS equipment from Malvern. The powder samples were dispersed in a solvent before characterization. A more detailed description is given in the corresponding chapter.

2.7. Electrochemistry

Electrochemistry studies rely on the conversion of electrical energy to chemical energy and vice versa. The electrochemical characterization of batteries specifically investigates the chemical reactions that take place at the electrode interfaces, which often involves electrical discharge and charge transfer between the electrodes and the electrolyte of the cells. Measurements for evaluating the electrochemical performance on lithium-sulfur batteries can be carried out by cyclic voltammetry (CV),[8] galvanostatic charge-discharge testing[9] and electrochemical impedance spectroscopy (EIS).[10], [11] In this thesis, galvanostatic measurements were performed.

Galvanostatic cycling is used in order to determine the practical capacity of an electrode material. During those processes, electrons flow from one electrode to another and the electrodes are charged and discharged in each step. The term "specific capacity" is used in order to study the electrochemical behavior of a battery. The specific capacity, C, is the amount of charge that can be stored per unit of mass of a material in the electrode. It is often expressed in terms of $mAh \cdot g^{-1}$ and calculated as shown in Equation 3:

$$C_{electrode} = \frac{nF}{M} \times \frac{1000}{3600} \tag{3}$$

where n is the number of electrons transferred in the reaction, F is the Faraday's constant ($96{,}485\ C \cdot mol^{-1}$) and M is the molar mass of the electrode material ($g \cdot mol^{-1}$). Given the specific capacities of the cathode and anode, the specific capacity of the battery can be calculated as follows (Equation 4):

$$\frac{1}{C_{battery}} = \frac{1}{C_{cathode}} + \frac{1}{C_{anode}} \quad (4)$$

A related parameter is the specific energy density of a battery ($W_{battery}$), which is the amount of energy that can be stored per unit of mass or volume. It can be calculated, as a function of the calculated specific capacity and the average voltage applied to the battery.

Moreover, there is an additional indicator that links the discharge and charge parameters of a rechargeable battery, known as Coulombic Efficiency (CE). This parameter is calculated as shown in Equation 5:

$$CE\ (\%) = \frac{Discharge\ capacity}{Charge\ capacity} x\ 100 \quad (5)$$

In lithium-sulfur batteries, a value of 100% of CE indicates a completely reversible reaction, in which the amount of dissolved sulfur ions and the ones regenerated to S_8 is the same. However, experimentally, CE is less than 100%, meaning that undesirable side reactions, due to the generation of polysulfides and reactions with electrolyte, are taking place.

Usually, the galvanostatic discharge-charge measurements for studying the performance of batteries are done by the analysis of the C-rates and the cycle-life of the battery.

C-rate experiments

When the behavior of a battery is described, the discharge current is often expressed as a C-rate in order to normalize it against the battery capacity. The term C-rate describes how fast a battery is charged or discharged. A battery is usually cycled at various discharge (or charge) rates, also known as C-rates. C/n is defined as the current needed to complete the discharge or charge of the battery in n hours, based on the theoretical capacity of the electrode material. For instance, C/5, C/2, 1C and 2C correspond to complete discharge or charge cycles of the battery in 5h, 2h, 1h and 0,5h, respectively. For low-power applications, such as in experimental cells, usually low C-rates are employed, like

C/5 or C/10. However, in high-power applications, often high current densities are used, for example 2C, 5C or even higher. Those high C-rates can drastically affect the performance and the lifetime of a battery. Consequently, ways to improve their use are being intensely investigated.

Cycling or cycle-life analysis

Another typical experiment for testing the batteries' long-term stability is cycling. Here, batteries are charged and discharged multiple times and their capacity is measured, maintaining the current density constant, until their failure. The operating life of the battery is affected by the applied C-rate and by other conditions, such as, the temperature. Cycle life is an important parameter for evaluating the battery performance. The capacity retention with respect to the first cycle is reported as x% over a specific number of cycles, and the decay rate per cycle can be calculated as (100-x)/number of cycles.

In this thesis, electrochemical measurements have been carried out by means of galvanostatic testing, in order to study the cell performance of the modified lithium-sulfur batteries. Coin cells were assembled with the modified ALD sulfur cathodes and then tested with a BaSyTec Cell Test System (Germany). The specific experimental conditions are described more in detail in the corresponding experimental sections of each chapter.

References

[1] Myers, H. P. *Introductory Solid State Physics. Taylor & Francis* (2002).

[2] Oitmaa, J., Zheng, W. Curie and Néel temperatures of quantum magnets. *J. Phys. Condens. Matter* **16**, 8653–8660 (2004).

[3] Josephson, B. D. Possible new effects in superconductive tunnelling. *Phys. Lett.* **1**, 251–253 (1962).

[4] Bohra, M., Agarwal, N., Singh, V. A short review on Verwey Transition in nanostructured Fe_3O_4 materials. *J. Nanomater.* 1–18 (2019).

[5] Coats, A. W., Redfern, J. P. Thermogravimetric Analysis. *Analyst* **88**, 906–924 (1963).

[6] Mo, J., Raizen, M. G. Highly Resolved Brownian Motion in Space and in Time. *Annu. Rev. Fluid Mech.* **51**, 403–428 (2019).

[7] Kholodenko, A. L., Douglas, J. F. Generalized Stokes-Einstein equation for spherical particle suspensions. *Phys. Rev. E* **51**, 1081–1090 (1995).

[8] P.S., J., Sutrave, D. S. A Brief Study of Cyclic Voltammetry and Electrochemical Analysis. *Int. J. ChemTech Res.* **11**, 77–88 (2018).

[9] Talaie, E., Bonnick, P., Sun, X., Pang, Q., Liang, X., Nazar, L. F. Methods and protocols for electrochemical energy storage materials research. *Chem. Mater.* **29**, 90–105 (2017).

[10] Quanchao, Z., Shoudong, X., Xiangyun, Q., Yongli, C., Liang, F., Shigang, S. Diagnosis of electrochemical impedance spectroscopy in lithium ion batteries. *Prog. Chem.* **22**, 1044–1057 (2010).

[11] Lämmel, C., Schneider, M., Weiser, M., Michaelis, A. Investigations of electrochemical double layer capacitor (EDLC) materials - A comparison of test methods. *Materwiss. Werksttech.* **44**, 641–649 (2013).

Chapter 3

A Concerted Coating and Reduction Atomic Layer Deposition Process on TiO_2-coated Magnetite Nanoparticles

This chapter describes the initial experiments of the thesis in the area of ALD-coated particles. Iron oxide nanopowders have been coated by ALD in a chamber-type ALD reactor where particles were static and not fluidized. The work shows that the choice of a metal precursor with an appropriate ligand can unveil a novel approach to concertedly coat and reduce γ-Fe_2O_3 nanoparticles to form a final product composed of Fe_3O_4-TiO_2 core-shell nanoparticles. To this aim, an appropriate design of precursors and selection of substrates will pave the way for numerous new compositions, while the ALD process itself allows for easy up-scaling to large amounts of coated and reduced particles for industrial use.

This chapter describes the part of the thesis that was published in the journal *Chemical Science* from the Royal Society of Chemistry. The experimental work described in this chapter was performed at nanoGUNE, while the supporting modeling in form of density functional theory (DFT) calculations was performed by collaborators from the University of Texas in Dallas (USA). Graphs, figures and parts of the text of the publication are reused in this thesis with permission of the publisher.

Article:

Ligand-induced reduction concerted with coating by atomic layer deposition on the example of TiO_2-coated magnetite nanoparticles

Sarai García-García, Alberto López-Ortega, Yongping Zheng, Yifan Nie, Kyeongjae Cho, Andrey Chuvilin and Mato Knez. *Chemical Science*, **10**, 2171-2178 (2019).

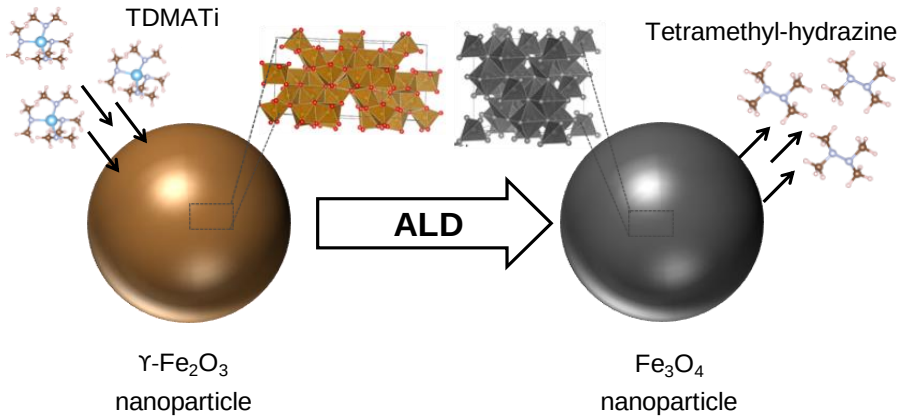

3.1. Introduction

Atomic layer deposition (ALD)[1]–[3] is a coating technology that in recent years became indispensable in microelectronics,[4],[5] and it enjoys a rapidly growing interest for emerging applications in energy storage[6]–[9] and medicine[10]–[12] among others. One of the important aspects of ALD is that it is a chemical deposition technology and as such requires understanding and control of the chemical processes that occur during the coating.[13]–[15] Most considerations for the development of a process are directed to the precursor chemistry, which is usually thoughtfully designed to enable a rapid process with ideally no impurities in the growing film and no corrosion or any other kind of harm to the coated substrate. Typically, metalorganic, organometallic or halide compounds are utilized as metal source for coatings and the ligands of those compounds shall ideally be highly volatile.[16]–[19] However, in numerous cases those ligands corrode the substrate or compete for adsorption sites,[20],[21] which are side reactions of such processes. Typically, such side reactions are unwanted, and precursors are chosen which will not release reactive ligands or intermediates. The ability to control such side reactions might, however, be of great interest, since one could achieve synchronous coating and alteration of a substrate in one process, thus saving time and energy otherwise needed for post treatment of the sample. One such scenario refers to the oxidation state of a substrate material. Since most ALD processes operate with a counter precursor that contains oxygen, for example, water vapor, oxygen plasma or ozone, it becomes difficult to preserve or achieve a reduced state of a metal during the process, particularly in those cases where the metal is prone to easily oxidizing. The choice of a precursor which contains ligands that upon release can reduce the substrate can be beneficial as it would avoid the need of post-processing, for example in the form of reductive annealing.

In this work, the synthesis of Fe_3O_4-TiO_2 core-shell nanoparticles by ALD at moderate temperatures is carried out. An ALD process is applied, which involves two independent and concerted chemical reactions. As substrate, commercial iron oxide nanoparticles are used and as precursors, Ti-based precursors with different ligands and deionized water. The possibility of coating and reducing at the same

time iron oxide particles depending on the existing ligand in the selected metal-based precursor is demonstrated. In other words, while the ALD process to coat the particles with TiO_2 takes place, the Fe^{3+} ions in the seed nanoparticles can be partially reduced to Fe^{2+}, enforcing the transformation of the γ-Fe_2O_3 to the well-known magnetite, Fe_3O_4, structure. The resulting core-shell particles have been systematically studied by X-ray diffraction, magnetometry, energy dispersive X-ray analysis and electron microscopy. The underlying mechanism for the reduction reaction was further modeled by density functional theory. Upon comparisons with various optional Ti-precursors, the study showed that the ligands of the titanium precursor tetrakis (dimethylamino) titanium (IV) (TDMATi) are responsible for the partial reduction of Fe^{3+} by forming tetramethylhydrazine as byproduct during the corresponding oxidation reaction. Both, simulation and experiments show that only this class of precursor enables the synchronous coating-reduction reaction, while the energy barriers for a reduction are too high in case of alternative choices of precursors. Those will only yield a coating of the particles.

This finding opens the possibility to design novel ALD precursors for a combined one-step capping and reduction process for the synthesis of further material combinations, while the ALD process itself allows for easy up-scaling to large amounts of coated and reduced particles for an industrial use.[22]–[26]

3.2. Experimental section

3.2.1. Sample preparation

All the samples were prepared following the same procedure. Commercial maghemite (γ-Fe_2O_3) nanoparticles with a particle size less than 50 nm, (CAS: 1309-37-1) from Sigma Aldrich, were dispersed in ethanol and sonicated for 15 minutes for better dispersion. Thereafter, the nanoparticles were spread over fused quartz substrates and dried for 24 hours. Prior to loading, the fused quartz substrates were cleaned in an ultrasonicator using acetone and ethanol and blown dry using nitrogen gas.[27]

3.2.2. ALD process

The coating of the nanoparticles was performed in a commercial pump-type ALD reactor (Savannah S100, Cambridge NanoTech Inc), where particles were coated being static inside the reactor chamber. The processes were carried out under a constant nitrogen gas flow of 20 standard cubic centimeters per minute (sccm) and under vacuum at a base pressure of 1 mbar.

Various metal-containing ALD precursors were used for the coating of the nanoparticles, including tetrakis (dimethylamino) titanium (IV) (TDMATi, $[(CH_3)_2N]_4Ti$), titanium chloride ($TiCl_4$), tetrakis (dimethylamino) tin (IV) (TDMASn, $[(CH_3)_2N]_4Sn$) and tetrakis (dimethylamino) hafnium (IV) (TDMAHf, $[(CH_3)_2N]_4Hf$), all of which were obtained from Sigma Aldrich. Demineralized water was used as oxygen source. The coated nanoparticles were prepared following a typical ALD timing sequence expressed as t_1-t_2-t_3-t_4, where t_1 is the exposure time to the first precursor, t_2 is the purge time following the first exposure, t_3 is the exposure time to the second precursor, t_4 is the purge time following the exposure to the second precursor. The times corresponding to t_1-t_2-t_3-t_4 were 20-25-20-25, all given in seconds (s). The pulsing times were a function of the vapor pressure of the precursor. For TDMA-based precursors (titanium, tin and hafnium) 0,5 s at 150 °C process temperature were used and 0,2 s was the pulsing time only for the comparative case, at 250 °C process temperature. For the chloride precursor 0,05 s were used, and for demineralized water in all the cases 0,05 s was the pulsing time. The process temperature in all cases was 150 °C. One further process was carried out at 250 °C with TDMASn in order to evaluate the thermal impact of the ALD process on the substrate. For all coatings, a thickness of approximately 30 nm was targeted. In order to obtain this thickness, 440 ALD cycles were performed for TiO_2 deposition with TDMATi, calculated from the obtained growth rate of 0,73 Å · $cycle^{-1}$. For the $TiCl_4$ process, 500 ALD cycles were applied, resulting from the growth rate of 0,66 Å · $cycle^{-1}$. For the SnO_2 and HfO_2 processes, 380 ALD cycles (growth rate: 0,79 Å · $cycle^{-1}$) and 400 ALD cycles (growth rate: 0,82 Å · $cycle^{-1}$) were applied, respectively.

After the ALD coating process, TiO_2-coated Fe_2O_3 nanoparticles with TDMATi and demineralized water, were subjected to *ex situ* annealing in order to crystallize the deposited film. The thermal treatment was carried out in air at atmospheric pressure and at 470 ^oC for 3 hours.[28]

3.2.3. Structural characterization

Scanning transmission electron microscopy (STEM) images were acquired with a FEI Titan operating at 300 kV in scanning mode with a coupled energy-dispersive x-ray spectrometer (STEM-EDX). The samples were dissolved in ethanol and drop casted onto carbon coated copper grids.

Powder x-ray diffraction (XRD) patterns were recorded with a PANalytical XPert Pro x-ray diffractometer using Cu Kα radiation (λ=1,5405980 Å) operating at 45 kV/40 mA in the 25^o – 65^o 2θ range with a scan speed of $0{,}00144^o \cdot s^{-1}$. Quantitative analysis of the XRD data was performed with a full pattern fitting procedure based on the fundamental parameter approach (Rietveld method) using the MAUD software (http://maud.radiographema.eu/).

The magnetic properties of the nanoparticles were measured from tightly packed powder samples using a vibrating sample mode magnetometer (Quantum Design SQUID-VSM overcool) with 70 kOe maximum field. Magnetization versus temperature measurements were performed in zero-field cooled (ZFC) and field cooled (FC) conditions with 50 Oe probe fields.

3.2.4. Computational methods

All the calculations in this work were performed using the density functional theory (DFT) method implemented in the Vienna *ab initio* simulation package (VASP)[29], [30] with the projector-augmented wave (PAW) method.[31] The generalized gradient approximation (GGA) with semilocal Perdew-Burke-Ernzerhof (PBE)[32] function was adopted to describe the exchange correlation interactions. The cutoff energy was set to be 450 eV. The structures were optimized with criteria of convergence for energy and force as 10^{-4} eV and 10^{-2}

$eV \cdot Å^{-1}$, respectively. On-site Coulomb repulsion of Fe $3d$ electrons was corrected by GGA+U method[33] with U_{eff}=4 eV according to previous theoretical reports.[34], [35]

The minimum activation barriers of reducing Fe_2O_3 to Fe_3O_4 by different ALD precursors were determined as the reaction energy of the Reaction 9:

$$6Fe_2O_3 + M\text{-}L_4(ad) \rightarrow 4Fe_3O_4 + MO_2 + 2L_2(ad) \quad (9)$$

, where M-$L_4(ad)$ and $L_2(ad)$ denote the adsorbed ALD precursors and adsorbed oxidation products, respectively. Although the reaction energies are typically positive, this reduction reaction will be driven by the entropy change as L_2 desorbs and becomes gas phase.

3.3. Results and discussion

Commercial γ-Fe_2O_3 nanoparticles (sample FeO_x) have been coated with TiO_2 by ALD using at a first stage, TDMATi and water as precursors (sample TDMATi-FeO_x). Figure 13(a) shows x-ray diffraction (XRD) patterns obtained from the samples before and after ALD coating. Both diffraction patterns are very similar showing characteristic peaks of the cubic spinel structure stemming from the iron oxide. It should be noted that no characteristic peaks from titanium oxide are seen, which is due to the amorphous character of the TiO_2 deposited in the applied processing conditions.

However, the transmission electron micrographs show the formation of a core-shell structure. In Figure 14 the core-shell construction of the nanoparticles is very obvious both from the contrast in scanning transmission electron microscopy (STEM) as well as the energy-dispersive x-ray spectroscopy (EDX) images, which show the involved elements in different colors. A more detailed analysis of the x-ray diffraction (XRD) patterns of samples FeO_x and TDMATi-FeO_x shows a clear alteration of the pristine iron oxide structure after the ALD process. While both patterns reveal the presence of a cubic spinel structure, the shift in their diffraction peaks and the concomitant variation of their cell parameter, points towards the presence of two different iron oxide phases in the two samples.

The commercial particles have a cell parameter of 8,347(5) Å (see Table 1) which is characteristic for completely oxidized maghemite, γ-Fe_2O_3 (JCPDS Card No. 39-1346), where Fe^{3+} cations occupy the octahedral and tetrahedral sites of the structure. In contrast, sample TDMATi-FeO_x shows an increase of the cell parameter to values of 8,390(5) Å (see Table 1), which is characteristic for a partial $Fe^{3+} \rightarrow Fe^{2+}$ reduction of the octahedral cations to form the well-known magnetite, Fe_3O_4 structure (JCPDS Card No. 19-629). Note that the crystal size of both samples is very similar with values of roughly 30 nm. The expected change of the volume of about 6% after ALD process is not notable from Rietveld-based XRD measurements, since the resolution is not high enough for clearly confirming such small changes.

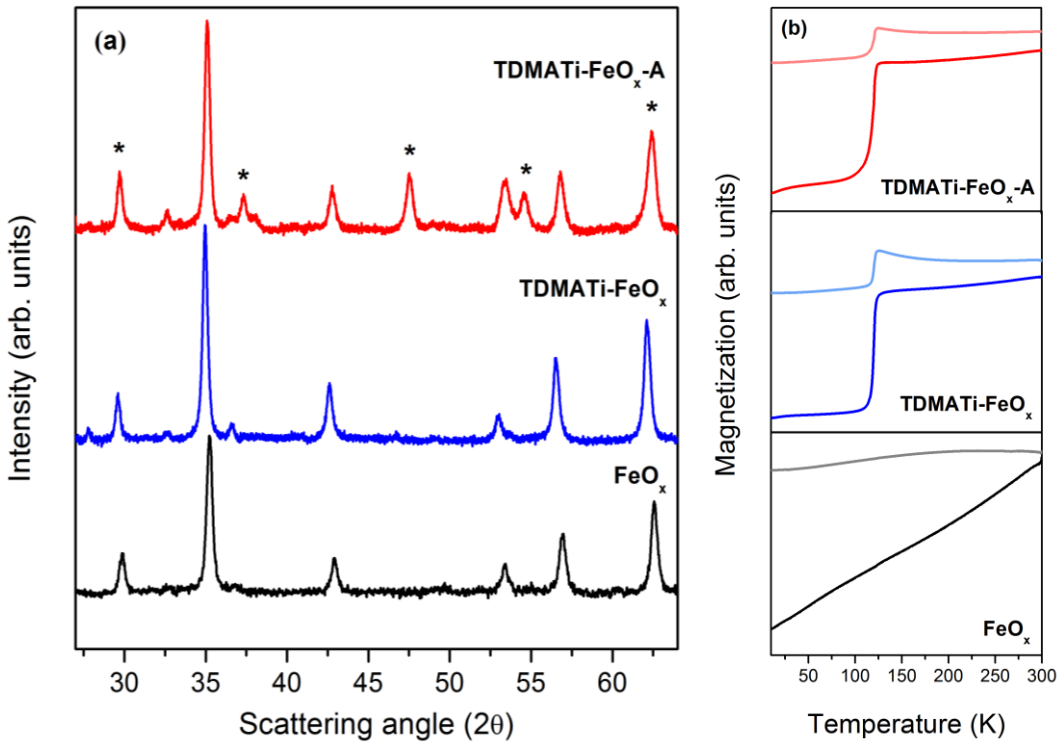

Figure 13. (a) XRD patterns of uncoated γ-Fe_2O_3 particles (FeO_x), TiO_2-coated γ-Fe_2O_3 nanoparticles with TDMATi and H_2O precursors, before annealing (TDMATi-FeO_x) and after annealing at 470 °C (TDMATi-FeO_x-A). (b) Magnetization curves vs. temperature for the samples in (a). * denotes diffraction peaks originating from TiO_2.

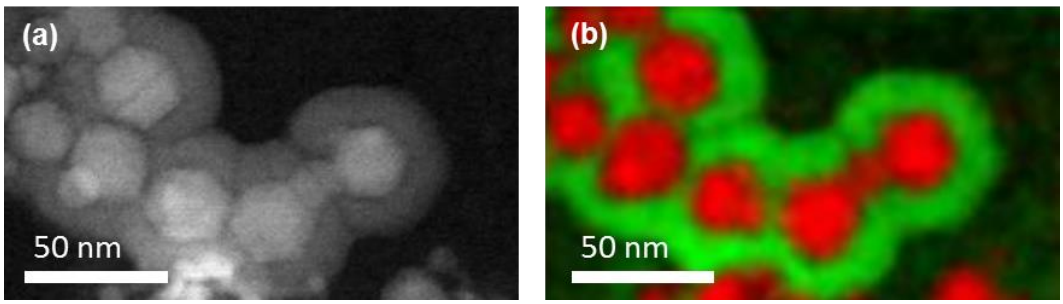

Figure 14. (a) STEM micrograph and (b) STEM-EDX map of Fe_3O_4 (red)-TiO_2 (green) core-shell nanoparticles.

In order to gain more insight into the phase transformation observed after the ALD process the magnetic properties of both samples are compared by measuring their magnetization temperature curves in both field cooling (FC) and zero field cooling (ZFC) conditions (see Figure 13(b), in bold ZFC). Both samples depict the expected behavior for nanostructured magnetic nanoparticles, where the FC and ZFC curves are distinct at low temperatures and tend to converge at the so-called blocking temperature (T_B).[36] Indeed, for such large iron oxide particles (i.e., 30 nm) this transition was observed at temperatures above RT.[37] Sample TDMATi-FeO_x shows a similar trend as the untreated sample, but with an extrapolated T_B at higher temperatures. More interesting is, however, another magnetic transition that can be clearly observed at 120 K and can be ascribed to the Verwey temperature (T_V) of Fe_3O_4. This transition is characteristic of Fe_3O_4 which undergoes a transformation from cubic ($T > T_V$) to monoclinic ($T < T_V$) symmetry.[38] Such transformation is related to modifications in the crystal symmetry and the cation ordering and is accompanied by dramatic changes in electrical conductivity and heat capacity. Given the results of the magnetic characterization, it can be stated that the iron in the commercial particles (FeO_x) suffered a transformation from a completely oxidized state as typical in maghemite (γ-Fe_2O_3) to a partially reduced state as it is typical of magnetite (Fe_3O_4) during the ALD process.

Table 1. Structural properties and Verwey transition of nanoparticles.

Sample	**Composition**	**ALD process**	**Phase**	**Lattice parameter (Å)**	**Crystal size (nm)**	**Verwey transition**
FeO_x	Commercial FeO_x	---	γ -Fe_2O_3	8,347(5)	32,5(5)	NO
TDMATi-FeO_x	TiO_2-FeO_x	TDMATi+H_2O (150 °C)	Fe_3O_4	8,390(5)	31(5)	YES
TDMATi-FeO_x-A	TiO_2-FeO_x	TDMATi+H_2O (150 °C)	Fe_3O_4	8,388(5)	32(5)	YES
		Annealing (470 °C)	TiO_2	3,782(5)/9,483(5)	23(5)	
$TiCl_4$-FeO_x	TiO_2-FeO_x	$TiCl_4$+H_2O (150 °C)	γ – Fe_2O_3	8,339(5)	28(5)	NO
TDMASn-FeO_x	SnO_2-FeO_x	TDMASn+H_2O (150 °C)	γ -Fe_2O_3	8,351(5)	23(5)	NO
TDMASn-FeO_x-250	SnO_2-FeO_x	TDMASn+H_2O (250 °C)	Fe_3O_4	8,380(5)	30(5)	YES
TDMAHf-FeO_x	HfO_2-FeO_x	TDMAHf+H_2O (150 °C)	Fe_3O_4	8,382(5)	44(5)	YES

For crystallographic confirmation of the deposition of titanium oxide over the iron oxide, the particles have been annealed at 470 °C (sample TDMATi-FeO_x-A). Figure 13(a) shows the evolution of anatase-type TiO_2 (JCPDS Card No. 21-1272) after annealing, which resulted from the crystallization of the deposited film. Moreover, the peaks of the cubic spinel structure of Fe_3O_4 are not affected by the heat treatment, preserving the structure obtained after the ALD process. The magnetization measurement of the particles after annealing further confirms the presence of magnetite showing its characteristic Verwey transition (see Figure 13(b)). It is interesting to note that no traces of any further iron oxide crystal structure can be found, and the crystal size of the phase is very similar to the untreated sample (i.e., 30 nm). Both effects demonstrate that the TiO_2 coating avoids intimate contact between the particles and thus their agglomeration and phase transformation to more stable iron oxide phases (i.e., α-Fe_2O_3), even if the temperature is increased to 470 °C.[39]

The TiO_2 coating of iron oxide particles by ALD using TDMATi as precursor not only protects the nanostructures from oxidation and agglomeration, but also induces a partial reduction of the pristine γ-Fe_2O_3 and a concomitant phase transformation. Such transformation may be triggered by either the metal or by the ligand present in the ALD precursor. Therefore, a series of experiments has been performed in order to identify the source. Firstly, the growth of TiO_2 has been carried out using an alternative titanium precursor (titanium chloride, $TiCl_4$) in order to identify a potential effect of the titanium ion. In the second stage, the effect of the $(CH_3)_2N^-$ ligand has been evaluated by performing ALD coatings with another TDMA-based metal precursor, tetrakis (dimethylamino) tin (IV) (TDMASn).

Sample $TiCl_4$-FeO_x has been obtained after an ALD process of the same commercial iron oxide particles using $TiCl_4$ and demineralized water as precursors at 150 °C. From the Rietveld analysis of the x-ray diffraction data in Figure 15, it can be observed that after the TiO_2 deposition the cell parameter of the iron oxide core remains similar to the pristine sample (γ-Fe_2O_3) (see Table 1). The magnetometric curves, Figure 16, show no signs of Verwey transition. Therefore, the titanium cation appears not to be responsible for the partial reduction of the

γ-Fe_2O_3 particles, which is reasonable from the chemical perspective as it is already present in the oxidation state +4 and further oxidation would not be possible in the given conditions.

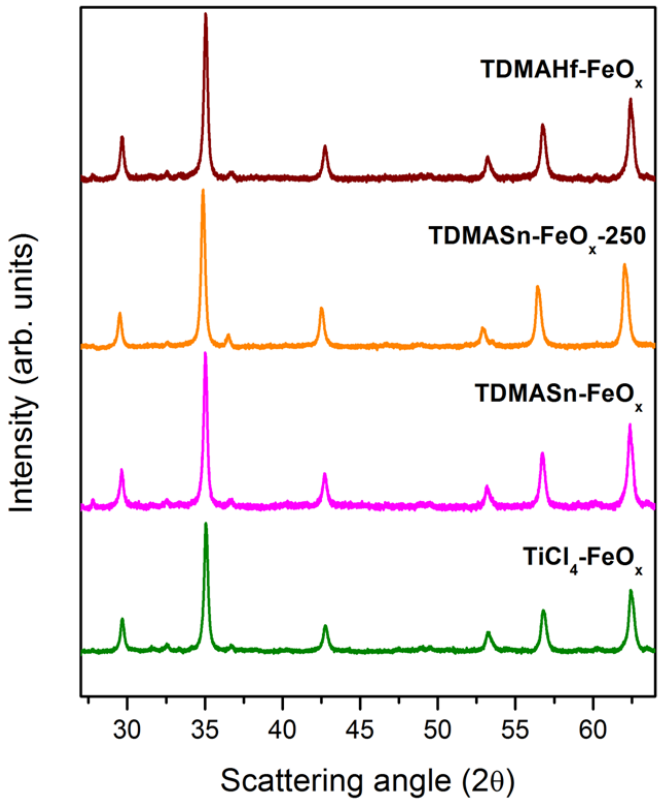

Figure 15. XRD patterns of TiO_2-coated γ-Fe_2O_3 nanoparticles with $TiCl_4$ and H_2O ALD precursors ($TiCl_4$-FeO_x), SnO_2-coated γ-Fe_2O_3 nanoparticles with TDMASn and H_2O ALD precursors, at processing temperatures of 150 °C (TDMASn-FeO_x) and 250 °C (TDMASn-FeO_x-250), and HfO_2-coated γ-Fe_2O_3 nanoparticles with TDMAHf and H_2O ALD precursors (TDMAHf-FeO_x).

For investigating the ligand ($(CH_3)_2N^-$) as potential reducing agent, TDMASn and demineralized water were used as precursors in an ALD process at 150 °C (sample TDMASn-FeO_x). Similar to the $TiCl_4$ ALD process, the crystal structure of the iron oxide particles after using TDMASn seem not to be affected. The particles largely maintain their cell parameters (Table 1) and no presence of Verwey

transition is observed, Figure 16. However, considering the different Pauling electronegativities of Ti and Sn (i.e., 1.3 and 1.8 for Ti and Sn, respectively), the reactivity of the ligand may be strongly affected by the metal cation present in the precursor. Assuming that the energy required for the ligand dissociation from the coordination sphere of the metal in the TDMASn is higher than in the case of the TDMATi, the ALD process with the tin precursor has been repeated at higher temperatures, namely, at 250 °C (sample TDMASn-FeO_x-250).

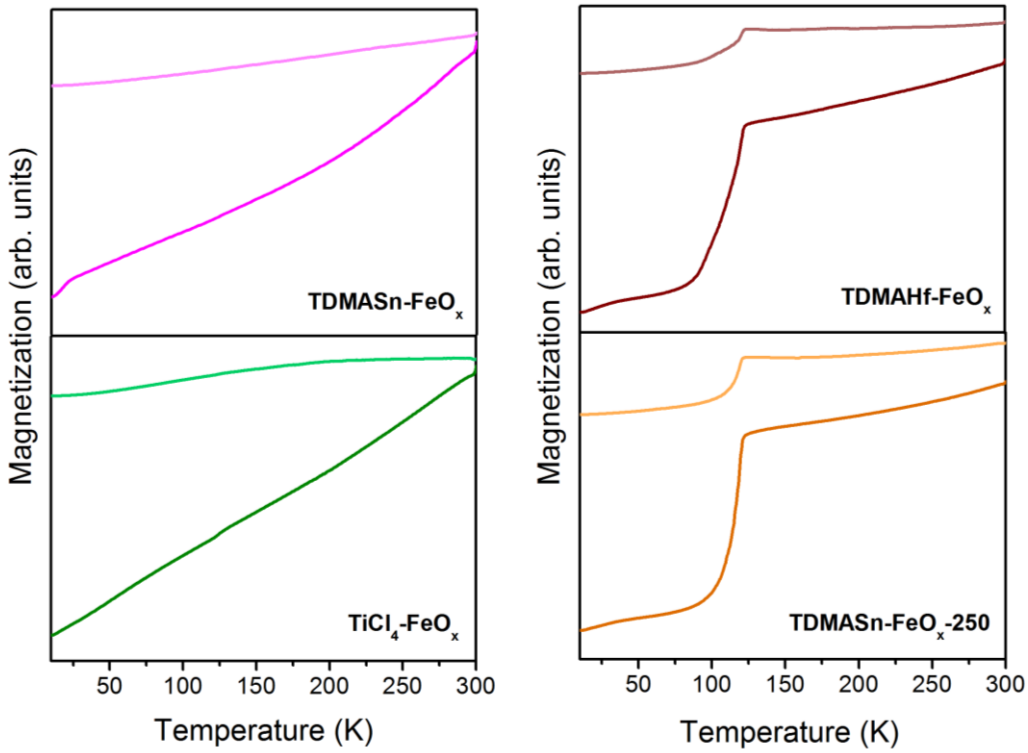

Figure 16. Magnetization vs. temperature curves of TiO_2-coated γ-Fe_2O_3 nanoparticles applying $TiCl_4$ and H_2O as ALD precursors ($TiCl_4$-FeO_x), SnO_2-coated γ-Fe_2O_3 nanoparticles with TDMASn and H_2O as ALD precursors, at 150 °C (TDMASn-FeO_x) and at 250 °C (TDMASn-FeO_x-250) process temperatures, and HfO_2-coated γ-Fe_2O_3 nanoparticles with TDMAHf and H_2O ALD precursors (TDMAHf-FeO_x).

As a result, the iron oxide nanostructure is affected in a similar manner as with TDMATi. The cell parameter is increased (Table 1) and the Verwey transition appears in the magnetization curves, Figure 16, confirming the $Fe^{3+} \rightarrow Fe^{2+}$ partial reduction and, thus, the Fe_3O_4 formation.

Finally, in order to further confirm that the TDMA ligand is responsible for the reduction, a further ALD process with tetrakis (dimethylamino) hafnium (IV) (TDMAHf) as precursor has been performed (sample TDMAHf-FeO_x). Hf has an electronegativity similar to Ti (i.e., 1.2), which implies that upon correct assumption of the mechanism, similar results as with TDMATi can be obtained. A partial reduction of the γ-Fe_2O_3 may take place already at lower temperatures. Indeed, the Rietveld analysis of the sample TDMAHf-FeO_x shows that the cell parameter is increased after the TDMAHf process to permit the formation of the Fe_3O_4 structure. In the magnetization curves, Figure 16, the Verwey temperature is clearly observed.

The results show that the anion of the precursor, $((CH_3)_2N^-)$, is responsible for the partial reduction of iron oxide and the concomitant structural modification of the initial seed nanoparticles. In the first step of the ALD process, the TDMATi precursor loses the amino groups while anchoring to the surface of the nanoparticles. Those ligands can lose one electron each and recombine to form gas phase tetramethylhydrazine ($(CH_3)_2NN(CH_3)_2$), which is the oxidation product as the γ-Fe_2O_3 substrate is being reduced.

A DFT modeling of the reaction activation energies was performed for such a case and it was compared to the model of reactions with different precursors varying the central metal ion and the ligands (Figure 17). Indeed, the calculations show that the TDMATi energetically favors the reduction of γ-Fe_2O_3 to Fe_3O_4 with an estimated activation barrier of 0,85 eV, and the TDMAHf has a reduction capability similar to TDMATi (a lower barrier of 0,73 eV). However, the TDMASn is energetically less favorable for such a reduction reaction with a larger activation barrier of 1,12 eV, indicating that a higher reaction temperature is needed to trigger the reduction, which is in full agreement with the experimental observations. For Ti precursors with different ligands such as $Ti(OiPr)_4$ (titanium

isopropoxide) or $TiCl_4$, DFT calculations show significantly higher values of 4,08 eV and 4,45 eV, respectively, meaning that no reduction is expected. These theoretical results well explain the phenomena observed experimentally and support the importance of precursor ligands for such concerted reduction-coating processes. When an ALD process is carried out, the electrons originating from the amino ligands of the TDMATi create a chemical potential gradient at the nanoparticle surface triggering the reduction process along the whole iron oxide structure.

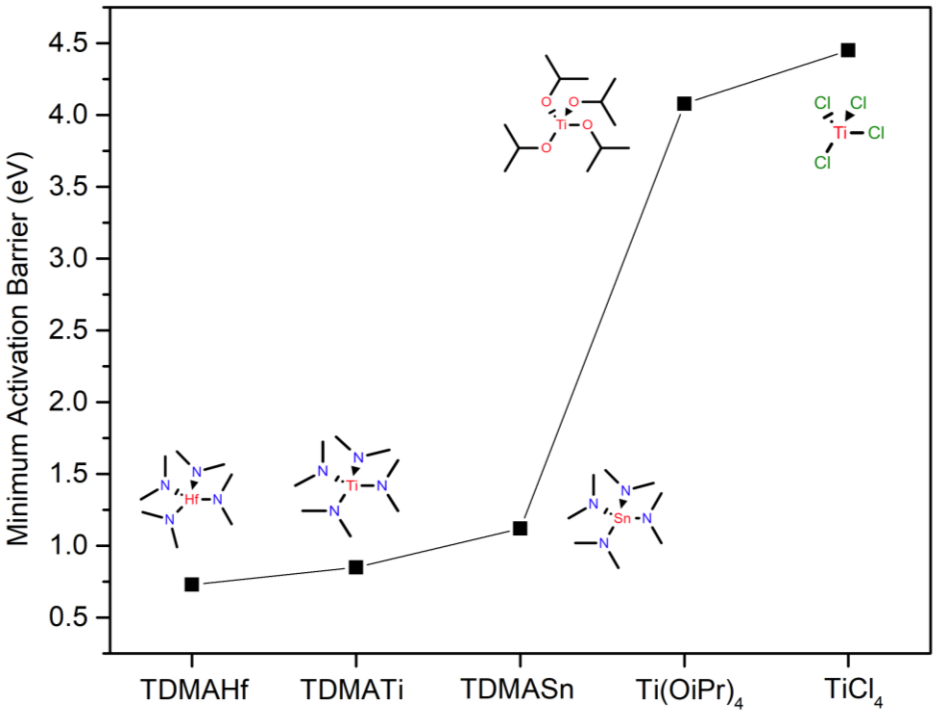

Figure 17. Comparison of DFT calculated minimum activation barriers for reducing Fe_2O_3 to Fe_3O_4 by using various ALD precursors as sketched in the graph.

This hypothesis is supported by the magnetometric curves measured after different ALD cycle numbers and the visual color change of the particles after ALD process (Figure 18). The characteristic T_V for the Fe_3O_4 structure appears

already after the first ALD cycles and becomes more pronounced as the number of cycles increases, which is very likely related to a mediated diffusion and growth mechanism.[40] Besides, it is possible to appreciate visually, the color change from orange, in commercial γ-Fe_2O_3, to black, after the reduction to Fe_3O_4.

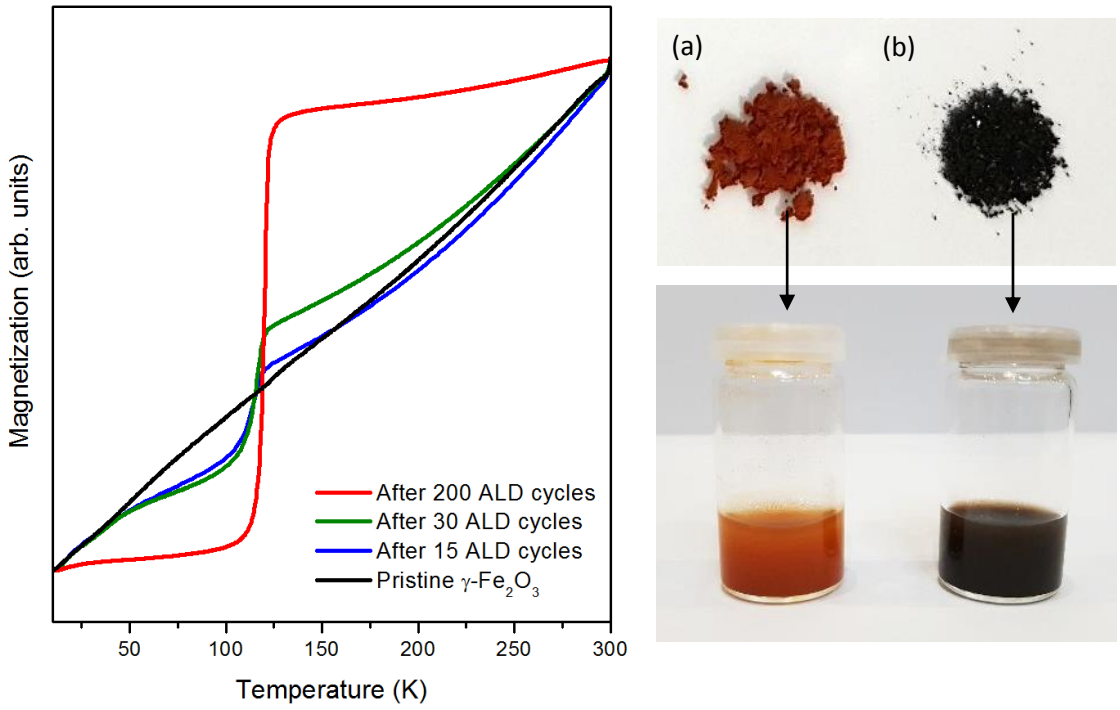

Figure 18. Left panel: Magnetization vs. temperature curves of Fe_3O_4-TiO_2 core-shell nanoparticles after various numbers of ALD coating cycles and a concerted reduction of the γ-Fe_2O_3 nanoparticles to Fe_3O_4. Right panel: Visual color change of the particles in powder form (top) and dispersed in water (bottom); (a) untreated commercial γ-Fe_2O_3 nanoparticles, (b) the same particles after applying various ALD cycles, forming Fe_3O_4-TiO_2 core-shell nanoparticles. The color change from orange to black is indicative of a transformation from γ-Fe_2O_3 to magnetite.

3.4. Conclusions

In this work, it is demonstrated that the ALD process not only coats nanoparticles in a controlled way, but also depending on the ligand of the metallic

precursor, the substrate material is modified on its final chemical and/or structural properties. γ-Fe_2O_3 nanoparticles have been coated with TiO_2 and concertedly reduced to magnetite. As a result, Fe_3O_4-TiO_2 core-shell nanoparticles have been generated by atomic layer deposition at moderate temperatures. The deposited coatings prevent agglomeration of the nanoparticles and re-oxidation to γ-Fe_2O_3 even at high temperatures, allowing for the use of post-process annealing and thus crystallization of the amorphous TiO_2 to anatase; a beneficial characteristic which has an important role in many industrial and bio-related applications.

The reduction of γ-Fe_2O_3 to Fe_3O_4 is a function of the applied precursor and the processing temperature. The ligand of the precursor $(CH_3)_2N^-$ can become oxidized and recombine to form tetramethylhydrazine, while acting as reducing agent for the Fe^{3+}. The cation of the precursor also plays an important role. The more electronegative the cation is, the more energy is necessary to release the ligands, which is important for the recombination. Therefore, the temperature required for ALD processes to reduce the sample is higher for TDMASn than for TDMATi and TDMAHf.

The use of an ALD process to concertedly coat and reduce nanomaterials simplifies numerous attempts to generate multifunctional materials for emerging applications, such as energy storage or medicine. The appropriate design of precursors and selection of substrates will pave the way for numerous new compositions, while the ALD process itself allows for easy up-scaling to large amounts of coated and reduced particles for an industrial use.

References

[1] Parsons, G. N., George, S. M., Knez, M. Progress and future directions for atomic layer deposition and ALD-based chemistry. *MRS Bull.* **36**, 865–871 (2011).

[2] George, S. M. Atomic layer deposition: an overview. *Chem. Rev.* **110**, 111–131 (2009).

[3] Knez, M. ALD a Versatile Tool for Nanostructuring. *Mater. Matters* **3**, 1–7 (2008).

[4] Johnson, R. W., Hultqvist, A., Bent, S. F. A brief review of atomic layer deposition: From fundamentals to applications. *Mater. Today* **17**, 236–246 (2014).

[5] Lee, F., Marcus, S., Shero, E., Wilk, G., Swerts, J., Maes, J. W., Blomberg, T., Delabie, A., Gros-Jean, M., Deloffre, E. Atomic layer deposition: An enabling technology for microelectronic device manufacturing. *ASMC (Advanced Semicond. Manuf. Conf.) Proc.* 359–365 (2007).

[6] Knoops, H. C. M., Donders, M. E., van de Sanden, M. C. M., Notten, P. H. L., Kessels, W. M. M. Atomic layer deposition for nanostructured Li-ion batteries. *J. Vac. Sci. Technol. A Vacuum, Surfaces, Film.* **30**, 010801 (2012).

[7] Jung, Y. S., Cavanagh, A. S., Riley, L. A., Kang, S. H., Dillon, A. C., Groner, M. D., George, S. M., Lee, S. H. Ultrathin direct atomic layer deposition on composite electrodes for highly durable and safe Li-Ion batteries. *Adv. Mater.* **22**, 2172–2176 (2010).

[8] Yan, B., Li, X., Bai, Z., Song, X., Xiong, D., Zhao, M., Li, D., Lu, S. A review of atomic layer deposition providing high performance lithium sulfur batteries. *J. Power Sources* **338**, 34–48 (2017).

[9] Niu, W., Li, X., Karuturi, S. K., Fam, D. W., Fan, H., Shrestha, S., Wong, L. H., Tok, A. I. Y. Applications of atomic layer deposition in solar cells.

Nanotechnology **26**, 064001 (2015).

[10] Skoog, S. A., Elam, J. W., Narayan, R. J. Atomic layer deposition: medical and biological applications. *Int. Mater. Rev.* **58**, 113–129 (2013).

[11] Narayan, R. J., Adiga, S. P., Pellin, M. J., Curtiss, L. A., Stafslien, S., Chisholm, B., Monteiro-Riviere, N. A., Brigmon, R. L., Elam, J. W. Atomic layer deposition of nanoporous biomaterials. *Mater. Today* **13**, 60–64 (2010).

[12] Knez, M., Kadri, A., Wege, C., Gösele, U., Jeske, H., Nielsch, K. Atomic layer deposition on biological macromolecules: metal oxide coating of tobacco mosaic virus and ferritin. *Nano Lett.* **6**, 1172–1177 (2006).

[13] Choi, W.-S. The Fabrication of Tin Oxide Films by Atomic Layer Deposition using Tetrakis(Ethylmethylamino) Tin Precursor. *Trans. Electr. Electron. Mater.* **10**, 200–202 (2009).

[14] Chaukulkar, R. P., Agarwal, S. Atomic layer deposition of titanium dioxide using titanium tetrachloride and titanium tetraisopropoxide as precursors. *J. Vac. Sci. Technol. A* **31**, 031509 (2013).

[15] Leem, J., Park, I., Li, Y., Zhou, W., Jin, Z., Shin, S., Min, Y. Role of HCl in Atomic Layer Deposition of TiO_2 Thin Films from Titanium Tetrachloride and Water. *Bull. Korean Chem. Soc.* **35**, 1195–1201 (2014).

[16] Puurunen, R. L. Surface chemistry of atomic layer deposition : a case study for the trimethylaluminum / water process. *J. Appl. Phys.* **97**, 121301-121301–52 (2005).

[17] Yum, J. H., Akyol, T., Ferrer, D. A., Lee, J. C., Banerjee, S. K., Lei, M., Downer, M., Hudnall, T. W., Bielawski, C. W., Bersuker, G. Comparison of the self-cleaning effects and electrical characteristics of BeO and Al_2O_3 deposited as an interface passivation layer on GaAs MOS devices. *J. Vac. Sci. Technol. A Vacuum, Surfaces, Film.* **29**, 061501 (2011).

[18] Hou, C. H., Chen, M. C., Chang, C. H., Wu, T. B., Chiang, C. D., Luo, J. J. Effects of Surface Treatments on Interfacial Self-Cleaning in Atomic

Layer Deposition of Al_2O_3 on InSb. *J. Electrochem. Soc.* **155**, G180–G183 (2008).

[19] Tallarida, M., Adelmann, C., Delabie, A., Van Elshocht, S., Caymax, M., Schmeisser, D. Surface chemistry and Fermi level movement during the self-cleaning of GaAs by trimethyl-aluminum. *Appl. Phys. Lett.* **99**, 10–13 (2011).

[20] Ande, C. K., Knoops, H. C. M., de Peuter, K., van Drunen, M., Elliott, S. D., Kessels, W. M. M. Role of Surface Termination in Atomic Layer Deposition of Silicon Nitride. *J. Phys. Chem. Lett.* **6**, 3610–3614 (2015).

[21] O'Neill, B. J., Jackson, D. H. K., Lee, J., Canlas, C., Stair, P. C., Marshall, C. L., Elam, J. W., Kuech, T. F., Dumesic, J. A., Huber, G. W. Catalyst Design with Atomic Layer Deposition. *ACS Catal.* **5**, 1804–1825 (2015).

[22] McCormick, J. A., Cloutier, B. L., Weimer, A. W., George, S. M. Rotary reactor for atomic layer deposition on large quantities of nanoparticles. *J. Vac. Sci. Technol. A Vacuum, Surfaces, Film.* **25**, 67–74 (2007).

[23] Kim, W. J., Jang, E., Park, T. J. Enhanced visible-light photocatalytic activity of ZnS/g-C_3N_4type-II heterojunction nanocomposites synthesized with atomic layer deposition. *Appl. Surf. Sci.* **419**, 159–164 (2017).

[24] Ferguson, J. D., Buechler, K. J., Weimer, A. W., George, S. M. SnO_2 atomic layer deposition on ZrO_2 and Al nanoparticles: Pathway to enhanced thermite materials. *Powder Technol.* **156**, 154–163 (2005).

[25] Jang, E., Sridharan, K., Park, Y. M., Park, T. J. Eliminated Phototoxicity of TiO_2 Particles by an Atomic-Layer-Deposited Al_2O_3 Coating Layer for UV-Protection Applications. *Chem. - A Eur. J.* **22**, 12022–12026 (2016).

[26] Sridharan, K., Jang, E., Park, Y. M., Park, T. J. Superior Photostability and Photocatalytic Activity of ZnO Nanoparticles Coated with Ultrathin TiO_2 Layers through Atomic Layer Deposition. *Chem. - A Eur. J.* **21**, 19136–19141 (2015).

[27] Martinson, A. B. F., DeVries, M. J., Libera, J. A., Christensen, S. T.,

Hupp, J. T., Pellin, M. J., Elam, J. W. Atomic Layer Deposition of Fe_2O_3 Using Ferrocene and Ozone. *J. Phys. Chem. C* **115**, 4333–4339 (2011).

[28] Lin, C.-P., Chen, H., Nakaruk, A., Koshy, P., Sorrell, C. C. Effect of Annealing Temperature on the Photocatalytic Activity of TiO_2 Thin Films. *Energy Procedia* **34**, 627–636 (2013).

[29] Kresse, G., Hafner, J. Ab initio molecular dynamics for liquid metals. *Phys. Rev. B* **47**, 558–561 (1993).

[30] Kresse, G., Furthmiiller, J. Efficiency of ab-initio Total Energy Calculations for Metals and Semiconductors Using a Plane-wave Basis Set. *Comput. Mater. Sci.* **6**, 15–50 (1996).

[31] Kresse, G., Joubert, D. From Ultrasoft Pseudopotentials to the Projector Augmented-Wave Method. *Phys. Rev. B* **59**, 1758–1775 (1999).

[32] Perdew, J. P., Burke, K., Ernzerhof, M. Generalized Gradient Approximation Made Simple. *Phys. Rev. Lett.* **77**, 3865–3868 (1996).

[33] Dudarev, S. L., Botton, G. A., Savrasov, S. Y., Humphreys, C. J., Sutton, A. P. Electron-energy-loss Spectra and the Structural Stability of Nickel Oxide: An LSDA+U Study. *Phys. Rev. B* **57**, 1505–1509 (1998).

[34] Kong, F., Longo, R. C., Yeon, D., Yoon, J., Park, J., Liang, C., Kc, S., Zheng, Y., Doo, S., Cho, K. Multivalent Li-Site Doping of Mn Oxides for Li-Ion Batteries. *J. Phys. Chem. C* **119**, 21904–21912 (2015).

[35] Zhou, F. First-principles prediction of redox potentials in transition-metal compounds with LDA + U. *Phys. Rev. B* **70**, 235121 (2004).

[36] Bean, C. P., Livingston, J. D. Superparamagnetism. *J. Appl. Phys.* **30**, S120–S129 (1959).

[37] Caruntu, D., Caruntu, G., O'Connor, C. J. Magnetic properties of variable-sized Fe_3O_4 nanoparticles synthesized from non-aqueous homogeneous solutions of polyols. *J. Phys. D. Appl. Phys.* **40**, 5801–5809 (2007).

[38] Walz, F. The Verwey transition - a topical review. *J. Phys. C Condens.*

Matter **14**, R285 (2002).

[39] Promnopas, W., Promnopas, S., Phonkhokkong, T., Thongtem, T., Boonyawan, D., Yu, L., Wiranwetchayan, O., Phuruangrat, A., Thongtem, S. Crystalline phases and optical properties of titanium dioxide films deposited on glass substrates by microwave method. *Surf. Coatings Technol.* **306**, 69–74 (2016).

[40] López-Ortega, A., Lottini, E., Bertoni, G., Fernández, C. D. J., Sangregorio, C. Topotaxial phase transformation in cobalt doped iron oxide core/shell hard magnetic nanoparticles. *Chem. Mater.* **29**, 1279–1289 (2017).

Chapter 4

Controlled Atomic Layer Deposition of Aluminum Oxide on Sulfur-based Cathodes of Lithium-Sulfur Batteries

This chapter presents the modification of cathode materials of lithium-sulfur batteries by atomic layer deposition (ALD) using a conventional static ALD reactor. For this aim, the cathode of lithium-sulfur batteries was coated with alumina. The study is focused on low-temperature ALD coatings and the effect of the deposited material on the final cathode, after applying various numbers of deposition cycles. The alumina deposition results in an improved capacity of the system, especially at high current densities. Besides, the process temperature plays an important role, in particular for few-cycle ALD processes, aiding a better performance of the cell. It is also demonstrated that higher numbers of ALD cycles, especially at elevated process temperatures, lead to a considerable loss of sulfur, which in turn significantly lowers the cell performance. This work reports the optimal parameters for application of ALD to sulfur-based electrodes. Cathodes modified with alumina at low process temperatures and with low numbers of ALD cycles are proposed as alternative to conventional lithium-sulfur cathodes, since they have a higher specific capacity and Coulombic efficiency.

This chapter describes the part of the thesis that was under revision in the journal *Energy Technology* from Wiley-VCH at the time of submission of the thesis. The

ALD processes carried out in this chapter were performed at nanoGUNE, while the physicochemical and electrochemical characterizations of the samples were performed at Cidetec.

Article:

Controlled Atomic Layer Deposition of Aluminum Oxide to Improve the Performance of Lithium-Sulfur Batteries

Sarai García, Olatz Leonet, Eneko Azaceta, Iñaki Gómez, Antonio Reifs, J. Alberto Blazquez, Mato Knez, submitted to *Energy Technology*. Manuscript number: ente.201901432.

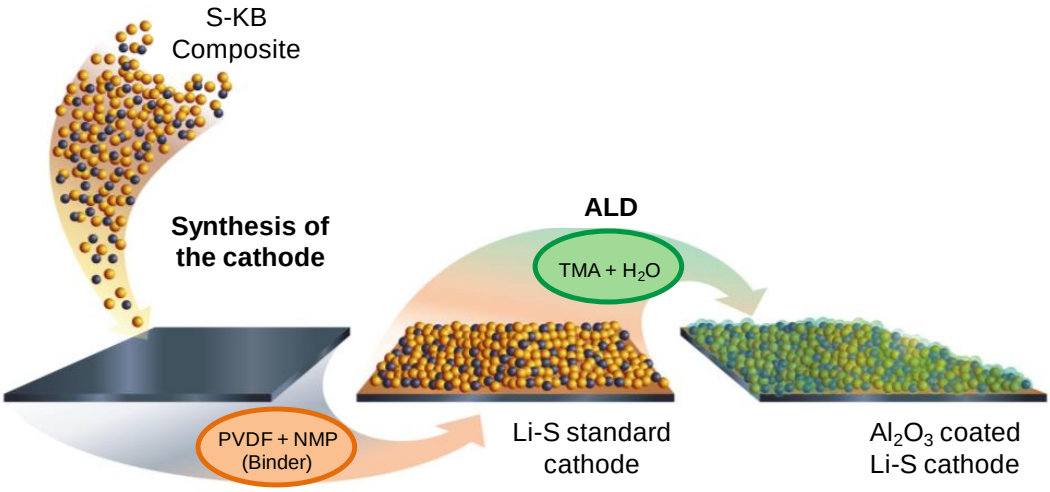

4.1. Introduction

Lithium-sulfur (Li-S) batteries are recognized as most promising next generation energy storage devices due to their overwhelming advantages in specific capacity and energy density. Thanks to the extraordinary properties of sulfur as cathodic material,[1]–[3] Li-S batteries are proposed as alternative to the conventional lithium-ion batteries (LIBs). However, Li-S batteries suffer from several issues that affect their commercial application. One of the most challenging issue to be solved is known as the "shuttle effect", resulting in high overcharge and poor Coulombic efficiency (CE) of the battery.[4],[5] In an effort to address the shuttle effect, various immobilizers and physically confining structures have been developed. In spite of their benefits, those strategies potentially affect the volume and weight of the cells, consequently reducing the Li-S energy density.[6]–[9]

A promising pathway to overcome the mentioned shuttle effect could be the use of atomic layer deposition (ALD).[10]–[13] In recent years, ALD enjoys a rapidly growing interest for emerging applications in energy storage devices [14]–[17] among other applications.[18]–[21] ALD provides ultimate control over the conformality of films and their thickness,[22]–[24] being more suitable for its application in batteries comparing with other deposition technologies.

In LIBs, the conformal deposited coatings and thickness control by means of ALD led to many improvements in the stability of this systems.[25] A protective layer, deposited by ALD, improves the stability of the LIBs by suppressing side reactions between the electrolyte and electrodes, thereby preventing the decomposition of the electrolyte.[26],[27] More recently, ALD has been evaluated for improving Li-S batteries. The application of a protective layer on the electrodes of this kind of batteries has proven to enhance the Li-S batteries´ performance, especially through reducing the polysulfide dissolution by absorbing or bonding them to the deposited material.[16]

Alumina (Al_2O_3) is the most popular metal oxide for ALD-type of deposition, being economic and facile.[28],[29] Already few cycles of alumina deposition can greatly increase the reversible capacity and long-term durability of the cathodes in conventional lithium-ion [15] and lithium-sulfur batteries.[6] However, Al_2O_3 is

electrochemically inactive and insulating, and it does not make any contribution to the capacity of a battery. Thus, a thick alumina coating can serve as a barrier for the Li-ion mobility and in this way decrease the total capacity of the battery.[1] On the other hand, if the number of alumina cycles is not sufficient to generate a coating, dispersed clusters or islands will be generated on the cathode that might act as a chemical absorber for binding polysulfides, thereby reducing the shuttling to the anode and improving the capacity retention of S cathodes.[30]

In this work, it is demonstrated that applying a specific number of ALD cycles of Al_2O_3 on prefabricated sulfur cathodes for Li-S batteries can reduce the shuttle effect and thereby greatly improve the cyclability and capacity retention of fabricated Li-S batteries. A range of process temperatures and various ALD cycles numbers are tested in order to minimize sublimation of sulfur and thereby, the loss of this active material during the ALD process. In addition to the process temperature, purge times of ALD precursors are also modified to avoid parasitic CVD, which might occur due to the applied low process temperatures. In this case, longer purging times are needed to remove the excess of precursors and by-products and in this way avoid the mentioned parasitic CVD. Inductively coupled plasma with mass spectroscopy (ICP-MS) and thermogravimetric analysis (TGA) were used to study the deposition of alumina on the cathodes and sulfur sublimation during the ALD process. Thanks to the electrochemical analysis, it is found that a deposition of alumina with as few as 2 ALD cycles at 85 °C results in an insignificant sulfur loss (<1%) and greatly improves the specific capacity and Coulombic efficiency (CE) of the lithium-sulfur batteries, especially at high current densities.

4.2. Experimental section

4.2.1. Fabrication of cathodes

Cathodes were produced using 60 wt% commercial sulfur powder (<40 μm Merck) in the final formulation. A mixture of 80 wt% sulfur (S) and 20 wt% Ketjen Black (KB) 600JD (AkzoNobel) was homogeneously mixed by ball-milling in ethanol for 3h. The mixed carbon-sulfur powder was heated at 300 °C for 2h in order to

properly impregnate the sulfur on the high-area carbon powder matrix. Afterwards, the dried powder was added to a solution of polyvinylidene fluoride (PVDF) 5130 (SOLVAY) in N-methylpyrrolidone (NMP) to form the cathodic slurry (see Figure 19). An additive conductor was added (carbon black, TIMCAL C-NERGY™ SUPER C45), capable of forming micellar structures. The whole mixture was sonicated for 30 minutes and stirred overnight by using a mechanical mixer (RW 20 digital, IKA) for ensuring a homogeneous slurry. These slurries were then blade cast onto a carbon-coated aluminum foil (MTI Corp.) and dried at 60 °C under dynamic vacuum during 12 h before the cell assembly.

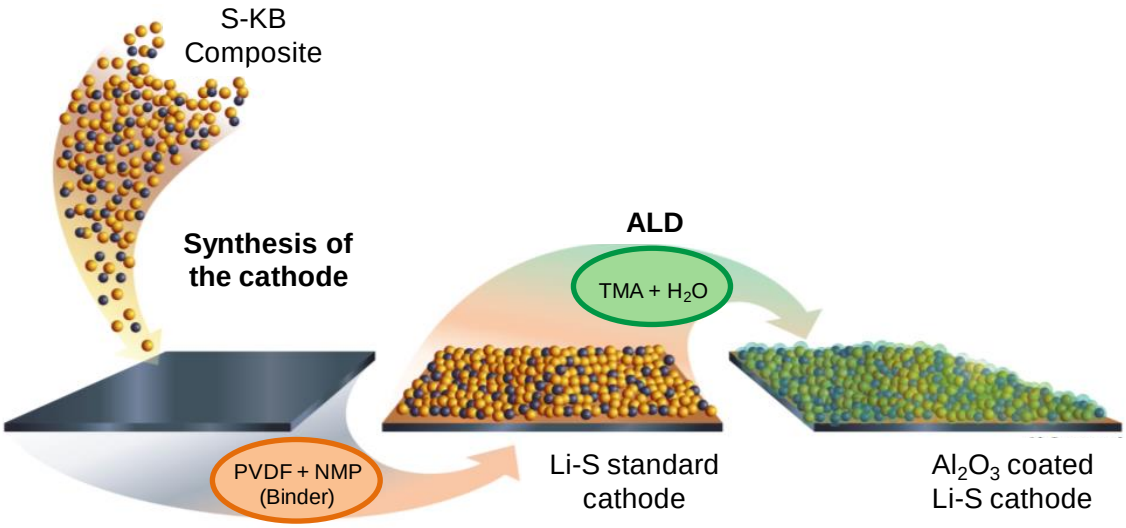

Figure 19. Schematic illustration of electrode assembly and alumina coating by ALD for lithium-sulfur batteries.

4.2.2. ALD process

The fabricated cathodes for Li-S coin cell batteries were used as a substrate in ALD experiments (see Figure 19). The coating of each cathode was performed in a commercial ALD reactor (Savannah S100, Cambridge NanoTech Inc). The processes were carried out under a constant nitrogen gas flow of 20 standard cubic centimeters per minute (sccm) at various process temperatures, 85 °C, 80 °C, 75 °C and 60 °C. Trimethyl aluminum (TMA), obtained from Sigma Aldrich, and

demineralized water (oxygen source), were used as ALD precursors. Coating processes were run with 2, 5, 10 and 20 ALD cycles. The coated cathodes were prepared following a typical ALD timing sequence expressed as t_1-t_2-t_3-t_4, where t_1 is the exposure time of the first precursor, t_2 is the purge time following the first exposure, t_3 is the exposure time of the second precursor, t_4 is the purge time following the exposure to the second precursor. The times corresponding to t_1-t_2-t_3-t_4 were 10-x-10-x, where x was varied as follows: for 85-80 °C x= 60, for 75 °C x=90 and for 60 °C x=120. All values are given in seconds (s). The pulsing times were a function of the vapor pressure of each precursor, being 0,1 s for TMA and 0,05 s for water vapor. The processes were performed under vacuum at a base pressure of 1 mbar.

4.2.3. Physicochemical characterization

The physicochemical properties of the produced electrodes were characterized to confirm alumina deposition and determine the sulfur loss during the ALD process. Elemental analysis of alumina was carried out using ICP-MS (Induced Couple Plasma with Mass Spectroscopy, performed with an iCAP-Q, Thermo Fisher Scientific GmbH, Germany), which provides the mass fraction of aluminum in the coated samples, Al wt%. To determine Al wt% in the samples, a small amount of the electrode material (dried slurry), without aluminum foil, was dissolved in a pre-prepared solution of 0,5 $mg \cdot mL^{-1}$ of nitric acid in water. After dissolution, the samples were aged for 72 hours and diluted in MQ (milli-Q) water in a ratio of 1:25 to obtain 2,7 % HNO_3, 20 $\mu g \cdot mL^{-1}$. The samples were then analyzed with ICP-MS to determine the mass fraction of aluminum in the samples. The elemental sulfur content of the cathodes was determined via thermogravimetric analysis (TGA) using a Netsch STA. A small amount of powder from the electrode material (dried slurry without aluminum foil) was thermally ramped from 25 °C (room temperature) to 400 °C with a heating rate of 10 $°C \cdot min^{-1}$ under N_2 atmosphere.

4.2.4. Li-S cell electrochemical characterization

The fabricated cathodes were assembled into lithium-sulfur (Li-S) coin cells. The cathodes were prepared with a sulfur loading of 1,8 $mg_S \cdot cm^{-2}$ and a theoretical capacity of 2,7 $mA \cdot h \cdot cm^{-2}$, derived from the theoretical capacity of elemental sulfur (1672 $mA \cdot h \cdot g^{-1}$). One layer of a commercial polyolefin separator, Celgard 2501, soaked with 50 µL of 0,38 M solution of Bis(trifluoromethane) sulfonimide lithium salt (LiTFSI) (Sigma-Aldrich) and 0,32 M of lithium nitrate ($LiNO_3$) (Sigma-Aldrich) as additive in a 1/1(v/v) mixture of dimethoxyethane (DME) (BASF) and dioxolane (DOL) (BASF), was placed between the electrodes. Lithium foil (0,05 mm, Rockwood Lithium) was used as the anode in coin half cells (2025, Hohsen). Vacuum drying of electrodes and cell crimping has been performed in a dry room with a dew point below -50 °C. Thereafter, the assembled cells were aged for 20 hours and then cycled in a BaSyTec Cell Test System (Germany) at 25±1 °C controlled by air conditioning.

The electrochemical behavior of the obtained ALD coated sulfur electrodes was evaluated at different C-rates (C/10, C/5, C/2,5, 1C and 2C) considering the theoretical capacity of elemental sulfur (1672 $mA \cdot h \cdot g^{-1}$). The cycle life of the coin cells was investigated within a 1,7-2,6 V interval at C/5 charge-discharge current rates.

4.3. Results and discussion

Standard sulfur electrodes have been coated with alumina (Al_2O_3) using ALD at various process temperatures (60 °C, 75 °C, 80 °C and 85 °C) and under vacuum. The characterization of the samples by ICP-MS, as shown in Table 2, confirms successful alumina deposition after each of the processes.

Theoretically, in ALD the amount of deposited alumina increases almost linearly with the number of cycles. If ALD processes are performed within a material-specific temperature window (ALD window), the cycle-dependent linear growth behavior is largely independent of the process temperature. There is an exception for our samples coated at 60 °C. In this case, the tendency of the deposited

alumina varies independently on the temperature and cycle number. This is attributed to the process being outside of the ALD window of alumina.[12],[31] The deposition process results in non-linear and scattered amounts of Al among the samples. Most likely the water precursor is not completely evaporated during purging, but rather some amount is remaining bound to the surface of the samples, reacting with the subsequent delivery of TMA and thus inducing some level of parasitic CVD coating in addition or instead of ALD. Furthermore, the activation energy that needs to be overcome for an ALD reaction, is higher at those temperatures. Consequently, the results are not consistent with the cases where the process is largely within the ALD window.

Table 2. ICP-MS derived aluminum amounts in ALD-coated sulfur cathodes for various process temperatures as a function of the number of processing cycles.

% Al (w/w)				
Temperature (°C)	2 ALD	5 ALD	10 ALD	20 ALD
60	0,46	10,78	10,46	7,88
75	0,55	1,39	5,64	13,17
80	0,44	1,71	4,03	10,59
85	1,97	1,75	5,80	13,10

Sulfur is the active cathodic material in Li-S batteries. Therefore, a reduction of the sulfur to carbon ratio in the electrode formulation leads to a lower capacity of the system. In the course of an ALD deposition, with the surface reaction being of chemical nature, a loss of the initial sulfur amount can be expected. To quantify the sulfur loss during the ALD processes, thermogravimetric analyses have been done for each sample after the ALD treatment. Figure 20 shows the percentual sulfur loss after various ALD cycle numbers for the studied process temperatures. The general trend is obvious: The higher the temperature is, the higher is the loss of sulfur. With respect to the cycle numbers, the same trend can be observed, namely the amount of sulfur decreases considerably with an increasing number of ALD cycles.

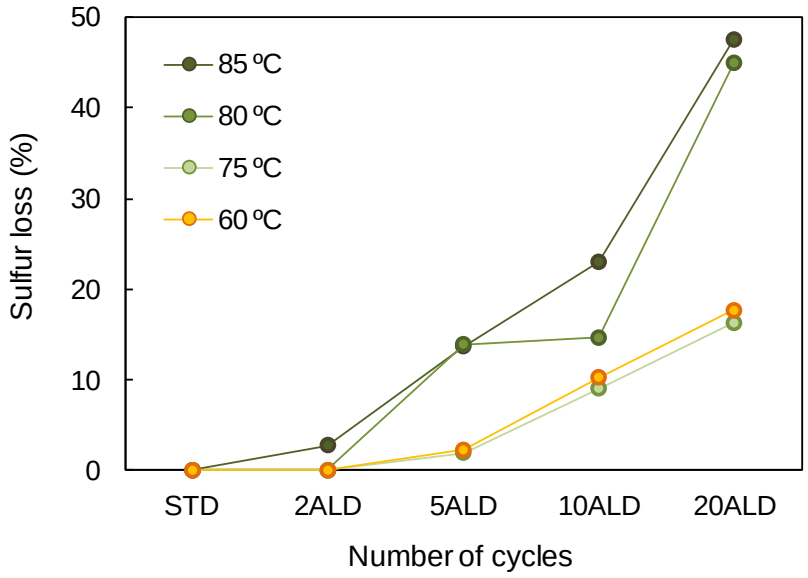

Figure 20. Loss of sulfur in the cathodes resulting from ALD processing at the indicated process temperatures as a function of the number of applied ALD cycles.

Two observable tendencies allow dividing the samples into two groups; samples done at 60-75 ºC and at 80-85 ºC. In the first case, processes at 2 and 5 ALD cycles have an acceptable sulfur loss of less than 5 %. In the second group (80-85 ºC), only the samples coated with 2 ALD cycles are showing a comparable and acceptable loss of sulfur. On the other extreme of applied cycle numbers, namely 20 ALD cycles, the significant loss of sulfur of more than 15 % for all applied temperatures, which resulted in discarding those samples from further electrochemical testing.

After physicochemical characterization, the samples were tested electrochemically. The most promising electrodes from previous characterizations (containing around 40-60 wt% of sulfur in the final cathode formulation) were selected for testing. 2025 type coin cells, assembled with those electrodes, were tested at C/10, C/5, C/2,5, 1C and 2C C-rates and their cyclability was analyzed at C/5.

Figure 21 shows the electrochemical performance of 2 ALD, 5 ALD and 10 ALD-coated alumina electrodes, processed at different ALD process temperatures

(60 °C, 75 °C, 80 °C and 85 °C), in Li-S batteries at different C-rates. If compared to the standard sample (cathode without ALD coating), only the assembly with the cathode after with 2 ALD cycles showed an improved performance of the battery, especially at elevated C-rates (1C, 2C), as depicted in Figure 21a; the higher the current density is, the better is the cell performance regarding the standard cathode. The reason could be the volume changes resulting from the different sulfur species generated during the redox reaction, which happens on a rather short time scale. Thanks to ALD, those volume changes could be largely suppressed and in this way the electron conductivity in fast kinetic reactions (high C-rates processes) improved. Those results are even more evident with higher processing temperatures, meaning that the obtained enhancement is dependent on the process temperature. Particularly at 85 °C, the capacity of the system increases from 400 mAh · g_S^{-1} in the standard sample to 600 mAh · g_S^{-1} in the 2 ALD-coated sample for high current densities (2C). After increasing the number of ALD cycles to 5 and 10 (Figure 21b and Figure 21c, respectively), a tendency similar to the previous case (2 ALD) can be observed, however, with some slight differences: At low C-rates an improvement of ALD-treated samples with respect to the standard sample is not very obvious in neither case.

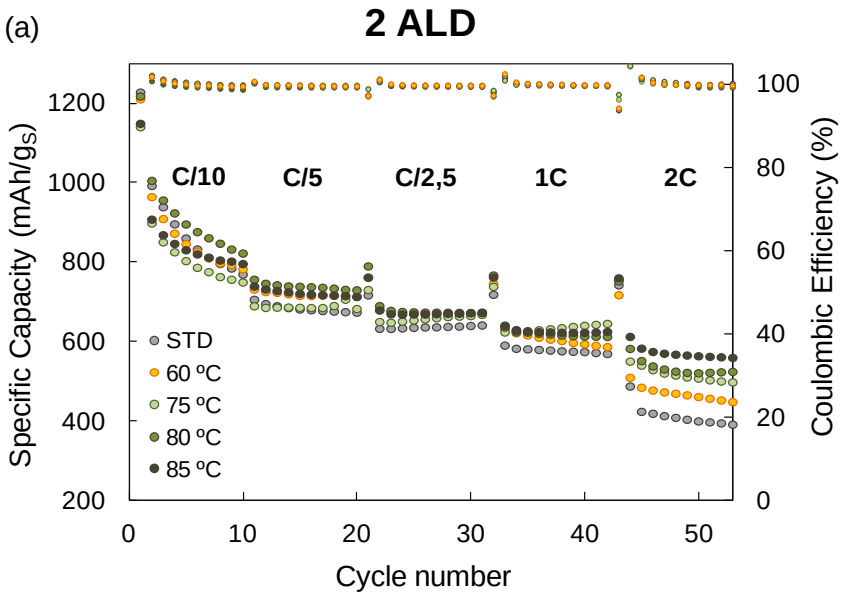

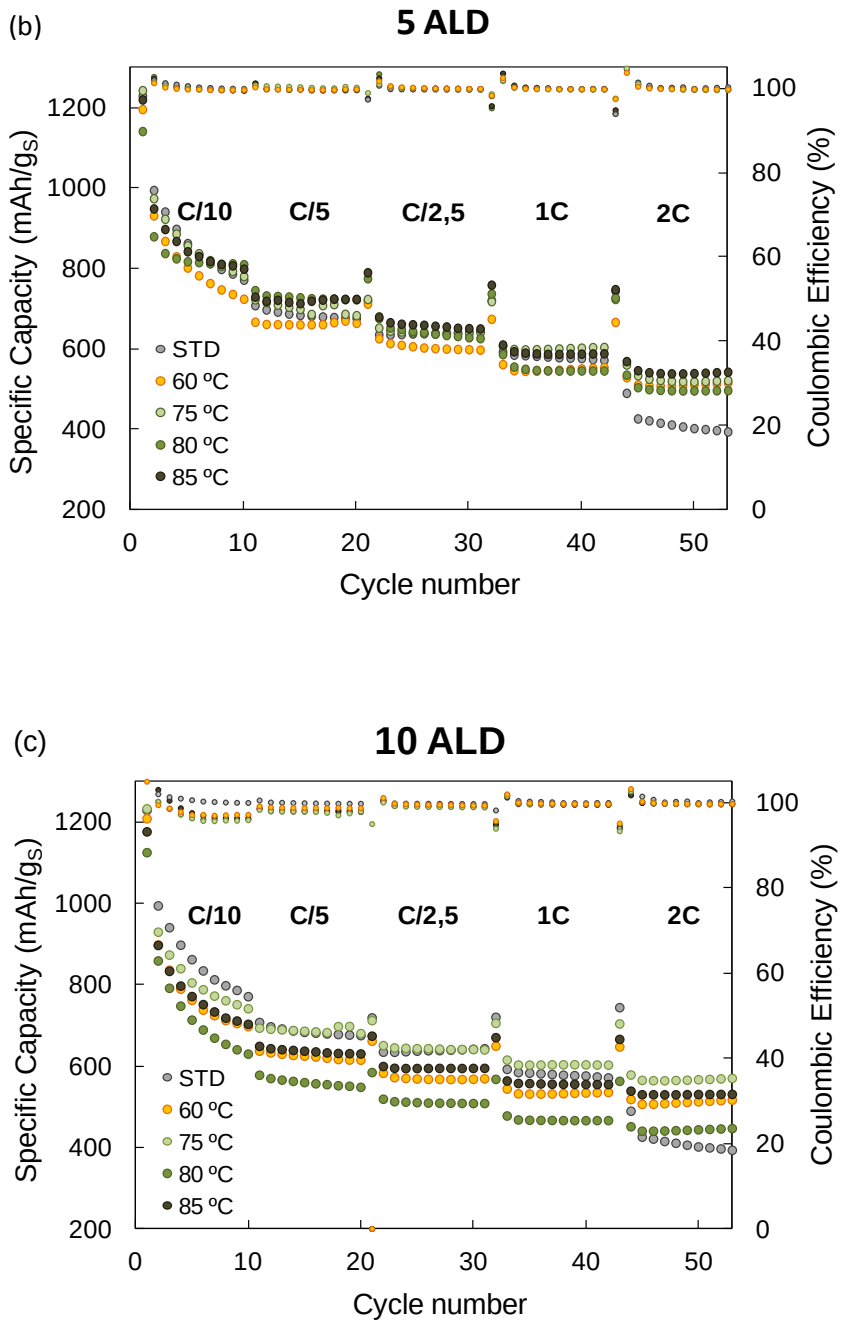

Figure 21. Electrochemical performance of 2025 type Li-S coin cells at different C-rates for (a) 2-ALD, (b) 5-ALD and (c) 10-ALD coated sulfur electrodes (sulfur loading of 1,8 mg · cm^{-2}) at ALD process temperatures of 60 °C, 75 °C, 80 °C and 85 °C.

However, at high current densities (2C) the cell performance is considerably better with ALD-processed cathodes than in the case of standard cathodes, with the capacity retention being improved for all the samples. While with 5 ALD-coated samples the performance of the battery enhances significantly from 400 mAh · g_S^{-1} to around 600 mAh · g_S^{-1} for all process temperatures, with 10 ALD-coated electrodes this distribution is wider, and the enhancement is not as good. The capacity is increased to almost 600 mAh · g_S^{-1} in the best case, the 10 ALD-coated electrode at 75 °C.

Looking at the cycle life of the cells, Figure 22a shows enhanced capacity retention during cycling at C/5 with 2-ALD samples processed at different process temperatures. This is most strongly expressed with samples processed at 85 °C. Here, the specific capacity of the cell increases from 700 mAh · g_S^{-1} to almost 800 mAh · g_S^{-1}, even after 50 charge-discharge cycles. However, with higher numbers of ALD cycles, that is, samples 5-ALD and 10-ALD, the cycle life and capacity retention of the cathodes do not improve at all. For 5-ALD, only the sample coated at 85 °C is better than the reference sample, increasing the capacity up to 800 mAh · g_S^{-1} even after 50 charge-discharge cycles (Figure 22b), while for the 10-ALD samples, none of the modified samples shows improvement (Figure 22c).

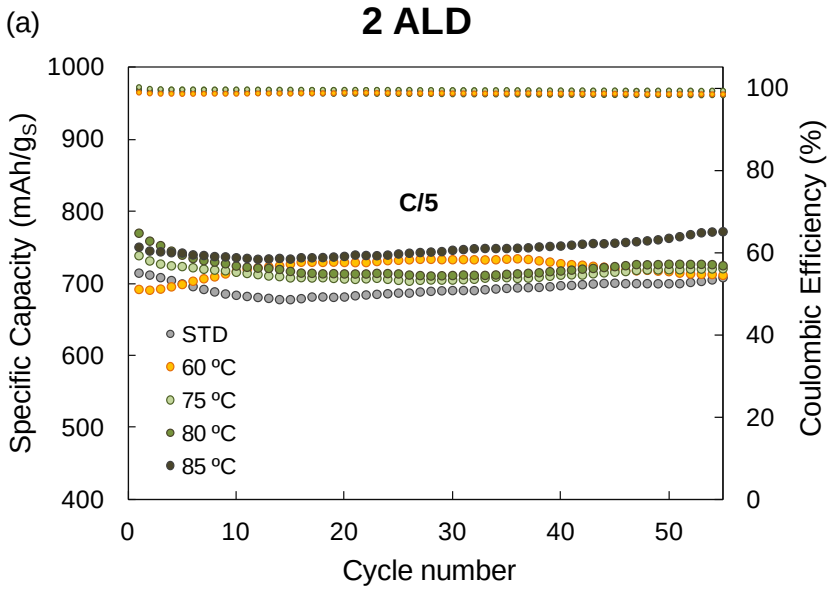

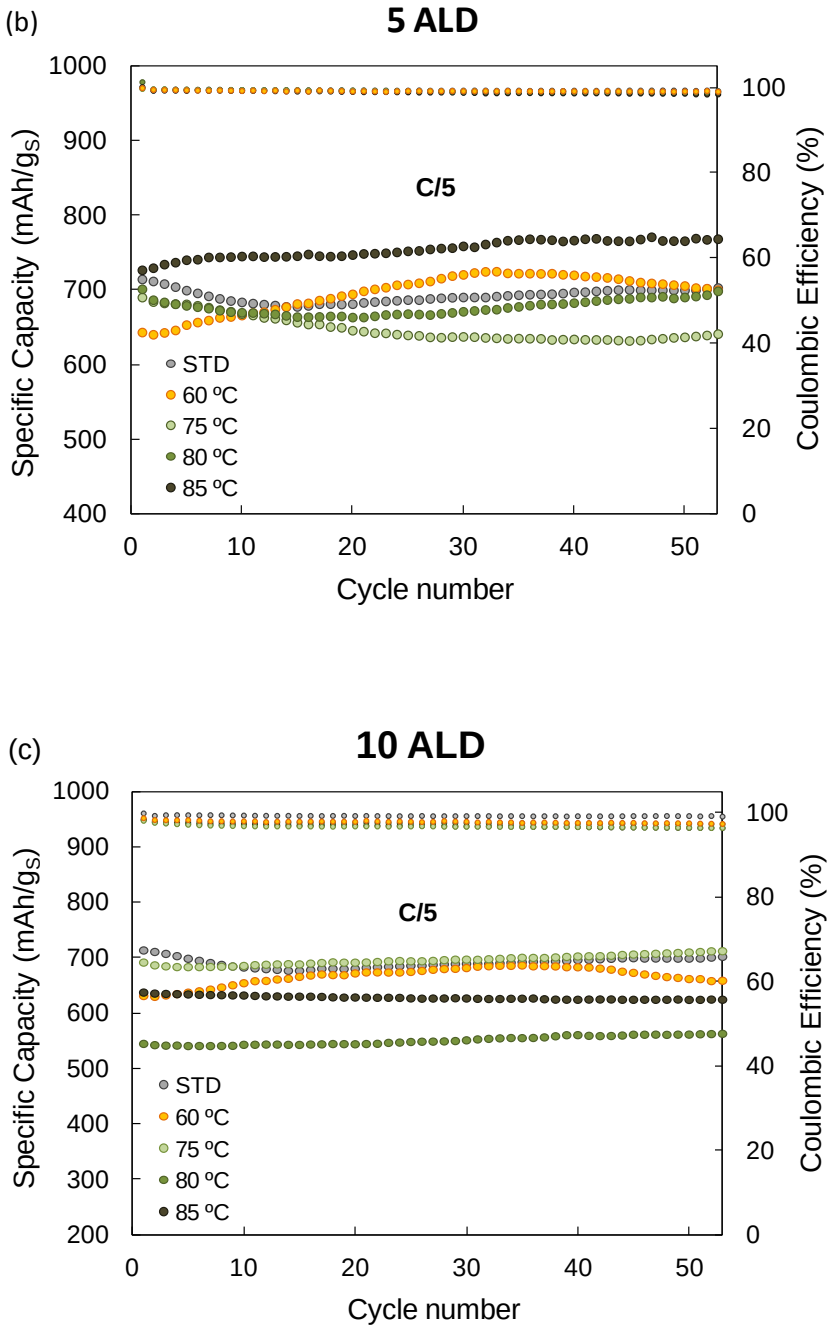

Figure 22. Cycling performance at C/5 of (a) 2-ALD, (b) 5-ALD and (c) 10-ALD sulfur electrodes (with a sulfur loading of 1,8 mg · cm^{-2}) at ALD process temperatures of 60 ºC, 75 ºC, 80 ºC and 85 ºC.

It is worth mentioning that for the 10-ALD samples the sulfur loss is ≥10 % for all processing temperatures (see Figure 20). Consequently, the results are not comparable with the standard sample. The sulfur amount in 10-ALD samples is deviating much more than the other ALD modified samples regarding the standard cathode, while the applied electrochemical conditions are the same. For this reason, the 10-ALD sulfur cathodes are not a suitable alternative for standard sulfur cathodes.

The electrochemical results further show that ALD processing does not induce significant differences to the performance of the lithium-sulfur batteries at low current densities (from C/10 to 1C). However, for high C-rates (2C) the performance is enhanced for all ALD processed samples, at any processing temperature. This may be attributed to trapping of polysulfides by alumina, which can bind polysulfides from the cathode, thus suppressing their dissolution and a resulting generation of extra resistance to the electronic conductivity of the cell. At high current densities this improvement is more evident, since the kinetic of the reaction is faster.

Apart from the trapping of polysulfides by Al_2O_3, another reason for the capacity improvement in ALD-modified cathodes could be the cohesion of the particles at the surface electrode with the particles in the subsurface, enhanced by the deposited alumina. This will enhance both the electronic conductivity and the electrolyte absorption by the electrode, resulting from the cohesions generated by deposited alumina which can bind electrode particles improving the contact with each other. However, since alumina is an insulator, the higher amount of deposited material on the surface of the cathode in the case of 5-ALD and 10-ALD samples can worsen the performance of the cathode by increasing its resistance. The mentioned sulfur loss during ALD processing for those samples adds another issue to the described drawbacks.

Given the physicochemical and electrochemical analysis, the 2-ALD electrode processed at 85 °C shows most promise as alternative to the standard sulfur cathode. It is the only sample that shows an improvement of the cell capacity

both for different C-rates and cycle life. Moreover, the deposition of only 2 ALD cycles saves time and precursors during the ALD process.

The charge-discharge voltage profiles of 2-ALD, processed at 85 °C, and the standard sample for different C-rates are compared. Figure 23 shows that at low C-rates there is no significant difference in the profiles of the samples with the standard cathode and the 2-ALD cathode. Moreover, at low C-rates (C/10), ALD worsens the cell performance. However, with increasing the C-rate the discharge capacity of the ALD-coated cathode improves, as also shown previously in the current densities and cycle life analyses. For instance, at C/5 the discharge capacity is increased, namely from 680 $mAh \cdot g_S^{-1}$ in the standard cathode to around 750 $mAh \cdot g_S^{-1}$ in the 2-ALD sample. Furthermore, for the highest C-rate (2C) the discharge capacity increases considerably from 400 $mAh \cdot g_S^{-1}$ in the standard cathode, to around 600 $mAh \cdot g_S^{-1}$ in 2-ALD sample.

On the other hand, one can see two discharge plateaus, one between 2,4 and 2,3 V and another at 2,1 V for all C-rates except of 2C. In the latter case, the first plateau is reduced from the standard cell, while the 2-ALD modified cell still maintains it. This shows a moderate improvement of the specific capacity of the test cell, but this increased potential could significantly raise the energy density in a real battery prototype.

Regarding polarization, ALD is decreasing the resistance of the electrochemical process especially at high C-rates. As stated above, ALD enhances the current density, meaning that electrolyte penetration and its absorption is enhanced with the presence of small amounts of alumina, improving the wettability of the cathode as well as the cohesion of sulfur particles and reducing the shuttle effect due to the blocking of polysulfides.

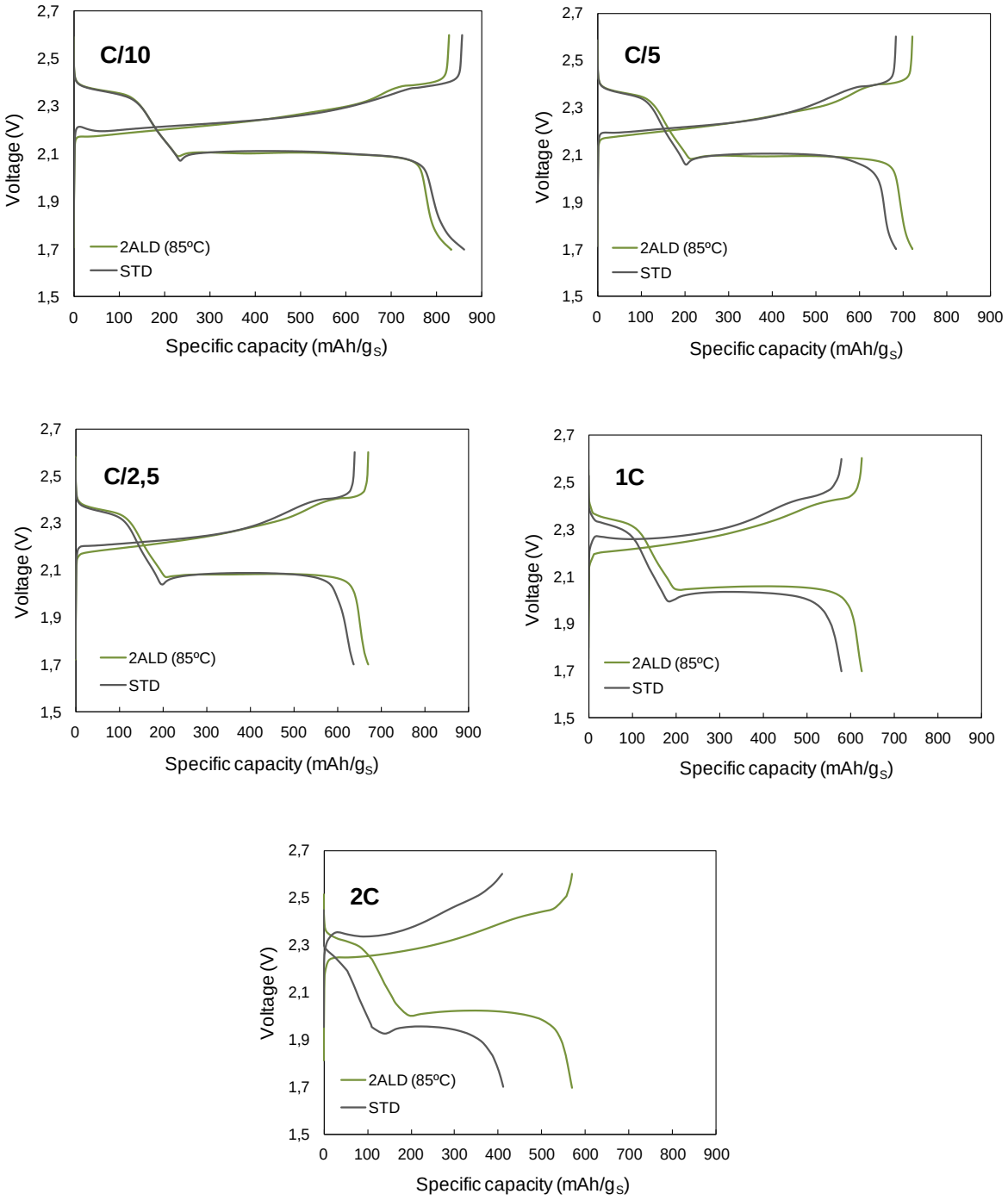

Figure 23. Voltage profiles of the standard electrode (STD) in comparison to 2-ALD coated electrodes processed at 85 ºC at different C-rates.

4.4. Conclusions

In this chapter, it is demonstrated that applying ALD directly to the produced cathodes improves the performance of Li-S batteries. The optimal parameters for the ALD processes involve deposition of alumina with few ALD cycles at low temperatures. Besides the improved performance of the batteries, this way of processing is more cost-effective and time efficient.

The physicochemical characterization of the materials confirmed deposition of alumina on the sulfur cathodes by ALD, which improves the cohesion of the particles between the electrode surface and subsurface area, thus improving the electronic conductivity and increasing the absorption of the electrolyte by the cathode. Furthermore, alumina may bind polysulfides, thereby blocking their transport to the anode and their dissolution in the electrolyte.

The loss of sulfur during the ALD process, which results from elevated process temperatures and long exposure times of the substrate to the precursors, has negative consequences for the performance of the batteries. For this reason, samples processed with larger numbers of ALD cycles, which resulted in less than 40 wt% of sulfur in the cathode formulation, were discarded from electrochemical performance testing.

Among the tested samples, the cell performance showed that at low C-rates (C/10-1C) ALD did not improve the efficiency of the cells considerably. However, at high C-rates (2C), the capacity of the system was significantly increased for ALD-coated samples with 2, 5 and 10 applied ALD cycles. The best performance was observed from 2-ALD samples processed at 85 ^{o}C. Compared to the standard cathode, this sample showed better capacity retention for low and high current densities, meaning that only 2 ALD cycles are sufficient to improve the cell performance.

References

[1] Yu, M., Yuan, W., Li, C., Hong, J., Shi, G. Performance enhancement of a graphene – sulfur composite as a lithium – sulfur battery electrode by coating with an ultrathin Al_2O_3 film via atomic layer deposition. *J. Mater. Chem. A* **2**, 7360–7366 (2014).

[2] G. Bruce, P., A. Freunberger, S., J. Hardwick, L., Tarascon, J.-M. Li – O_2 and Li – S batteries with high energy storage. *Nat. Mater.* **11**, 19–30 (2012).

[3] Yamin, H., Gorenshtein, A., Penciner, J., Sternberg, Y., Peled, E. Lithium Sulfur Battery. *J. Electrochem. Soc.* **135**, 1045–1048 (1988).

[4] Kim, H., Lee, J. T., Lee, D., Magasinski, A., Cho, W. Plasma-Enhanced Atomic Layer Deposition of Ultrathin Oxide Coatings for Stabilized Lithium – Sulfur Batteries. *Adv. Energy Mater.* **3**, 1308–1315 (2013).

[5] Li, X., Liu, J., Wang, B., Banis, M. N., Xiao, B., Li, R., Sham, T.-K., Sun, X. Nanoscale stabilization of Li–sulfur batteries by atomic layer deposited Al_2O_3. *RSC Advances* **4**, 27126–27129 (2014).

[6] Meng, X., Liu, Y., Cao, Y., Ren, Y., Lu, W., Elam, J. W. High-Performance High-Loading Lithium – Sulfur Batteries by Low Temperature Atomic Layer Deposition of Aluminum Oxide on Nanophase S Cathodes. *Adv. Mater. Interfaces* **4**, 1700096 (2017).

[7] Ji, L., Rao, M., Zheng, H., Zhang, L., Li, Y., Duan, W., Guo, J., Cairns, E. J., Zhang, Y. Graphene Oxide as a Sulfur Immobilizer in High Performance Lithium/Sulfur Cells. *J. Am. Chem. Soc.* **133**, 18522–18525 (2011).

[8] Kresse, G., Furthmiiller, J. Efficiency of ab-initio Total Energy Calculations for Metals and Semiconductors Using a Plane-wave Basis Set. *Comput. Mater. Sci.* **6**, 15–50 (1996).

[9] Wang, Z., Li, X., Cui, Y., Yang, Y., Pan, H., Wang, Z., Wu, C., Chen, B., Qian, G. A Metal−Organic Framework with Open Metal Sites for Enhanced Confinement of Sulfur and Lithium − Sulfur Battery of Long Cycling Life. *Cryst. Growth Des.* **13**, 5116–5120 (2013).

[10] Parsons, G. N., George, S. M., Knez, M. Progress and future directions for atomic layer deposition and ALD-based chemistry. *MRS Bull.* **36**, 865–871 (2011).

[11] George, S. M. Atomic layer deposition: an overview. *Chem. Rev.* **110**, 111–131 (2009).

[12] Johnson, R. W., Hultqvist, A., Bent, S. F. A brief review of atomic layer deposition: From fundamentals to applications. *Mater. Today* **17**, 236–246 (2014).

[13] Lee, F., Marcus, S., Shero, E., Wilk, G., Swerts, J., Maes, J. W., Blomberg, T., Delabie, A., Gros-Jean, M., Deloffre, E. Atomic layer deposition: An enabling technology for microelectronic device manufacturing. *ASMC (Advanced Semicond. Manuf. Conf.) Proc.* 359–365 (2007).

[14] Knoops, H. C. M., Donders, M. E., van de Sanden, M. C. M., Notten, P. H. L., Kessels, W. M. M. Atomic layer deposition for nanostructured Li-ion batteries. *J. Vac. Sci. Technol. A Vacuum, Surfaces, Film.* **30**, 010801 (2012).

[15] Jung, Y. S., Cavanagh, A. S., Riley, L. A., Kang, S. H., Dillon, A. C., Groner, M. D., George, S. M., Lee, S. H. Ultrathin direct atomic layer deposition on composite electrodes for highly durable and safe Li-Ion batteries. *Adv. Mater.* **22**, 2172–2176 (2010).

[16] Yan, B., Li, X., Bai, Z., Song, X., Xiong, D., Zhao, M., Li, D., Lu, S. A review of atomic layer deposition providing high performance lithium sulfur batteries. *J. Power Sources* **338**, 34–48 (2017).

[17] Niu, W., Li, X., Karuturi, S. K., Fam, D. W., Fan, H., Shrestha, S., Wong,

L. H., Tok, A. I. Y. Applications of atomic layer deposition in solar cells. *Nanotechnology* **26**, 064001 (2015).

[18] Skoog, S. A., Elam, J. W., Narayan, R. J. Atomic layer deposition: medical and biological applications. *Int. Mater. Rev.* **58**, 113–129 (2013).

[19] Narayan, R. J., Adiga, S. P., Pellin, M. J., Curtiss, L. A., Stafslien, S., Chisholm, B., Monteiro-Riviere, N. A., Brigmon, R. L., Elam, J. W. Atomic layer deposition of nanoporous biomaterials. *Mater. Today* **13**, 60–64 (2010).

[20] Knez, M., Kadri, A., Wege, C., Gösele, U., Jeske, H., Nielsch, K. Atomic layer deposition on biological macromolecules: metal oxide coating of tobacco mosaic virus and ferritin. *Nano Lett.* **6**, 1172–1177 (2006).

[21] Knez, M. ALD a Versatile Tool for Nanostructuring. *Mater. Matters* **3**, 1–7 (2008).

[22] García-García, S., López-Ortega, A., Zheng, Y., Nie, Y., Cho, K., Chuvilin, A., Knez, M., Chuvilin, A. Ligand-induced reduction concerted with coating by atomic layer deposition on the example of TiO_2 - coated magnetite nanoparticles. *Chem. Sci.* **10**, 2171–2178 (2019).

[23] Azpitarte, I., Zuzuarregui, A., Ablat, H., Ruiz-Rubio, L., López-Ortega, A., Elliott, S. D., Knez, M. Suppressing the Thermal and Ultraviolet Sensitivity of Kevlar by Infiltration and Hybridization with ZnO. *Chem. Mater.* **29**, 10068–10074 (2017).

[24] Leskelä, M., Niinisto, J., Ritala, M. *Atomic Layer Deposition.* vol. 4 (2014).

[25] Yan, P., Zheng, J., Zhang, X., Xu, R., Amine, K., Xiao, J., Zhang, J. G., Wang, C. M. Atomic to Nanoscale Investigation of Functionalities of Al_2O_3 Coating Layer on a Cathode for Enhanced Battery Performance. *Chem. Mater.* **28**, 857–863 (2016).

[26] Ma, L., Nuwayhid, R. B., Wu, T., Lei, Y., Amine, K., Lu, J. Atomic Layer

Deposition for Lithium-Based Batteries. *Adv. Mater. Interfaces* **3**, 1600564 (2016).

[27] Sun, Y. K., Lee, M. J., Yoon, C. S., Hassoun, J., Amine, K., Scrosati, B. The role of AlF_3 coatings in improving electrochemical cycling of Li-enriched nickel-manganese oxide electrodes for Li-ion batteries. *Adv. Mater.* **24**, 1192–1196 (2012).

[28] Puurunen, R. L. Surface chemistry of atomic layer deposition : a case study for the trimethylaluminum / water process. *J. Appl. Phys.* **97**, 121301-121301–52 (2005).

[29] Groner, M. D., Fabreguette, F. H., Elam, J. W., George, S. M. Low-Temperature Al_2O_3 Atomic Layer Deposition. *Chem. Mater.* **16**, 639–645 (2004).

[30] Han, X., Xu, Y., Chen, X., Chen, Y., Weadock, N., Wan, J., Zhu, H., Liu, Y., Li, H., Rubloff, G., Wang, C., Hu, L. Reactivation of dissolved polysulfides in Li – S batteries based on atomic layer deposition of Al_2O_3 in nanoporous carbon cloth. *Nano Energy* **2**, 1197–1206 (2013).

[31] Zhu, Z., Sippola, P., Lipsanen, H., Savin, H., Merdes, S. Influence of plasma parameters on the properties of ultrathin Al_2O_3 films prepared by plasma enhanced atomic layer deposition below 100°C for moisture barrier applications. *Jpn. J. Appl. Phys.* **57**, 2–8 (2018).

Chapter 5

Atomic Layer Deposition on Sulfur-Carbon Composites using a Fluidized Bed Reactor for Lithium-Sulfur Batteries

In this chapter aluminum oxide is deposited on sulfur-carbon powder composite from the cathode of lithium-sulfur batteries by atomic layer deposition (ALD) using a fluidized bed reactor (FBR). As a result, the sulfur-carbon composite particles are embedded in alumina shells and bridged with deposited alumina. In this way, variable sulfur loaded (up to 3,6 $mg \cdot cm^{-2}$), uniform and crack-free electrodes are successfully generated. These new electrodes significantly exceed the performance of current electrodes with respect to cycle life and capacity of the resulting lithium-sulfur batteries. Moreover, the scale-up of the employed FBR technology to perform ALD processes is feasible and facile, allowing the coating of large amount of powders and its extension to industrial applications.

This chapter describes the part of the thesis that was submitted for a patent application at the time of the submission of the thesis. Its content is confidential until the final acceptance of the patent.

5.1. Introduction

Lithium-sulfur (Li-S) batteries moved into the focus of researchers in the recent years for their numerous benefits. Namely, the high theoretical specific capacity of sulfur (1672 $mAh \cdot g^{-1}$) and its high theoretical specific energy density (2567 $Wh \cdot kg^{-1}$), largely exceeds that of Li-ion batteries, where the theoretical specific energy is around 300 $Wh \cdot kg^{-1}$.[1]–[3]

However, the novel Li-S technology has few obstacles to be overcome in order to allow its optimal exploitation. In order to address some of those issues, especially the ones from the cathodic side as reported in the thesis introduction, sulfur is usually confined in a micro-nanosized carbon matrix (conductive material), which enhances sulfur utilization, traps dissolved polysulfides, thus minimizing shuttle reactions, and improves the cycling performance of the battery. However, the amount of carbon support required can be significant, which greatly reduces the Li-S energy density. Nanostructured sulfur-carbon composites are needed in order to maximally utilize the sulfur. On the practical side, one of the main challenges for the cathode production is the difficulty of forming a homogeneous coating of the sulfur-carbon composite with a reasonable thickness on the current collector. Namely, utilizing traditional slurry coating processes commonly causes cracks or pinholes.[2],[4] Upon drying the electrode after slurry deposition, the solvent evaporation causes a significant volume reduction, which leads to the mentioned cracks and pores and consequently to negative effects on the electronic conductivity of the cell. This issue has been addressed in several ways, by altering the binder,[5] increasing the particle size or introducing conductive polymers.[6],[7] In addition, various immobilizers[8] and physically confining structures[9] have been developed, but in most of the cases those materials tend to significantly increase the weight and volume of the cathode, thereby reducing the Li-S energy density.

The use of atomic layer deposition (ALD) for improving the efficiency of lithium-sulfur batteries was shown to be very beneficial.[10]–[12] Only few ALD cycles can greatly increase the reversible capacity and long-term durability of sulfur cathodes.[13] This strategy offers tremendous advantages, including facile

scalability and formation of continuous ultrathin encapsulating films over the whole electrode, which can improve the mechanical integrity of the electrodes and increase the contact between the electrode and the liquid electrolyte, improving its impregnation and diffusion of ions.[14]

In this work, a facile approach to improve the connection among sulfur-carbon particles and therefore, the integrity of the electrodes, by ALD is proposed. Micrometer sized particles of a sulfur-carbon composite have been coated using a fluidized bed reactor (FBR), a novel technology that has not been used before for this aim. Upon fluidization, the particles, individually or in small agglomerates, are exposed to the ALD precursors with their whole surface. Alumina (Al_2O_3) was selected as coating material. With only a few deposition cycles of alumina the reversible capacity and long-term durability of a cathode can be already greatly increased.[10],[15] Physicochemical characterization of the coated particles was carried out in order to identify the amount of deposited alumina and the loss of sulfur during the ALD process. ICP-MS measurements confirmed an alumina deposition after the ALD process, which increased with the number of ALD cycles. Thermogravimetric analysis revealed that some sulfur was lost during the ALD process, especially at larger numbers of cycles. Electron microscopy images showed that the alumina deposition on the particles proceeded in form of clusters. The deposited alumina enhanced the interaction between the sulfur-carbon composite particles, thus eliminating cracks and holes on the electrode and enhancing both the electronic conductivity and electrolyte absorption by the cathode. Finally, the electrochemical performance was studied, where 5 ALD-coated composite electrodes were compared to standard sulfur cathodes, showing improvement of the cell capacity and cycle life of lithium-sulfur batteries, for both low and high sulfur loadings.

5.2. Experimental section

5.2.1. Experimental setup

Sulfur-carbon composite powders from the electrode were coated in a home-made fluidized bed reactor (FBR), schematically shown in Figure 24a. Figure 24b

presents a photograph of the constructed reactor in our laboratory. The design of the FBR was based on the reactor described by D. Valdesueiro *et al.*[16] The fluidized bed reactor is divided into three parts: the gas dosing part, the reactor itself and the residual gas treatment part.

The gas dosing part is composed of bubblers in which ALD precursors are stored. Swagelok diaphragm-sealed ALD valves and stainless-steel tubes are connected to the bubblers to deliver the precursors to the reactor column. Both the bubblers and the connections are externally heated.

The reactor itself is composed of a vertical stainless-steel column of 25 mm internal diameter and 250 mm height, placed on a single motor Paja PTL 40/40-24 vertical vibration table to assist the fluidization of the loaded particles. The vibration table is operated at 37,5 Hz. In order to control the bed temperature, a heating jacket is wrapped around the reactor during the process.

(a)

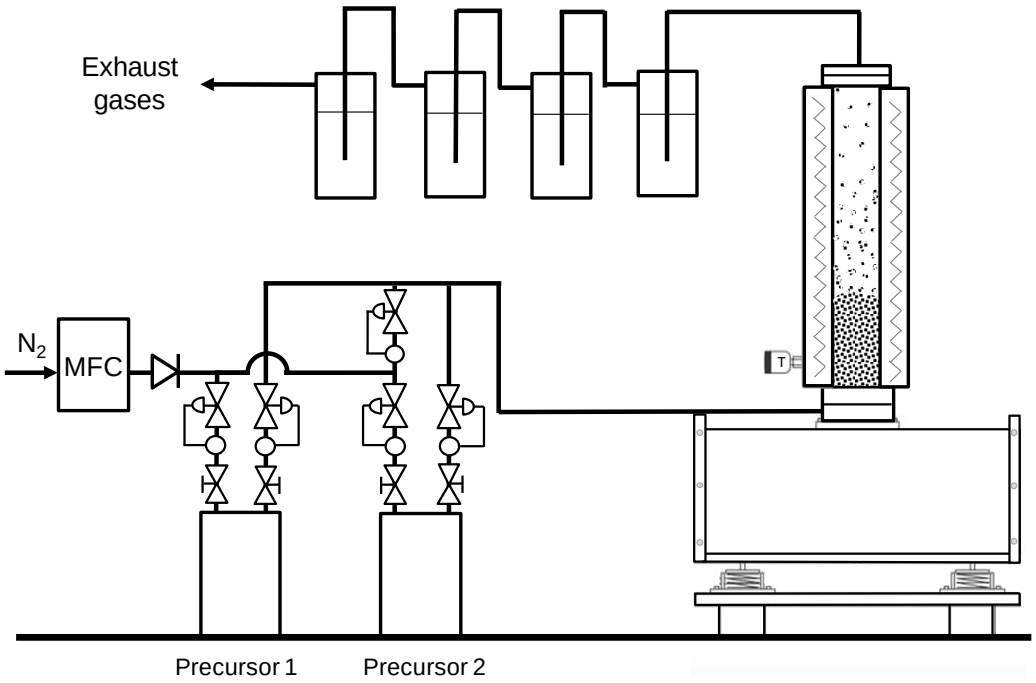

(b)

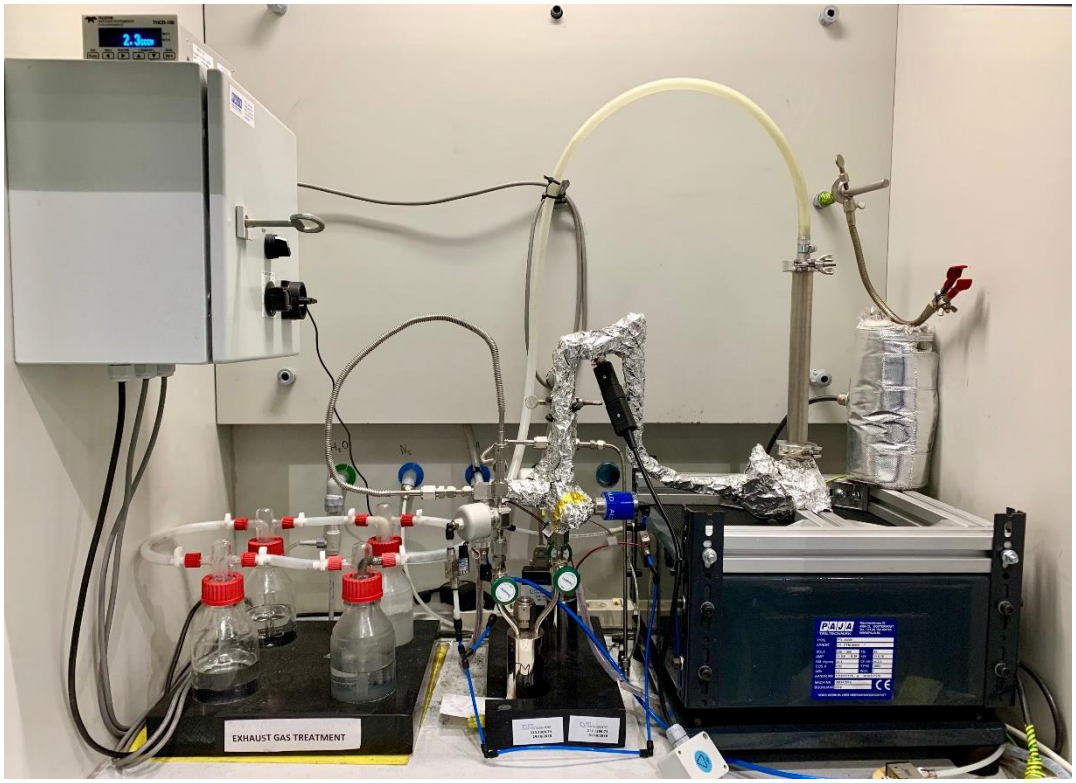

Figure 24. The home-made fluidized bed reactor (FBR), (a) schematics, (b) photograph of the reactor in Nanomaterials laboratory at CIC nanoGUNE. From left to right: the gas residual treatment section, the gas dosing section and the reactor itself where the particles are processed on the top of the vibration table.

To avoid loss of particles from the reactor, two sintered stainless steel 316L filters, with 20-micrometer pore size, are placed on both ends of the column. As the pore size of the filters is several orders of magnitude smaller than the particle size, the risk of losing particles is small.[17]–[19] The composite particles show a dynamic aggregation and disaggregation behavior during the process, while breaking and recombining constantly due to collisions between the solids.[20] The dynamic behavior and large porosity of the material ensure that the precursor molecules reach the whole surface area, even inside corrugated surfaces.

The residual gas treatment part consists of four glass bottles filled with mineral oil to remove possible traces of unreacted precursors and the products of the reactions.

5.2.2. Sulfur-carbon composite preparation

80 wt% of micrometer sized commercial sulfur powder (<40 μm Merck) and 20 wt% of nanometer sized Ketjen Black (KB) 600JD (AkzoNobel) with a high surface area (S_{BET}: 1400 $m^2 \cdot g^{-1}$) were homogeneously mixed in ethanol by ball-milling for 3h. Afterwards, mixed sulfur-carbon powder was thermally treated at 300 °C for 2 h in order to properly impregnate the sulfur on the high area carbon powder matrix.

5.2.3. ALD process

The prepared sulfur-carbon (S-KB) composite was used as substrate for the coating experiments. In each process, the reactor column was loaded with 6 g of the composite. As ALD precursors, trimethyl aluminum (TMA), obtained from Sigma Aldrich, and demineralized water were used. Both precursors were stored in 100 mL stainless steel bubblers which were kept at room temperature during the coating experiments. Pressurized nitrogen was provided to the column as a carrier gas with a flow of 800 standard cubic centimeters per minute (sccm). This flow not only fluidized the powder during the process, but it was also used as carrier gas for the precursors and purging gas for removal of the excess of precursors and the by-products of the reaction.

The column was always kept at atmospheric pressure and no pump was used during the process. At the beginning of each experiment, nitrogen was flown for 15 minutes to purge the trapped air and flood the reactor and lines with inert gas. We performed 2, 5, 10 and 20 ALD cycles with a dosage sequence of 1,5-10-1,5-10 minutes of TMA, nitrogen gas, water and nitrogen gas, respectively. After each ALD process, lines were released of the excess of precursors using a vacuum pump. The process temperature was 90 °C and the lines were heated to 110 °C in order to avoid condensation of the precursors and a resulting parasitic chemical vapor deposition (CVD) before reaching the material to be coated.

5.2.4. Fabrication of cathodes

Cathodes were fabricated using standard and ALD-modified S-KB composite powders. Each composite was dried and added to a solution of polyvinylidene fluoride (PVDF) 5130 (SOLVAY) in N-methyl-2-pyrrolidone (NMP) to fabricate the cathodic slurry. An additive conductor was added (carbon black, TIMCAL C-NERGY™ SUPER C45), capable of forming micellar structures. The mixture was sonicated for 30 minutes and stirred over night by using a mechanical mixer (RW 20 digital, IKA) at 360 rpm, in order to obtain a homogeneous slurry without agglomerates. These slurries were blade casted onto a carbon-coated aluminum foil (MTI Corp.) and dried at 60 °C under dynamic vacuum during 12 h before the cell assembly.

5.2.5. Physicochemical characterization

The physicochemical properties of the produced electrodes were characterized to determine the alumina deposition and sulfur loss during the ALD process.

Elemental analysis of alumina was carried out using ICP-MS (Induced Couple Plasma with Mass Spectroscopy, performed with an iCAP-Q, Thermo Fisher Scientific GmbH, Germany), which provides the mass fraction of aluminum in the coated samples, Al %(w/w). To determine Al %(w/w) in the samples, a small amount of the sulfur-carbon modified composite was dissolved in a prepared solution of 0,5 $mg \cdot mL^{-1}$ of nitric acid in water. After dissolution, the samples were aged for 72 hours and diluted 1:25 in MQ (milli-Q) water (2,7 % HNO_3, 20 $\mu g \cdot mL^{-1}$). The samples were then analyzed with ICP-MS to determine the mass fraction of aluminum in the samples, Al %(w/w).

Electron Microscopy studies were done with a Titan 60-300 (S)TEM microscope (FEI, Netherlands) operating at 300 kV in scanning mode (STEM). The microscope is equipped with a Quantum GIF 965 electron energy loss spectrometer (EELS), and element distribution in the samples was studied by STEM EELS spectral imaging utilizing Al L23 (73 eV), S L23 (163 eV), C K

(282 eV) and O K (532 eV) edges. The samples were prepared by ultrasound dispersion of the powders in ethanol and drop casting on holey carbon TEM grids.

The particle size and the particle size distribution were measured by dynamic light scattering (DLS) (Nanosizer, Malvern). The samples were dispersed in N-methyl-2-pyrrolidone (NMP) according to the following procedure. One milligram of the composite was mixed with 1 mL of NMP with strong agitation, followed by 15 min of sonication. Then, the particle size was calculated from the light scattering average diameters of 3 measurements per sample.

The elemental sulfur content of the cathodes was determined via thermogravimetric analysis (TGA) on a Netsch STA from 25 °C (room temperature) to 400 °C with a heating rate of 10 °C · min^{-1} under N_2 atmosphere.

Finally, the morphology of the fabricated electrodes was analyzed using an ULTRA plus ZEISS field emission scanning electron microscope (FESEM) equipped with an Ammeter EDAX (Apollo model) accessory for the elemental analysis of the samples by energy dispersive spectroscopy (EDS). The measurements were carried out at 20 kV accelerating voltage.

5.2.6. Electrochemical characterization

The produced cathodic electrodes were assembled into lithium-sulfur (Li-S) coin cells. The cathodes were prepared with sulfur loadings of 1,8 $mg_S \cdot cm^{-2}$ and 3,6 $mg_S \cdot cm^{-2}$, and theoretical capacities of 2,7 $mAh \cdot cm^{-2}$ and 5,4 $mAh \cdot cm^{-2}$, respectively, calculated from the theoretical capacity of elemental sulfur (1672 $mAh \cdot g^{-1}$). One layer of commercial polyolefin separator Celgard 2501 soaked with 50 µL of 0,38 M solution of Bis(trifluoromethane) sulfonimide lithium salt (LiTFSI) (Sigma-Aldrich) and 0,32 M of lithium nitrate ($LiNO_3$) (Sigma-Aldrich) as additive in 1/1(v/v) mixture of dimethoxyethane (DME) (BASF) and dioxolane (DOL) (BASF), was placed between the electrodes. Lithium metal (0,05 mm, Rockwood Lithium) was used as the anode in coin half cells (2025, Hohsen). Vacuum drying of electrodes and cell crimping has been performed in a dry room with dew point below -50 °C. Thereafter, assembled cells were aged for

20 hours and then cycled with a BaSyTec Cell Test System (Germany) at 25±1 °C, controlled by air conditioning.

The electrochemical behavior of the obtained ALD-coated sulfur electrodes was evaluated at different C-rates (C/10, C/5, C/2,5, 1C and 2C) taking into account the theoretical capacity of elemental sulfur (1672 $mAh \cdot g^{-1}$). The cycle life of the coin cells was investigated within a 1,7-2,6 V interval at C/5 charge-discharge current rates.

5.3. Results and discussion

Sulfur-carbon composite powders have been coated with alumina by atomic layer deposition in a fluidized bed reactor (FBR). The physicochemical characterization of the samples confirms alumina deposition on the particles. In Table 3 the aluminum contents according to the measurements by ICP-MS are shown. When the number of ALD cycles increases, the amount of deposited aluminum increases linearly, confirming successful deposition of alumina by ALD.

Table 3. Aluminum percentage on ALD-coated sulfur-carbon composites calculated from ICP-MS measurements.

Sample	**%Al (w/w)**
STD (0 ALD)	0
2 ALD	1,23
5 ALD	2,12
10 ALD	4,86
20 ALD	7,35

Transmissions electron microscope (TEM) images further confirm alumina deposition. Figure 25 shows the composites after performing ALD processes with 2, 5, 10 and 20 deposition cycles. The first column shows color-coded elemental maps with aluminum being yellow. The higher the number of cycles is, the more

alumina is deposited. Note that even with 20 ALD cycles the alumina is not completely embedding the particles, but rather separated alumina clusters and particles are formed on the powders. The individual elemental mappings of aluminum and oxygen (second and last columns) also confirm the growth of alumina. The mapping of sulfur and carbon confirms good dispersion and encapsulation of sulfur in the carbon matrix during the preparation of the composite. Sulfur is clearly visible around carbon particles in a good dispersion.

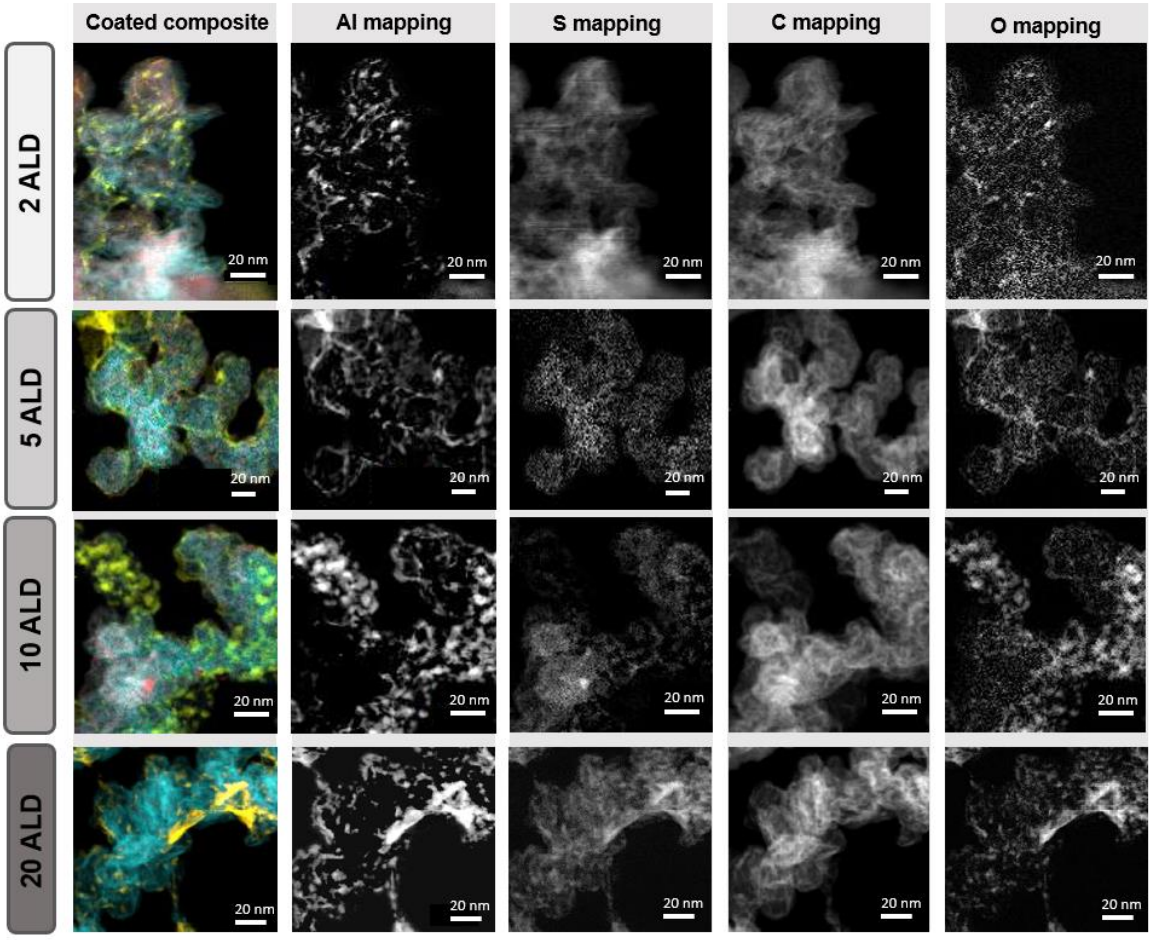

Figure 25. High-resolution TEM images of coated S-KB composite for 2, 5, 10 and 20 ALD cycles (from top to bottom) with the analyzed elements in colors: aluminum (yellow), sulfur (red), carbon (blue) and oxygen (green). Their

corresponding elemental mapping of aluminum, sulfur, carbon and oxygen (from left to right).

Dynamic light scattering (DLS) measurements demonstrate agglomeration of the particles after ALD process (see Table 4). While in the reference cathode the average size of particles is around 331,6 nm, it increases with the number of applied ALD cycles to almost triple size (867,6 nm) after 20 ALD cycles. This confirms that composite particles are embedded in alumina shells and bridged with the deposited alumina.

Table 4. Size distribution of the particles after various ALD cycle numbers, measured by DLS.

Sample	**Size distribution (nm)**
STD	331,6
2 ALD	535,5
5 ALD	661,6
10 ALD	774,7
20 ALD	867,6

The amount of sulfur in the final cathode is of paramount importance for the performance of Li-S batteries. While in the produced standard cathodes the sulfur content is 60 wt%, during the ALD process, part of the sulfur is lost by sublimation due to the elevated processing temperature (90 °C) or as byproduct, that is, as volatile mercaptans resulting from secondary reactions of the ALD precursors with S_8. This affects the electrochemical performance of the cell negatively. For that reason, S-KB composites with a sulfur loss higher than 15wt% were discarded before electrode fabrication.

In Figure 26, the sulfur loss during the ALD process, measured by TGA, is shown. Sulfur is lost in each ALD process and a correlation with the number of applied ALD cycles can be seen. The higher the number of cycles is, the more sulfur is lost. Therefore, S-KB composites coated with 20 ALD cycles were discarded before

electrode fabrication and also from electrochemical testing, for having a loss of sulfur higher than 15 wt%.

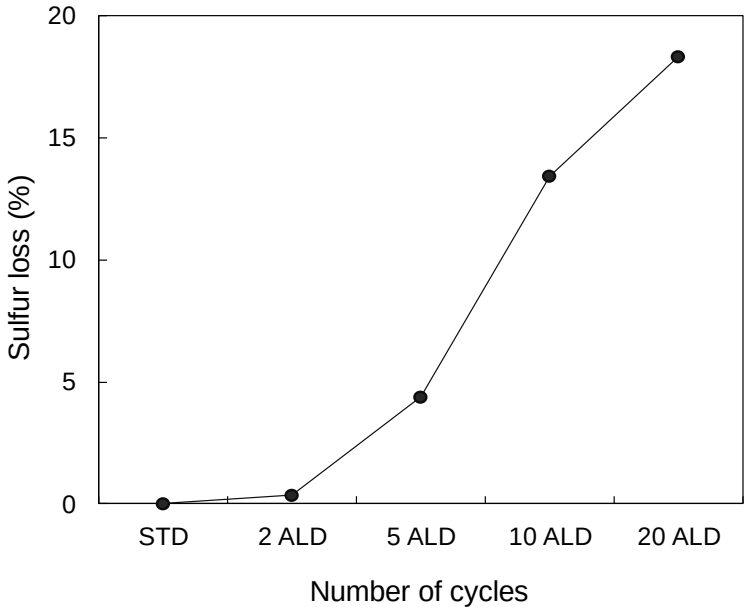

Figure 26. Sulfur loss (in wt%) of the cathodes as a function of applied ALD cycles.

The morphology of the fabricated electrodes was analyzed by scanning electron microscopy. Figure 27 shows cathodes with 1,8 $mg_S \cdot cm^{-2}$ (left) and 3,6 $mg_S \cdot cm^{-2}$ (right) sulfur loadings. In the first column from left, cracks in the standard sulfur cathode are visible at a glance. The porous S-KB composite particles easily absorb and trap a large amount of solvent during the slurry mixing and coating. During the subsequent drying process, the solvent evaporates, and the coating shrinks significantly. With the binder content being insufficient to bind these particles, cracks, big pores and holes are formed. This generally happens if nanosized or microsized materials are used for thick electrode coating and has negative effects on the capacity of the system.

After applying few cycles of ALD, the formation of those cracks on the electrode is suppressed. The reason may be that alumina binds and glues composite particles, bridging them. Moreover, sulfur and carbon surfaces are hydrophobic,

which results in no or just weak interactions between the particles. But after alumina deposition, thanks to its hydrophilicity, the surface interaction of the composite particles enhances, eliminating large holes and pores from the cathodic material where otherwise solvent would accumulate. However, with ALD cycles numbers higher than 5, the positive effect on the crack formation is reversed again and cracks re-appear. The most likely reason is the formation of larger agglomerates (see Table 4) during the ALD process that favor a crack formation upon drying of the slurry. This effect became more pronounced in the electrodes where the sulfur loading is increased to 3,6 $mg_S \cdot cm^{-2}$ and the electrode becomes thicker.

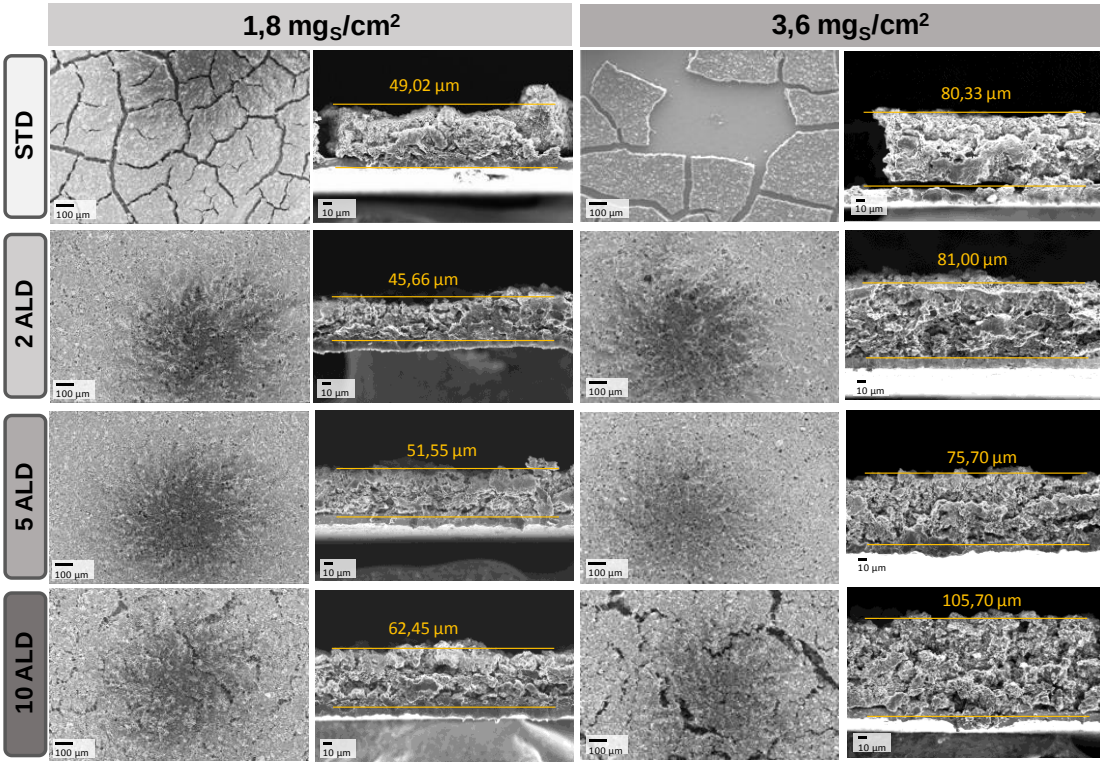

Figure 27. Top-view SEM images and cross sections of standard (uncoated), 2, 5 and 10 cycles ALD-coated electrodes with 1,8 $mg_S \cdot cm^{-2}$ (left) and 3,6 $mg_S \cdot cm^{-2}$ (right) sulfur loadings.

It is worth mentioning that not only the crack formation is significantly suppressed after few ALD cycles, but also the adhesion of the slurry to the

aluminum current collector is enhanced as can be seen from the cross section of the electrodes for both sulfur loadings, 1,8 $mg_S \cdot cm^{-2}$ and 3,6 $mg_S \cdot cm^{-2}$. In the standard cathode of 1,8 $mg_S \cdot cm^{-2}$ sulfur loading, a gap appeared between aluminum foil and cathodic material, which brings delamination of the active material and an extra resistance for electronic conductivity of the cell. This gap becomes stronger when the sulfur loading is doubled. With 3,6 $mg_S \cdot cm^{-2}$ sulfur loading, delamination is too large, so that the fabrication of standard cathodes with this sulfur loading is not feasible. After application of ALD, the gap disappeared, improving the adhesion of the active material to the current collector. Besides, the hydrophilic nature of alumina, which enhances the connection of particles, makes a better dispersion of the electrode material along the aluminum foil. As mentioned above, alumina interlinks composite particles and, in this way, generates small agglomerates which are beneficial for the cathode fabrication. However, if the coating exceeds 5 ALD cycles, the agglomerates become too large and cracks re-appear, seriously affecting the morphology of the cathode.

Electrochemical characterization of the modified lithium-sulfur cells was done to investigate the cell performance. The selected electrodes from previous characterizations with a sulfur loading of 1,8 $mg_S \cdot cm^{-2}$ were assembled into 2025 type coin cells at C/10, C/5, C/2,5, 1C and 2C current densities.

Figure 28a shows that for various current densities ALD deposition on sulfur-carbon composites improves the specific capacity of the cell. The difference in specific capacity between standard and coated samples increases, especially, for higher current densities. At 2C, the specific capacity of the cell increases from below 400 $mAh \cdot g_S^{-1}$ for standard samples to around 650 $mAh \cdot g_S^{-1}$ for ALD modified samples, confirming greatly enhanced performance. The tests of cycle life, analyzed at C/5 current density, show the same trend (Figure 28b). In this case, the coating improves the cell capacity from 600 $mAh \cdot g_S^{-1}$ to 850 $mAh \cdot g_S^{-1}$ for the best performing electrode, i.e. after 5 ALD deposition cycles.

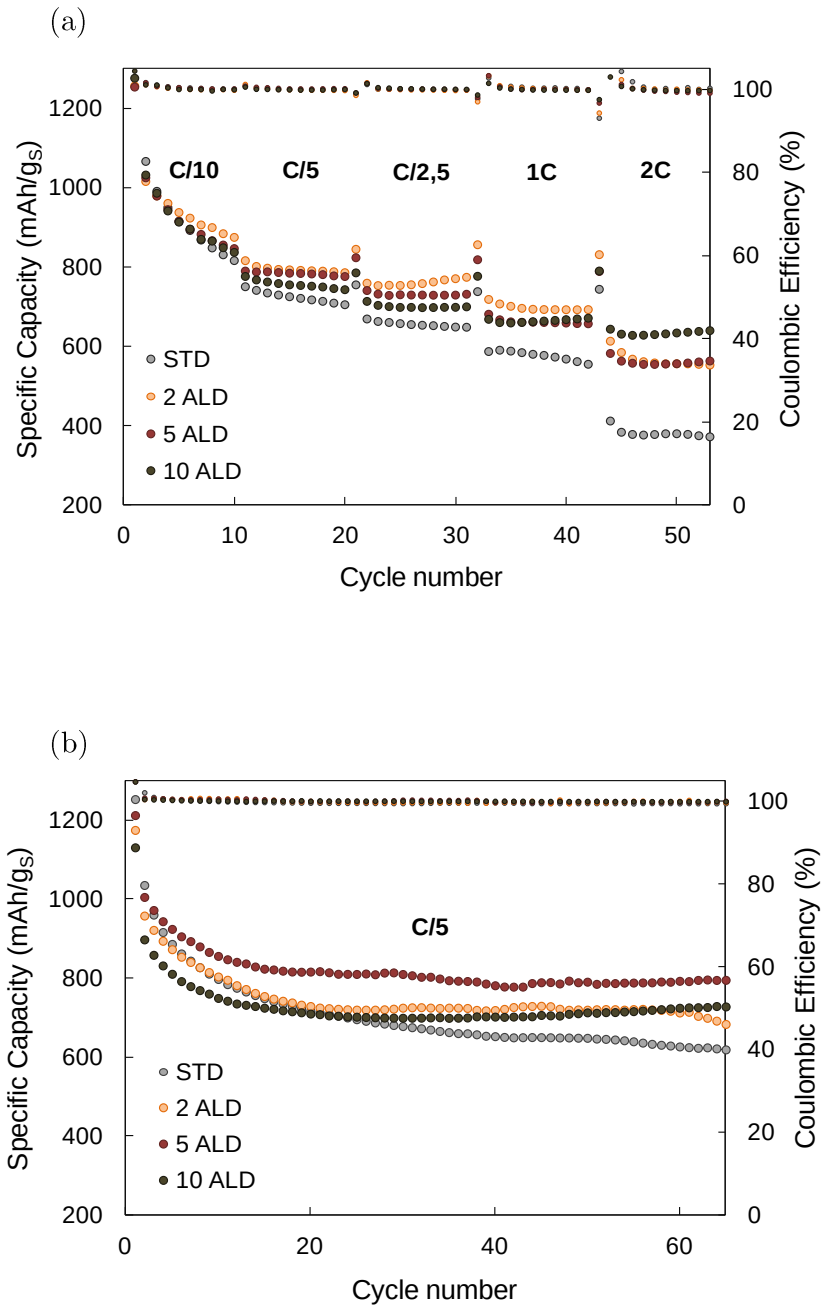

Figure 28. Electrochemical performance of lithium-sulfur batteries with ALD-coated sulfur-carbon composites with a sulfur loading of 1,8 $mg_S \cdot cm^{-2}$. (a) C-Rate performance analysis for different current densities and (b) cycling performance at C/5.

A likely explanation for this improvement is the improved cohesion of the particles after alumina deposition. Due to the OH groups that terminate the surface of the deposited alumina, the cohesion of the particles and the adhesion of the electrode material (dried slurry) to the aluminum foil is improved, thus further enhancing both electronic and ionic conductivity, and electrolyte penetration. Besides, this integration of particles may suppress the out-diffusion of polysulfides and favor its reversible transformation. Secondary structures may have been generated inside the large agglomerated sulfur-carbon particles that further suppress the diffusion of polysulfides during the discharge/charge cycles.

In order to increase the cell capacity, we increased the amount of sulfur in the electrode from 1,8 $mg_S \cdot cm^{-2}$ to 3,6 $mg_S \cdot cm^{-2}$. In this case, the 10 ALD cycles electrode was discarded from electrochemical measurements for its significant sulfur loss during the ALD process (>10%). In the previous electrochemical tests (Figure 28), the 5 ALD sample showed the best performance with a sulfur loading of 1,8 $mg_S \cdot cm^{-2}$. Thus, the 5 ALD cycles modified S-KB composite was chosen for assembling cells with a sulfur loading of 3,6 $mg_S \cdot cm^{-2}$.

Figure 29 shows the electrochemical performance of the 5 ALD sample with a sulfur loading of 3,6 $mg_S \cdot cm^{-2}$. In order to make comparison with the reference sample, the standard sample with 1,8 $mg_S \cdot cm^{-2}$ was used, since a standard cathode with 3,6 $mg_S \cdot cm^{-2}$ was not possible to assemble in a cell due to the delamination of the material from the aluminum foil. The specific capacity of the cell improved at low C-rates. At C/5, for instance, it increases from 700 $mAh \cdot g_S^{-1}$ to 900 $mAh \cdot g_S^{-1}$ after ALD. However, this capacity enhancement over the standard electrode was lost at high C-rates (1C, 2C). The reason could be the higher thickness of the electrode, an consequently porosity, which may increase the resistance in electronic conductivity. For high energy densities, where also the current is higher and the kinetics of the redox reaction are faster, this resistance has to be overcome in less time, resulting in a drop of the performance of the system.

Note that during the first cycles at C/10, there is a gradual capacity increase. This is caused by the slow electrolyte wetting process within the thick electrode as

it was seen by Dongping *et al.*[4] Once the electrolyte is correctly absorbed, the results at low current densities improve considerably the cell performance.

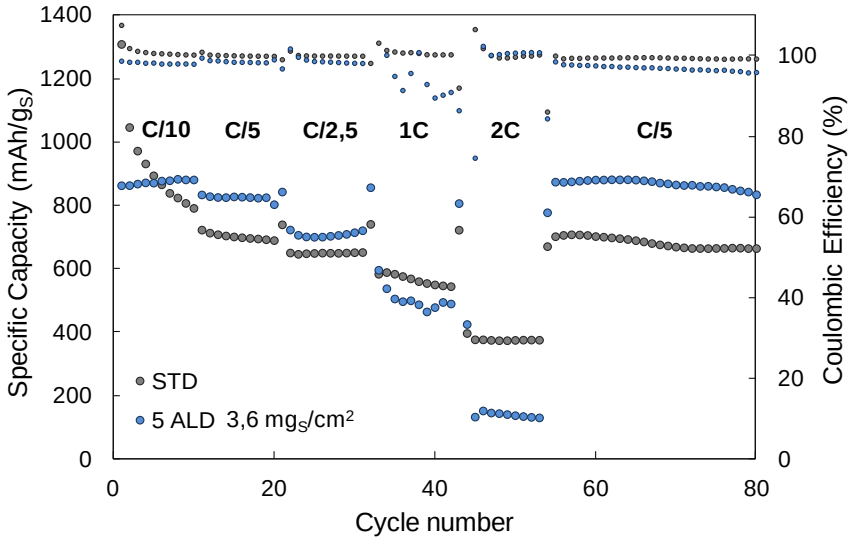

Figure 29. Electrochemical performance of lithium-sulfur batteries after 5 ALD cycles-coated sulfur-carbon composites with a sulfur loading of 3,6 $mg_S \cdot cm^{-2}$ for various C-rates.

In Figure 30, the variation of sulfur loading is studied using 5 ALD cycles-modified S-KB composite. For that purpose, the specific capacity is analyzed as a function of electrode mass and not of sulfur mass, where also the Al current collector is considered.

The electrochemical measurements in Figure 30 show two tendencies. At low current densities (C/10, C/5 and C/2,5), the 5 ALD samples, both 1,8 $mg_S \cdot cm^{-2}$and 3,6 $mg_S \cdot cm^{-2}$, show higher specific capacity than cells with standard cathodes. This difference to the reference sample is higher when the sulfur loading is 3,6 $mg_S \cdot cm^{-2}$, which is reasonable, since the amount of the active material is doubled. On the other hand, for high current densities (1C and 2C), the high amount of sulfur in the electrode (3,6 $mg_S \cdot cm^{-2}$) shows drawbacks, decreasing the specific capacity of the cell to very low values. As mentioned earlier, this is related to the electronic resistance to be overcome in thick electrodes, at high

current densities and shorter time, due to the fast kinetics of the redox reaction of the battery system.

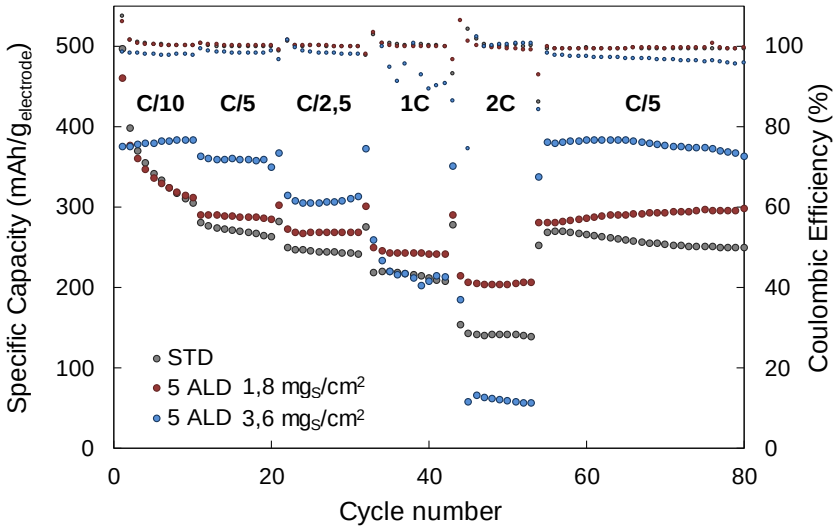

Figure 30. Electrochemical performance of lithium-sulfur batteries with standard electrode (1,8 $mg_S \cdot cm^{-2}$ sulfur loading) and 5 ALD cycles modified S-KB composite with 1,8 $mg_S \cdot cm^{-2}$ and 3,6 $mg_S \cdot cm^{-2}$ sulfur loadings at different C-rates. The specific capacity is shown as $mAh \cdot g_{electrode}^{-1}$.

5.4. Conclusions

In this work a new approach to improve the surface chemistry/physics and increase sulfur loading in cathodes of lithium-sulfur batteries is shown, resulting in an enhancement of the capacity and efficiency of the battery.

Sulfur-carbon composites have been coated with alumina in a fluidized bed reactor by ALD. The fluidization of particles and the employed number of ALD cycles generated alumina particles on the top of composite powders that bridge them from each other, agglomerating and interconnecting composite particles. Thanks to the cohesion between the modified particles, the commonly occurring cracks

and holes in the cathode are eliminated, especially at high sulfur loadings (>2 $mg_S \cdot cm^{-2}$), thus improving the electronic conductivity of the cell.

The alumina deposition further reduces the porosity of the cathode, having positive effects on the absorption and penetration of the electrolyte throughout the electrode, again interconnecting the active material in an optimal way and benefiting the cycling stability of Li-S cells. Moreover, by applying an external pressure that reduces the electrode thickness would be beneficial for the final volumetric energy density of the cell, while decreasing slightly the remaining porosity would help to reduce the amount of electrolyte needed to wet the entire electrodes, still maintaining a high amount of sulfur.

From this research, we conclude that the application of only 5 ALD cycles to the sulfur-carbon composite is sufficient to increase the sulfur loading in the cathode even to values around 3,6 $mg_S \cdot cm^{-2}$, without cracks and holes, and to achieve capacity values higher than in conventional Li-S cathodes.

References

[1] Yan, B., Li, X., Bai, Z., Song, X., Xiong, D., Zhao, M., Li, D., Lu, S. A review of atomic layer deposition providing high performance lithium sulfur batteries. *J. Power Sources* **338**, 34–48 (2017).

[2] Ye, Y., Wu, F., Liu, Y., Zhao, T., Qian, J., Xing, Y., Li, W., Huang, J., Li, L., Huang, Q., Bai, X., Chen, R. Toward Practical High-Energy Batteries: A Modular-Assembled Oval-Like Carbon Microstructure for Thick Sulfur Electrodes. *Adv. Mater.* **29**, 1700598 (2017).

[3] Wang, Q., Mao, B., Stoliarov, S. I., Sun, J. A review of lithium ion battery failure mechanisms and fire prevention strategies. *Prog. Energy Combust. Sci.* **73**, 95–131 (2019).

[4] Lv, D., Zheng, J., Li, Q., Xie, X., Ferrara, S., Nie, Z., Mehdi, L. B., Browning, N. D., Zhang, J. G., Graff, G. L., Liu, J., Xiao, J. High Energy Density Lithium-Sulfur Batteries: Challenges of Thick Sulfur Cathodes. *Adv. Energy Mater.* **5**, 1402290 (2015).

[5] Wang, J., Yao, Z., Monroe, C. W., Yang, J., Nuli, Y. Carbonyl-β-cyclodextrin as a novel binder for sulfur composite cathodes in rechargeable lithium batteries. *Adv. Funct. Mater.* **23**, 1194–1201 (2013).

[6] Fu, Y., Su, Y. S., Manthiram, A. Sulfur-carbon nanocomposite cathodes improved by an amphiphilic block copolymer for high-rate lithium-sulfur batteries. *ACS Appl. Mater. Interfaces* **4**, 6046–6052 (2012).

[7] Gomez, I., Mecerreyes, D., Blazquez, J. A., Leonet, O., Ben Youcef, H., Li, C., Gómez-Cámer, J. L., Bundarchuk, O., Rodriguez-Martinez, L. Inverse vulcanization of sulfur with divinylbenzene: Stable and easy processable cathode material for lithium-sulfur batteries. *J. Power Sources* **329**, 72–78 (2016).

[8] Zhang, Z., Li, Z., Hao, F., Wang, X., Li, Q., Qi, Y., Fan, R., Yin, L. 3D interconnected porous carbon aerogels as sulfur immobilizers for sulfur

impregnation for lithium-sulfur batteries with high rate capability and cycling stability. *Adv. Funct. Mater.* **24**, 2500–2509 (2014).

[9] Wang, Z., Li, X., Cui, Y., Yang, Y., Pan, H., Wang, Z., Wu, C., Chen, B., Qian, G. A metal-organic framework with open metal sites for enhanced confinement of sulfur and lithium-sulfur battery of long cycling life. *Cryst. Growth Des.* **13**, 5116–5120 (2013).

[10] Li, X., Liu, J., Wang, B., Banis, M. N., Xiao, B., Li, R., Sham, T. K., Sun, X. Nanoscale stabilization of Li-sulfur batteries by atomic layer deposited Al_2O_3. *RSC Adv.* **4**, 27126–27129 (2014).

[11] Jung, Y. S., Cavanagh, A. S., Riley, L. A., Kang, S. H., Dillon, A. C., Groner, M. D., George, S. M., Lee, S. H. Ultrathin direct atomic layer deposition on composite electrodes for highly durable and safe Li-Ion batteries. *Adv. Mater.* **22**, 2172–2176 (2010).

[12] Kim, H., Lee, J. T., Lee, D. C., Magasinski, A., Cho, W. Il, Yushin, G. Plasma-enhanced atomic layer deposition of ultrathin oxide coatings for stabilized lithium-sulfur batteries. *Adv. Energy Mater.* **3**, 1308–1315 (2013).

[13] Yu, M., Yuan, W., Li, C., Hong, J. D., Shi, G. Performance enhancement of a graphene-sulfur composite as a lithium-sulfur battery electrode by coating with an ultrathin Al_2O_3 film via atomic layer deposition. *J. Mater. Chem. A* **2**, 7360–7366 (2014).

[14] Meng, X., Liu, Y., Cao, Y., Ren, Y., Lu, W., Elam, J. W. High-Performance High-Loading Lithium – Sulfur Batteries by Low Temperature Atomic Layer Deposition of Aluminum Oxide on Nanophase S Cathodes. *Adv. Mater. Interfaces* **4**, 1700096 (2017).

[15] Groner, M. D., Fabreguette, F. H., Elam, J. W., George, S. M. Low-Temperature Al_2O_3 Atomic Layer Deposition. *Chem. Mater.* **16**, 639–645 (2004).

[16] Valdesueiro, D., Meesters, G. M. H., Kreutzer, M. T. Gas-Phase Deposition of Ultrathin Aluminium Oxide Films on Nanoparticles at Ambient Conditions. *Materials (Basel).* **8**, 1249–1263 (2015).

[17] van Ommen, J. R., Valverde, J. M., Pfeffer, R. Fluidization of nanopowders: A review. *J. Nanoparticle Res.* **14**, 1–29 (2012).

[18] Hakim, L. F., George, S. M., Weimer, A. W. Conformal nanocoating of zirconia nanoparticles by atomic layer deposition in a fluidized bed reactor. *Nanotechnology* **16**, 375–381 (2005).

[19] King, D. M., Spencer, J. A., Liang, X., Hakim, L. F., Weimer, A. W. Atomic layer deposition on particles using a fluidized bed reactor with in situ mass spectrometry. *Surf. Coatings Technol.* **201**, 9163–9171 (2007).

[20] Beetstra, R., Lafont, U., Nijenhuis, J., Kelder, E. M., Van Ommen, J. R. Atmospheric pressure process for coating particles using atomic layer deposition. *Chem. Vap. Depos.* **15**, 227–233 (2009).

Chapter 6

Summary and Outlook

In this chapter, a summary of the most relevant results and conclusions obtained in this thesis is presented. Besides, a future perspective of the performed work is described.

In this thesis a facile approach for coating powders by atomic layer deposition (ALD) is described, which offers a pathway to introduce new functionalities to the coated particles or improve already existing ones. Besides the introductory and methods chapters, the main scientific part of the thesis is divided into three chapters, each of which describes its individual results and conclusions. While chapter 3 is focused on the synthesis of core-shell nanoparticles by ALD, chapter 4 and chapter 5 describe coating and properties of powder materials for energy storage applications, namely, for lithium-sulfur batteries.

The first part (chapter 3) describes the synthesis of core-shell nanoparticles by ALD on the example of TiO_2-coated magnetite. Their composition and physical properties are experimentally and theoretically studied. The novelty of this work lies in the finding that γ-Fe_2O_3 nanoparticles become coated and simultaneously reduced by ALD to form the final product composed of Fe_3O_4-TiO_2 core-shell nanoparticles. The reduction of γ-Fe_2O_3 to Fe_3O_4 is a function of the applied precursor and the processing temperature. In the course of the process, the released ligand of the metal organic precursor, $(CH_3)_2N^-$, induced a reduction of the Fe^{3+} from γ-Fe_2O_3, while itself it became oxidized and recombined to form tetramethylhydrazine as by-product. Besides, the chemical nature of the cation of the precursor also played an important role; the more electronegative the cation was, the more energy was necessary to release the ligands, which conditioned their recombination to form tetramethylhydrazine. Therefore, the results of this work showed that the appropriate composition of precursors and a matching of the selection of the substrate will pave the way for numerous new compositions. The use of the ALD process for coating and simultaneous reduction of nanomaterials simplifies numerous attempts to generate multifunctional materials for emerging applications, such as, catalysis, energy storage or medicine.

In the second part of this thesis, the study of ALD on cathode materials for lithium-sulfur batteries was done in order to improve the performance of such energy storage systems.

In chapter 4, an approach towards coating of sulfur-based prefabricated cathodes of lithium-sulfur batteries by ALD is described. Thanks to the deposited Al_2O_3,

the performance of the cells was improved, increasing the retention capacity of the system and minimizing the most common drawbacks of Li-S batteries, namely, the well-known shuttle effect. This enhancement may be attributed to the trapping of polysulfides by alumina, which can bind polysulfides from the cathode, thus reducing their dissolution and the resulting generation of extra resistance to the electronic conductivity of the cell. Besides, it may enhance the electronic conductivity and the electrolyte absorption by the electrode, resulting from the cohesions of sulfur-carbon particles, induced by the deposited alumina. In other words, the alumina acts as binder for the particles. As a result of the investigations, optimal parameters for the ALD process, with few cycles and low process temperatures, were found. The best performance was observed for coated sulfur-based cathode after 2 ALD cycles, processed at 85 °C. The capacity of this system ($mAh \cdot gr_S^{-1}$) was improved by 13 % for low current densities and by 50 % for high current densities with regard to the standard cathode. Moreover, the use of such low process temperatures and low numbers of ALD cycles results in a more cost-effective and time efficient processes than the ones commonly used for applying coatings by ALD.

Finally, in chapter 5 a novel approach for improving the performance of lithium-sulfur batteries is described. Micrometer sized sulfur-carbon composite particles, used for the cathode of lithium-sulfur batteries, were coated with alumina by ALD using a home-made fluidized bed reactor. After processing of the particles, the cathode was assembled. As a result, the deposited Al_2O_3 enhanced the interaction between the sulfur-carbon composite particles by bridging them, agglomerating and interconnecting composite particles, and thus, eliminating cracks and holes in the electrode after their fabrication, which improves both the electronic conductivity and electrolyte absorption by the cathode. Apart from the improvement in the morphology of the electrode, the electrochemical performance of the ALD-modified cells was also enhanced. It was found that only 5 ALD cycles were enough to improve the capacity of lithium-sulfur batteries ($mAh \cdot grs^{-1}$) by 30 % at low current densities and by 50 % at high current densities, with respect to the standard cathode system.

Thanks to the improved particle surface chemistry of the modified sulfur-based cathodes, without holes and cracks, the sulfur loading was increased from 1,8 $mg_s \cdot cm^{-2}$ to 3,6 $mg_s \cdot cm^{-2}$ in order to gain more capacity in the cell, which was achieved with 5 ALD cycle modified cathodes. In this case, the capacity of the system (given as $mAh \cdot g_{electrode}^{-1}$ for making comparisons between different sulfur loadings) was considerably increased by 32 % for 1,8 $mg_s \cdot cm^{-2}$ sulfur loading and by 60 % for 3,6 $mg_s \cdot cm^{-2}$ sulfur loading, with respect to the standard system.

In conclusion, ALD was successfully applied to lithium-sulfur batteries, improving the capacity of the cells. Only few ALD cycles of alumina were sufficient to enhance the performance of the studied energy storage systems. If we compare with the results obtained from ALD applied directly to prefabricated sulfur electrodes, an ALD application to sulfur-carbon composite before cathode fabrication provides the best results as summarized in the following:

- In ALD coated sulfur-carbon composites, the morphology of the cathodes is improved, eliminating pores, holes and cracks (even at high sulfur loadings), thanks to the generated cohesions of composite particles by alumina before electrode fabrication, thereby resulting in an increased capacity retention of the system.
- Even though both cases show an increment of 50 % in the cell capacity at high current densities, at low current densities the capacity is much higher if ALD was applied to the composite particles (30 % of increment) than to the prefabricated cathode (13 % of increment). Besides, only if ALD was applied to the composite powder, it was possible to increase the sulfur loading until values as high as 3,6 $mg_s \cdot cm^{-2}$. Resulting from that, the capacity of the battery increased by 60 % regarding the standard cathode system.
- The used reactor technology, the fluidized bed reactor, allows ALD processes directly on composite powders, which offers tremendous advantages for coating large amounts of particles, resulting in a facile way to scale-up the coating process, as well as its implementation in different industrial processes, being cost-effective and time-efficient.

The results presented in this thesis show a first step in the development of functioning and reliable Li-S batteries and can be further improved in a future work. Considering the wide variety of chemical precursor for ALD applications, further types of metal oxides or materials can be deposited on composite sulfur powders, introducing even better functionality and stability. A crucial point is the electrical conductivity of the coating, therefore further processes, which are more suitable for lithium-sulfur batteries, need to be applied and tested, which opts for a bright future in the optimization of Li-S batteries and therefore the next generation of energy storage enabled by ALD.

List of publications

[1] *Ligand-Induced Reduction Concerted with Coating by Atomic Layer Deposition on the Example of TiO_2-coated Magnetite Nanoparticles*
Sarai García, Alberto López-Ortega, Yongping Zheng, Yifan Nie, Kyeongjae Cho, Andrey Chuvilin and Mato Knez, *Chemical Science*, **10**, 7, 2171–2178 (2019).
(Chapter 3)

[2] *Controlled Atomic Layer Deposition of Aluminum Oxide to Improve the Performance of Lithium-Sulfur Batteries*
Sarai García, Olatz Leonet, Eneko Azaceta, Iñaki Gómez, Antonio Reifs, J. Alberto Blázquez and Mato Knez, submitted to *Energy Technology*, manuscript number: ente.201901432.
(Chapter 4)

Patents

[1] *High Energy Density Sulfur Cathode for Lithium-Sulfur Batteries*
Sarai García, Olatz Leonet, Eneko Azaceta, Iñaki Gómez, Mikel Beltrán, J. Alberto Blázquez and Mato Knez, submitted as *European Patent* (2020). Patent number: EP20382003
(Chapter 5)

Acknowledgements

This thesis has been the result of almost four years of intense work, not only for me, but also for people who have been there supporting and working with me for making it possible. I would like to take the opportunity to thank all these people.

First of all, I would like to start acknowledging my supervisor Prof. Dr. Mato Knez. I am very grateful for having the opportunity of being part of your research group at CIC nanoGUNE. You have been the best supervisor that I could ever have, always very positive and willing to help. Thank you very much for everything Mato, this thesis could not have been possible without you.

I am very grateful also to my group, Nanomaterials. I would like to thank the past and present members of the team. Fang Yang, Weike Wang, Jaime, Unai, Nagore, Victor, Karina, Oksana, Gabriele, Ana, Andoni, Livia... thank you very very much to each of you for helping and supporting me during my thesis, the good moments that we shared in the lab and the "issues" that we got, I will never forget all those moments. Se merecen una mención especial dos personas, que no solo han sido compañeros de trabajo para mí. Mikel e Itxasne. Mikel, muchísimas gracias por todo lo que me has ayudado, has sido un técnico, compañero, y amigo increíble durante todo este tiempo, gran parte de la tesis, la he podido llevar a cabo gracias a ti. Nunca se me olvidarán los sustos y alegrías que nos llevamos durante la fabricación del reactor, siempre quedarán en anécdotas. Y a ti Itxasne, eskerrik asko benetan, has ido como una hermana mayor para mí durante estos años, siempre dispuesta a ayudarme y aconsejarme cuando lo he necesitado.

Many thanks to the people who have taken part in my work and help me to obtain incredible results during my PhD thesis. I would like to highlight the help of Dr. Andrey Chuvilin, for being always our collaborator and for taking incredible TEM images. Una persona clave durante mi tesis ha sido el Dr. Alberto López-Ortega. Muchísimas gracias Alberto por haberme ayudando tanto, en

especial en los primeros años de mi tesis. Gracias a ti, aprendí lo necesario del mundo del magnetismo, los "papers" y a no desanimarme si algo salía mal. La maravillosa portada de esta tesis no existiría sin la ayuda de Antonio. Muchísimas gracias Antonio, eres un artista!! The people from Delft University deserve a special mention; the design of my reactor would not have been possible without your help, but especially without Damiano. I was lucky to meet you in Sweden, none of my work and frustration during the first years could have gone ahead without your help. Grazie mille! :)

Coming back to Nanogune, I want to thank all these good years to the nanopeople community. I feel very lucky for being part of it. The coffee-breaks, lunches, beers, laughs, dinners etc. have been very special for me. Juanma, Josu, Nieves, Eva, Eneko, Andoni, Mikel, Jaione, Maria, Teresa, Ana y muchos otros más, nunca olvidaré las risas y los buenos momentos que hemos pasado dentro y fuera de Nanogune.

Pasando a la segunda etapa de mi tesis, quiero agradecer a la gente que me ha ayudado y lo aprendido durante mi estancia en Cidetec. En primer lugar, quiero dar las gracias a mi codirector, el Dr. Alberto Blázquez, por darme la oportunidad de formar parte de su equipo e introducirme en el interesante mundo de las baterías. Muchísimas gracias Alberto, por estar siempre dispuesto a ayudarme y motivarme en este nuevo campo para mí. En este sentido, quiero agradecer al grupo de baterías de Li-S, por su apoyo, y el tiempo dedicado a enseñarme. Gracias en especial a Olatz, por guiarme, enseñarme y estar siempre dispuesta a ayudar cuando lo he necesitado, a mi compi Iñigo, por las risas y los buenos momentos pasados en el lab y por supuesto, a Iñaki, Eneko y Julen, por ayudarme y enseñarme durante mi estancia en el centro.

Muchísimas gracias a todas mis amig@s, por estar siempre que las he necesitado, por escucharme y apoyarme durante estos tres años y medio de tesis. Por un lado, a la gente que he tenido en Donosti; Haizea, has ido un apoyo enorme para mí, siempre dispuesta a escucharme, y Leire, por haber sido compañera, amiga y como una hermana en estos años en Donosti, por estar siempre disponible para ayudarme en los buenos y en los malos momentos. Por otro lado, a mis amigas y

cuadrilla. Habéis estado siempre presentes, y apoyándome desde la distancia. En especial Oihane, Libe, Ane y Ana, por escucharme, apoyarme, animarme e incluso venir a Donosti siempre que lo he necesitado. Eskerrik asko! :)

Finalmente, quisiera dejar las últimas líneas para agradecer a las personas más importantes durante mi tesis. Markel, Jon, Aita y Ama. Muchas gracias por apoyarme, aguantarme y estar siempre dispuestos a ayudarme. En especial a ti Ama, por ser, independientemente de la distancia, un apoyo constante todos los días y creer en mí. Eta azkenik, nanogunetik tesiaz aparte, eroan dodan gauzarik garrantzitsuena zu zarelako. Eskerrik asko danagatik Jon.

Eskerrik asko!! :)

Sarai.